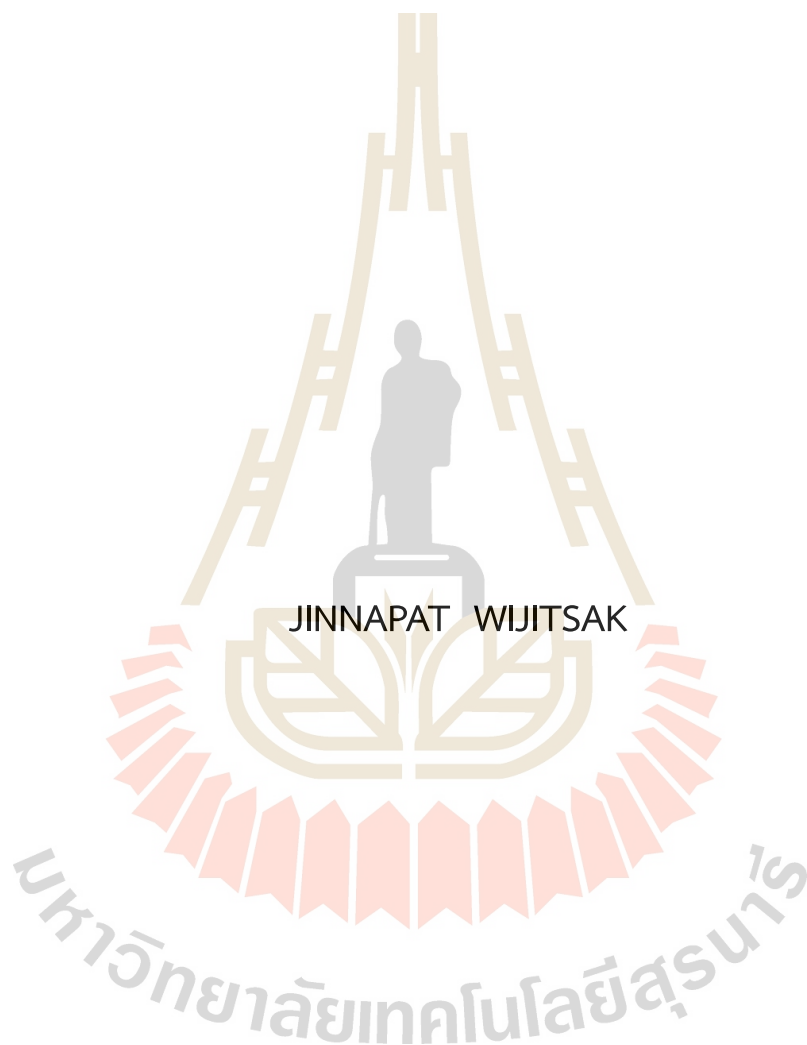


CARBON AND COPPER COMPLEX ELECTRODES FOR THE  
DETECTION OF MOLECULAR BIOMARKERS: GUANOSINE  
AND CREATININE



A Thesis Submitted in Partial Fulfillment of the Requirements for the  
Degree of Master of Science in Chemistry  
Suranaree University of Technology  
Academic Year 2024

ข้อไฟฟ้าชนิดคาร์บอนและสารประกอบเชิงซ้อนของทองแดงสำหรับการ  
ตรวจวัดตัวบ่งชี้ทางชีวภาพ: กัวโนซีนและครีเอตินีน



นางสาวจิณณพัตร วิจิตรศักดิ์

วิทยานิพนธ์นี้เป็นส่วนหนึ่งของการศึกษาตามหลักสูตรปริญญาวิทยาศาสตรมหาบัณฑิต  
สาขาวิชาเคมี  
มหาวิทยาลัยเทคโนโลยีสุรนารี  
ปีการศึกษา 2567

CARBON AND COPPER COMPLEX ELECTRODES FOR THE DETECTION OF  
MOLECULAR BIOMARKERS: GUANOSINE AND CREATININE

Suranaree University of Technology has approved this thesis submitted in partial fulfillment of the requirements for a Master's Degree.

Thesis Examining Committee



(Assoc. Prof. Dr. Sanchai Prayoonpokarach)  
Chairperson



(Assoc. Prof. Dr. Kamonwad Ngamchuea)  
Member (Thesis Advisor)



(Dr. Suttipong Wannapaiboon)  
Member



(Assoc. Prof. Dr. Phimpaka Harding)  
Member



(Asst. Prof. Dr. Patcharin Chaisuwan)  
Member



(Assoc. Prof. Dr. Yupaporn Ruksakulpiwat)  
Vice Rector for Academic Affairs  
and Quality Assurance



(Prof. Dr. Santi Maensiri)  
Dean of Institute of Science

จิณณพัตร วิจิตรศักดิ์ : ขั้วไฟฟ้าชนิดคาร์บอนและสารประกอบเชิงซ้อนของทองแดงสำหรับการตรวจวัดตัวบ่งชี้ทางชีวภาพ: กัวโนซีนและครีเอตินีน (CARBON AND COPPER COMPLEX ELECTRODES FOR THE DETECTION OF MOLECULAR BIOMARKERS: GUANOSINE AND CREATININE) อาจารย์ที่ปรึกษา : รองศาสตราจารย์ ดร.กมลวิชงามเชื้อ, 89 หน้า

คำสำคัญ: กัวโนซีน, ครีเอตินีน, ตัวบ่งชี้ทางชีวภาพ, เซ็นเซอร์, โวลแทมเมตรี

กัวโนซีนและครีเอตินีนเป็นตัวบ่งชี้ทางชีวภาพที่มีบทบาทสำคัญในกระบวนการที่เกี่ยวข้องกับความผิดปกติของระบบประสาทส่วนกลาง และการทำงานของไต ตามลำดับ งานวิจัยนี้ได้ศึกษาปฏิกิริยาออกซิเดชันของกัวโนซีนโดยใช้เทคนิคโวลแทมเมตรีที่ขั้วไฟฟ้าแบบนิ่งและแบบไฮโดรไดนามิก พร้อมทั้งใช้การคำนวณตามทฤษฎีฟังก์ชันนัลความหนาแน่นเพื่อทำความเข้าใจกลไกการเกิดออกซิเดชัน และได้พัฒนาเซนเซอร์สำหรับตรวจวัดกัวโนซีนด้วยขั้วไฟฟ้าคาร์บอนไฟเบอร์ โดยเซนเซอร์ที่พัฒนาขึ้นนี้มีช่วงความเป็นเส้นตรงสองช่วง ได้แก่ 0.0067–0.12 mM และ 0.12–1.00 mM มีค่าความไวในการวิเคราะห์ในแต่ละช่วงเท่ากับ  $1.40 \pm 0.03 \text{ nA mM}^{-1}$  และ  $0.05 \pm 0.003 \text{ nA mM}^{-1}$  ตามลำดับ มีค่าขีดจำกัดการตรวจวัดอยู่ที่ 0.002 mM มีความจำเพาะสูง ไม่มีสัญญาณรบกวนจากกลูโคส ครีเอตินีน ไอออนบวก ( $\text{Li}^+$ ,  $\text{Na}^+$ ,  $\text{K}^+$ ,  $\text{Mg}^{2+}$ ) และไอออนลบ ( $\text{Cl}^-$ ,  $\text{Br}^-$ ,  $\text{CO}_3^{2-}$ ,  $\text{SO}_4^{2-}$ ) และได้มีการทดสอบการใช้งานของเซนเซอร์ชนิดนี้ในการตรวจวัดกัวโนซีนในตัวอย่างปัสสาวะสังเคราะห์ โดยได้ค่าร้อยละการกลับคืนเท่ากับ  $99.71 \pm 4.02\%$  (RSD = 4.95%)

นอกจากเซนเซอร์สำหรับกัวโนซีนแล้ว งานวิจัยนี้ยังได้พัฒนาเซนเซอร์สำหรับตรวจวัดครีเอตินีน โดยใช้ขั้วไฟฟ้าทองมาดัดแปลงด้วยสารประกอบ Cu(II)-ImaSMe เซนเซอร์ที่พัฒนาขึ้นนี้มีช่วงความเป็นเส้นตรงอยู่ระหว่าง 0.14–20.0 mM ค่าขีดจำกัดการตรวจวัดอยู่ที่ 0.04 mM และค่าความไวในการวิเคราะห์เท่ากับ  $30.64 \pm 0.86 \mu\text{A mM}^{-1}$  เซนเซอร์ที่พัฒนาขึ้นมีความจำเพาะสูง ไม่มีสัญญาณรบกวนจากกรดแอสคอร์บิก กรดยูริก โดปามีน ยูเรีย แลคเตต อาร์จินีน และครีเอทีน และได้มีการทดสอบการใช้งานของเซนเซอร์ชนิดนี้ในการตรวจวัดครีเอตินีนในตัวอย่างปัสสาวะจริงจำนวน 3 ตัวอย่าง ได้ค่าร้อยละการกลับคืนเท่ากับ  $97.3 \pm 3.1\%$  (RSD = 1.59%),  $100.5 \pm 2.4\%$  (RSD = 6.25%), และ  $97.4 \pm 2.6\%$  (RSD = 7.31%) ซึ่งเซนเซอร์ทั้งสองชนิดได้รับการออกแบบมาเพื่อรองรับการตรวจวัดตัวบ่งชี้ทางชีวภาพในตัวอย่างชีวภาพได้อย่างแม่นยำและน่าเชื่อถือ เหมาะสำหรับการประยุกต์ใช้ในงานวิจัยและการวินิจฉัยทางการแพทย์

JINNAPAT WIJITSAK : CARBON AND COPPER COMPLEX ELECTRODES FOR THE  
DETECTION OF MOLECULAR BIOMARKERS: GUANOSINE AND CREATININE.  
THESIS ADVISOR : ASSOC. PROF. KAMONWAD NGAMCHUEA, Ph.D. 89 PP.

Keyword: Guanosine, Creatinine, Biomarker, Sensor, Voltammetry

Guanosine and creatinine are important biomarkers for central nervous system disorders and kidney functions, respectively. First, the oxidation of guanosine was studied using voltammetric techniques at stationary and hydrodynamic electrodes. Density functional theory (DFT) calculations were used to understand the oxidation mechanism. A carbon fiber microelectrode-based sensor was developed for guanosine detection. The sensor showed two linear detection ranges (0.0067–0.12 mM and 0.12–1.00 mM) with sensitivities of  $1.40 \pm 0.03 \text{ nA mM}^{-1}$  and  $0.05 \pm 0.003 \text{ nA mM}^{-1}$ . The detection limit was 0.002 mM. The developed sensor is highly selective, with no interference from glucose and creatinine, as well as cations like  $\text{Li}^+$ ,  $\text{Na}^+$ ,  $\text{K}^+$ ,  $\text{Mg}^{2+}$ , and anions such as  $\text{Cl}^-$ ,  $\text{Br}^-$ ,  $\text{CO}_3^{2-}$ ,  $\text{SO}_4^{2-}$ . Validation was performed with synthetic urine, and a recovery rate of  $99.71 \pm 4.02\%$  (RSD = 4.95%) was achieved.

In addition to a guanosine sensor, an electrochemical sensor was developed for creatinine detection. The sensor was based on a Cu(II)-ImaSMe complex-modified gold macroelectrode. A linear detection range of 0.14–20.0 mM, a detection limit of 0.04 mM, and a sensitivity of  $30.64 \pm 0.86 \mu\text{A mM}^{-1}$  were obtained. Selectivity was confirmed against interferences such as ascorbic acid, uric acid, dopamine, urea, lactate, arginine, and creatine. Recovery rates of  $97.3 \pm 3.1\%$  (RSD = 1.59%),  $100.5 \pm 2.4\%$  (RSD = 6.25%), and  $97.4 \pm 2.6\%$  (RSD = 7.31%) were achieved in three urine samples. These sensors are therefore suitable for accurate and reliable guanosine and creatinine detection in biological samples.

School of Chemistry  
Academic Year 2024

Student's Signature จินนพัทธ์ วิจิตรศักดิ์  
Advisor's Signature กมลวรรณ

## ACKNOWLEDGEMENTS

I would like to take this opportunity to express my profound gratitude to those who have supported and guided me throughout the course of this research.

First and foremost, I extend my deepest appreciation to my advisor, Assoc. Prof. Dr. Kamonwad Ngamchuea, for her exceptional guidance, insightful feedback, and unwavering encouragement. Her expertise has been instrumental in shaping the direction and quality of this work.

I am also deeply grateful to the members of my thesis committee, Assoc. Prof. Dr. Sanchai Prayoonpokarach, Dr. Suttipong Wannapaiboon, Assoc. Prof. Dr. Phimphaka Harding, and Asst. Prof. Dr. Patcharin Chaisuwan for their thoughtful critiques, valuable suggestions, and the time they dedicated to reviewing my work.

Special thanks are extended to Dr. Bunrat Tharat and Assoc. Prof. Dr. Suwit Suthirakun for their assistance with the DFT calculations related to the oxidation of guanosine. I would also like to express my gratitude to Dr. Theerapoom Boonprab, Assoc. Prof. Dr. Phimphaka Harding, and Assoc. Prof. Dr. David J. Harding for their support in synthesizing materials for use with modified electrodes, as well as for their help with the characterization of these materials using single-crystal X-ray diffraction (SCXRD), CHNS analysis, and the fitting of the EXAFS data in R-space to a scattering model derived from the SCXRD structure of the complex.

I would like to acknowledge the financial support provided by Suranaree University of Technology, which was essential for the successful completion of this research.

Lastly, I extend my heartfelt gratitude to my family, friends and SUT Electrochemistry Research Group for their constant encouragement, patience, and understanding throughout this journey. Their unwavering support has been a source of strength and motivation.

Jinnapat Wijitsak

# CONTENTS

	Page
ABSTRACT IN THAI.....	I
ABSTRACT IN ENGLISH.....	II
ACKNOWLEDGEMENTS .....	III
CONTENTS .....	IV
LIST OF TABLES .....	VIII
LIST OF FIGURES .....	IX
LIST OF ABBREVIATIONS.....	XIII
<b>CHAPTER</b>	
<b>I INTRODUCTION.....</b>	<b>1</b>
1.1 Research and background.....	1
1.1.1 Guanosine .....	1
1.1.2 Creatinine.....	3
1.2 Research objectives.....	4
<b>II LITERATURE REVIEWS.....</b>	<b>5</b>
2.1 Guanosine.....	5
2.1.1 Oxidative stress.....	5
2.1.2 Properties and clinical significance of guanosine.....	6
2.1.3 Analytical methods for the detection of guanosine.....	8
2.1.4 Mechanisms of guanosine electro-oxidation .....	11
2.2 Creatinine.....	12
2.2.1 Properties and clinical significance of creatinine .....	12
2.2.2 Gold standard methods for measuring creatinine.....	18
2.2.2.1 Alinity c Creatinine (Enzymatic) Reagent Kit.....	18
2.2.3 Analytical methods for the detection of creatinine .....	20
2.2.4 Cu(II)-ImaSMe complex.....	24
2.2.4.1 Electronic configuration of Cu(II) .....	24
2.2.4.2 Properties of Cu(II)-ImaSMe complex.....	25

## CONTENTS (Continued)

	Page
2.2.4.3 Example for Cu(II)-ImaSMe complex with sulfur Ligand .....	25
2.2.5 Copper(II)-creatinine complex formation.....	26
2.3 Detection and characterization methods .....	26
2.3.1 Cyclic voltammetry.....	26
2.3.2 Electrochemical impedance spectroscopy (EIS) .....	27
2.3.3 Scanning electron microscope (SEM).....	28
2.3.4 X-ray diffraction spectroscopy (XRD).....	29
2.3.5 X-ray adsorption spectroscopy (XAS).....	30
2.3.6 CHNS analysis.....	31
2.3.7 Thermogravimetry analysis (TGA).....	32
2.3.8 Ultraviolet-visible (UV-vis) spectroscopy.....	32
2.3.9 Fourier Transform Infrared (FTIR) spectroscopy .....	33
2.3.10 X-ray photoelectron spectroscopy (XPS).....	34
<b>III MATERIALS AND METHODS.....</b>	<b>35</b>
3.1 Guanosine detection .....	35
3.1.1 Chemical reagents.....	36
3.1.2 Electrochemical measurements.....	36
3.1.3 Computational detail.....	36
3.2 Creatinine detection.....	37
3.2.1 Chemical reagents.....	37
3.2.2 Synthesis of Cu(II)-ImaSMe.....	37
3.2.3 Characterization of Cu(II)-ImaSMe.....	38
3.2.4 Electrochemical studies.....	39
3.2.5 Creatinine analysis.....	39
<b>IV RESULTS AND DISCUSSION .....</b>	<b>40</b>
4.1 Guanosine detection .....	40
4.1.1 Cyclic voltammetry of guanosine at a stationary glassy carbon Electrode .....	40

## CONTENTS (Continued)

	Page
4.1.1.1 Tafel analysis.....	40
4.1.1.2 Effects of scan rates.....	41
4.1.1.3 Effects of pH.....	42
4.1.1.4 Calibration plots.....	43
4.1.2 Cyclic voltammetry of guanosine at a rotating glassy carbon Macroelectrode.....	44
4.1.3 Cyclic voltammetry of guanosine at a stationary carbon fiber microelectrode (CFE).....	45
4.1.4 Stationary glassy carbon macroelectrode vs. rotating glassy carbon macroelectrode vs. stationary carbon fiber microelectrode.....	46
4.1.5 Mechanistic studies by DFT calculation.....	47
4.1.6 Interference studies and application in synthetic urine samples.....	50
4.2 Creatinine detection.....	51
4.2.1 Physicochemical properties of Cu(II)-ImaSMe.....	51
4.2.2 Electrochemical properties the Cu(II)-ImaSMe complex in aqueous environment.....	60
4.2.2.1 Charge transfer resistances.....	60
4.2.2.2 Fingerprinting the redox processes.....	61
4.2.2.3 Effects of pH.....	62
4.2.2.4 Effects of potential scan rates.....	63
4.2.2.5 Multiple cycles.....	64
4.2.3 Application of Cu(II)-ImaSMe in creatinine analysis.....	65
4.2.3.1 Voltammetry of creatinine at Cu(II)-ImaSMe/Au.....	65
4.2.3.2 Effects of potential scan rates on creatinine analysis.....	66
4.2.3.3 Calibration plots.....	67
4.2.3.4 Reproducibility and selectivity studies.....	67
4.2.3.5 Application to synthetic urine sample.....	69
4.2.3.6 Application to real urine samples.....	70

## CONTENTS (Continued)

	Page
V CONCLUSION.....	71
REFERENCES.....	73
CURRICULUM VITAE.....	89



## LIST OF TABLES

Table	Page
2.1 Electrochemical sensors for guanosine detection.....	9
2.2 Stages of chronic kidney disease (CKD) .....	13
2.3 Specimen collection and preparation for analysis.....	19
2.4 Specimen storage.....	20
2.5 Analytical methodologies reported for the detection of creatinine .....	21
2.6 Electrochemical sensors for creatinine detection .....	22
4.1 Spike and recovery tests of guanosine in synthetic urine .....	51
4.2 Bond lengths and geometry parameters of the Cu(II)-ImaSMe complex .....	52
4.3 Comparison of electrochemical sensors for creatinine detection.....	68
4.4 Comparison of the Cu(II)-ImaSMe/Au sensor and Jaffe method for creatinine measurement in real urine samples .....	70

## LIST OF FIGURES

Figure	Page
2.1 Schematic representation of DNA damage caused by reactive oxygen species (ROS).....	6
2.2 Chemical structure of guanosine.....	7
2.3 a) Neuroprotective effects of guanosine. b) Neurotrophic effects of guanosine.....	8
2.4 Proposed electrochemical oxidation pathways of purine nucleosides and oligonucleotides.....	12
2.5 Chemical structure of creatinine.....	13
2.6 An example illustrating the dependency of serum creatinine levels on age and gender.....	14
2.7 Illustration depicting the relationship between serum creatinine levels and age/gender dependency.....	14
2.8 An example depicting the relationship between serum creatinine levels and muscle mass.....	15
2.9 Preparation of ligand and its copper complex.....	25
2.10 a) A plot of the applied potential with time in CV. b) Cyclic voltammogram. c) Setup of three-electrode in electrochemical.....	27
2.11 A simple scheme to describe the EIS circuit and the redox reaction takes place at the surface of working electrodes in a conventional electrochemical cell.....	28
2.12 Schematic diagram of the core components of an SEM microscope.....	29
2.13 Schematic of the experimental principle for X-ray diffraction.....	30
2.14 Separation into the XANES and EXAFS range. And on the right the corresponding energy level diagram with the associated transitions.....	31
2.15 CHNS/O configuration.....	31
2.16 Scheme of thermogravimeter.....	32
2.17 Schematic diagram of the UV-Visible Spectrophotometer.....	32
2.18 Principle and instrumental of Fourier transform infrared (FTIR) spectroscopy.....	33

## LIST OF FIGURES (Continued)

Figure	Page
2.19 Schematic diagram of the instrumental operation of the X-ray photoelectron spectroscopy (XPS) .....	34
4.1 Cyclic voltammogram of 1.0 mM guanosine at a stationary glassy carbon macroelectrode in a PBS buffer solution pH 7.0 a) at a scan rate of 10 mV s <sup>-1</sup> . The inlay shows the plot of ln <i>I</i> vs. <i>E</i> in Tafel analysis, b) at different scan rates (10 – 400 mV s <sup>-1</sup> ). The inlay shows the plot of peak currents ( <i>I<sub>p</sub></i> ) against the square root of scan rates ( $\nu^{1/2}$ ) .....	41
4.2 Cyclic voltammograms of 1.00 mM guanosine at a stationary glassy carbon macroelectrode in buffer solutions of different pH (from 1.0 to 14.0) at a scan rate of 100 mV s <sup>-1</sup> . The inlay shows the plot of peak potentials ( <i>E<sub>p</sub></i> ) against pH.....	43
4.3 a) Cyclic voltammograms at a scan rate of 100 mV s <sup>-1</sup> and b) chronoamperograms at the applied potential of 1.20 V at a stationary glassy carbon macroelectrode of varied concentrations of guanosine in a PBS buffer solution pH 7.0. The inlays show the calibration plots of a) peak currents ( <i>I<sub>p</sub></i> ) and b) the background subtracted amperometric currents at 10 s ( <i>I<sub>(t=10s)</sub></i> – <i>I<sub>b</sub></i> ) against the concentrations of guanosine .....	44
4.4 a) Cyclic voltammograms of 1.00 mM guanosine in a pH 7.0 PBS buffer solution at a rotating glassy carbon macroelectrode at various electrode rotation speeds ( $\omega = 0 - 1500$ rpm). b) The Levich plots of <i>I<sub>lim</sub></i> vs $\omega^{1/2}$ .....	45
4.5 Cyclic voltammograms at a stationary carbon fiber microelectrode of varied guanosine concentrations (0.00 – 1.00 mM) in a pH 7.0 PBS buffer solution at a scan rate of 10 mV s <sup>-1</sup> . The inlay shows the calibration plot of peak currents ( <i>I<sub>p</sub></i> ) against guanosine concentrations.....	46
4.6 a) The calculated energy profile for guanosine oxidation in an aqueous solution. b) The proposed reaction mechanism of guanosine oxidation .....	49

## LIST OF FIGURES (Continued)

Figure	Page
4.7 a) Cyclic voltammograms of 1.00 mM guanosine in PBS pH 7.0 in the absence and presence of interferences at a stationary carbon fiber microelectrode at a scan rate of 10 mV <sup>-1</sup> . b) The analysis of $(I_{p,mixture} - I_{p,control}) \times 100 / I_{p,control}$ for different interfering species .....	50
4.8 Asymmetric unit and amphiphilic-like packing of the Cu(II)-ImaSMe complex.....	53
4.9 Powder XRD of Cu(II)-ImaSMe complex.....	53
4.10 a) structure of Cu(II)-ImaSMe complex, b) Cu K-edge EXAFS data and, c) model fitting in <i>R</i> -space and <i>k</i> -space alongside with the atoms contributing to the scattering path .....	54
4.11 XPS spectra of the Cu(II)-ImaSMe complex are presented, illustrating the peaks for a) Cu 2p, b) C 1s, c) N 1s, d) S 2p, and e) S 2p, both before and after electrochemical detection of creatinine .....	55
4.12 a) SEM image of Cu(II)-ImaSMe. and size distribution from SEM imaging. b) Thermogravimetric analysis (TGA) curve (black line) and Differential Thermogravimetric Analysis (DTG) curve (blue line) of Cu(II)-ImaSMe. c) FT-IR spectra of powder ImaSMe ligand (black line) and Cu(II)-ImaSMe (red line). d) UV-vis spectra of Cu(II)-ImaSMe. e) UV-vis spectra of ImaSMe ligand.....	58
4.13 Cyclic voltammograms of 1.0 mM Cu(II)-ImaSMe complex (pink line) and 1.0 mM ImaSMe ligand (blue line) in acetonitrile with 0.10 M TBAPF <sub>6</sub> at a scan rate of 100 mV s <sup>-1</sup> . Solid lines indicate the presence of ferrocene, while dashed lines correspond to the absence of ferrocene .....	60
4.14 a) EIS spectra of the bare gold electrode, ImaSMe/Au, and Cu(II)-ImaSMe/Au in 5.0 mM [Fe(CN) <sub>6</sub> ] <sup>3-/4-</sup> and 0.10 M KCl aqueous solution. The inlay shows Randle's equivalent circuit used for fitting the EIS data. b) Cyclic voltammograms of Cu(II)-ImaSMe/Au in B-R buffer pH 2.00 aqueous solution at a scan rate of 50 mV s <sup>-1</sup> .....	62

## LIST OF FIGURES (Continued)

Figure	Page
4.15 a) Cyclic voltammograms of ImaSMe/Au and b) Cu(II)-ImaSMe/Au electrode in B-R buffer aqueous solution at a scan rate of $50 \text{ mV s}^{-1}$ at various pH.....	63
4.16 a) Cyclic voltammograms of ImaSMe b) Cu(II)-ImaSMe dropcasted on gold electrode in B-R buffer pH 2.00 aqueous solution at various scan rates .....	64
4.17 a) Cyclic voltammetry of multiple cycles at ImaSMe/Au and b) Cu(II)-ImaSMe/Au B-R buffer pH 2.00 aqueous solution at a scan rate of $50 \text{ mV s}^{-1}$ .....	65
4.18 Cyclic voltammograms of Cu(II)-ImaSMe complex dropcasted on gold macroelectrode in various creatinine concentrations in B-R buffer pH 2.0 containing 0.10 M KCl aqueous solution at a scan rate of $50 \text{ mV s}^{-1}$ .....	66
4.19 a) Cyclic voltammograms of 20.0 mM creatinine at bare Au electrode modified Au electrode with ImaSMe ligand and Cu(II)-ImaSMe at a scan rate of $50 \text{ mV s}^{-1}$ b) Cyclic voltammograms of Cu(II)-ImaSMe electrode in 10.0 mM creatinine containing 0.10 M KCl aqueous solution at various scan rates .....	67
4.20 a) CV of various creatinine concentrations containing 0.10 M KCl at Cu(II)-ImaSMe/Au electrode at a scan rate of $50 \text{ mV s}^{-1}$ . Inlay: Plot of peak currents ( $I_p$ ) vs. creatinine concentrations. b) Peak currents of creatinine at Cu(II)-ImaSMe/Au electrode in the presence and absence of interfering species.....	68

## LIST OF ABBREVIATIONS

AMP	Amperometry
B3LYP	Becke, 3-parameter, Lee-Yang-Parr
BUN	Blood urea nitrogen
CB	Carbon black
$C_{dl}$	Layer capacitance
CFE	Carbon fiber microdisk electrode
CHF	Congestive heart failure
CKD	Chronic kidney disease
CNS	Central nervous system
CPE	Carbon-paste electrode
CV	Cyclic voltammetry
DFT	Density functional theory
DM	Diabetes mellitus (DM),
DPV	Differential pulse voltammetry
$E$	Potential
eGFR	Estimated glomerular filtration rate
EIS	Electrochemical impedance spectroscopy
ESPMT*	N-ethyl-N-sulfopropyl-m-toluidine
EXAFS	Extended X-ray absorption fine structure
$\epsilon$	Solvation effects
F	Faraday constant
FBG	Fasting blood sugar
FTIR	Fourier Transform Infrared
GC	Glassy carbon electrode
GCE	Glassy carbon electrode
$h$	Planck's constant
$I$	Current
ImaSMe:	( <i>E</i> )-N-((1H-imidazol-4-yl)methylene)-4 (methylthio)aniline
$I_p$	Peak current

## LIST OF ABBREVIATIONS (Continued)

LSV	Linear sweep voltammetry
LUMO	Highest occupied molecular orbital
LUMO	Lowest unoccupied molecular orbital
$m$	Number of protons transfer, Slope of calibration plot
MEA	Microelectrode arrays molecularly-imprinted polymer
MGCE	Modified glassy carbon electrode
MI	Myocardial infarction
MWCNT	Multiwall carbon nanotube
$n$	Number of electron transfer
NPs	Nanoparticles
NSAIDs	Nonsteroidal anti-inflammatory drug
PAA	Polyacrylic acid
PANI	Polyaniline
PHS	Phenoxazinone synthase
R	Gas rate constant
RA	Rheumatoid arthritis
$R_{ct}$	Electron transfer resistance
RDE	Rotating glassy carbon macrodisk electrode
ROS	Reactive oxygen species
$R_s$	Resistance of the electrolyte solution
RSD	Relative standard deviation
$S_B$	Standard deviation of blank
SCXRD	Single-crystal X-ray diffraction
SEM	Scanning electrode microscope
SLE	Systemic lupus erythematosus
SPCE	Screen printed carbon electrode
SPE	Screen printed electrode
SWV	Square wave voltammetry
$T$	Temperature

## LIST OF ABBREVIATIONS (Continued)

TGA	Thermogravimetry analysis
UMA	Urine microalbumin
UV–vis	Ultraviolet–visible
V	Voltage
XANES	X-ray absorption near-edge structure
XAS	X-ray adsorption spectroscopy
XPS	X-ray photoelectron spectroscopy
$Z_w$	Warburg resistance arising from the diffusion process
$\tau_5$	tau-5
$A$	Electrode surface area
$D$	Diffusion coefficient.
$c$	Speed of light
$c^*$	Concentration at the electrode surface
$E_{H^+}$	Energy of $H^+$
$E^0$	Formal potential, standard electrode potential
$E_R$	Total energies of reactant
$E_g$	Energy gap
$E_p$	Peak potentials, Total energies of product
$I_{lim}$	Limiting current
$k^0$	Standard heterogeneous electron transfer rate constant
$n'$	Number of electrons transferred before the rate determining electron transfer step
$\beta_{n'+1}$	Anodic transfer
$\lambda_{onset}$	Wavelength at the absorption
$\text{Å}$	Angstrom
$\Gamma$	Surface coverage of the electroactive species
$\beta$	Anodic transfer coefficient
$\nu$	Kinetic viscosity, Scan rate
$\omega$	Electrode rotation speed

# CHAPTER I

## INTRODUCTION

### 1.1 Research and background

Guanosine and creatinine, though differing in their specific roles within biological systems, share several notable similarities that underline their importance in metabolism and diagnostics. Both molecules are nitrogen-rich compounds, with guanosine featuring a nitrogenous purine base and creatinine containing a cyclic amide structure, reflecting their biochemical origins. They are water-soluble due to their polar functional groups, enabling their transport and excretion in biological fluids such as urine. Additionally, both are involved in energy-related processes-guanosine as part of guanosine triphosphate (GTP) in cellular energy transfer and creatinine as a byproduct of creatine phosphate metabolism in muscle tissues. Their shared electroactive and UV-absorbing properties also make them detectable and quantifiable using similar analytical techniques, such as spectroscopy and electrochemical methods. These commonalities highlight their interconnected roles in metabolic processes and their significance in physiological studies and clinical assessments.

#### 1.1.1 Guanosine

Oxidative stress, neuroinflammation, and glutamatergic excitotoxicity are prevalent characteristics of various neurological conditions. The brain, with its high oxygen consumption and lipid content, is particularly vulnerable to oxidative stress, leading to adverse effects on central nervous system (CNS) functions. This vulnerability contributes to the development of CNS diseases such as ischemic stroke, Alzheimer's disease, Parkinson's disease, spinal cord injury, nociception, and depression. (Salim, 2017) Consequently, biomolecules involved in oxidative stress and CNS functions have emerged as promising candidates for the diagnosis and treatment of CNS diseases. (Lanznaster, Dal-Cim, Piermartiri, and Tasca, 2016) Among these biomolecules, guanosine has demonstrated therapeutic potential in *in vitro* and *in vivo* models of several neurological pathologies.

Guanosine administration exhibits low toxicity, minimal side effects, and can effectively reach the central nervous system through systemic and oral routes. Therefore, the monitoring of guanosine levels is crucial for early recognition and timely therapeutic intervention in CNS diseases.

Guanosine is a purine nucleoside comprised of guanine attached to ribofuranose via a beta-N(9)-glycosidic bond. It plays significant roles in cellular metabolism, nucleic acid and protein synthesis, RNA production, and acts as an intercellular messenger in the central nervous system. Guanosine promotes neuroprotection by reducing levels of reactive oxygen species (ROS) through inhibition of nuclear factor kappa B activation, preventing inducible nitric oxide synthase induction, and enhancing antioxidant defenses such as glutathione and superoxide dismutase activity. (Lanznaster, Dal-Cim, Piermartiri, and Tasca, 2016) Moreover, guanosine reduces extracellular glutamate levels and safeguards against glutamate excitotoxicity, a cell death mechanism triggered by excessive glutamate release. (Lanznaster, Dal-Cim, Piermartiri, and Tasca, 2016) Guanosine has attracted considerable interest as a biomarker of oxidative stress (Bolin and Cardozo-Pelaez, 2007) and CNS diseases such as Alzheimer's disease, (Ugarte et al., 2015) Parkinson's disease, (Giuliani et al., 2012) and Segawa disease. (Segawa, Nomura, and Nishiyama, 2003) The compound has also been reported to associate with airborne and systemic exposure to metals in welders. (Pesch et al., 2015) The concentrations of guanosine in healthy human bodily fluids are  $1.10 \pm 0.06 \mu\text{M}$  in blood plasma and  $0.39 \pm 0.24 \mu\text{mol/g}$  of creatinine in urine. (R. N. Goyal, Oyama, and Tyagi, 2007; Jakob et al., 1994)

Various techniques have been developed for guanosine detection, including high performance liquid chromatography, (Pilger, Ivancsits, Germadnik, and Rüdiger, 2002) capillary electrophoresis, (Kvasnicová, Samcová, Jursová, and Jelínek, 2003) gas chromatography, (Mei, Xu, Xing, and WU, 2001) and fluorescence. (Kai, Ohkura, Yonekura, and Iwasaki, 1988) However, these methods have limited applicability for point-of-care testing and on-site monitoring due to challenges associated with sample preparation, time-intensive analysis, costly reagents, and complex instrumentation. Meanwhile, electrochemical methods offer a simple and practical solution for the detection of guanosine and purine-based species due to their low cost, ease of operation, robustness, rapid measurement, high sensitivity, wide detection range, portability, and potential for integration into wearable devices for real-time monitoring. (Sarioğulları, Şenocak, Basova, Demirbaş, and Durmuş, 2019; Şenocak, Korkmaz, Khataee, and Demirbas, 2022; Şenocak et al., 2022; Şenocak, Tümay, Ömeroğlu, and Şanko, 2022; Tümay et al., 2023) Therefore, the objective of this study

is to establish a rapid, straightforward, and cost-effective electrochemical approach for the detection of guanosine.

Electrochemically, guanosine can be detected from its oxidation responses. However, the oxidation process of guanosine is complex and not yet fully understood. Furthermore, this process is of significant relevance in biological systems. Understanding guanosine oxidation is valuable for two primary purposes: enhancing our comprehension of guanosine's role within biological systems and facilitating the development of guanosine sensors. To unravel the underlying mechanism of guanosine oxidation, a comprehensive analysis extending beyond experimental observations is required. To determine the most favorable reaction pathway, this work employs a combination of density functional theory (DFT) calculations and cyclic voltammetry experiments conducted at both stationary and hydrodynamic electrodes. By integrating theoretical calculations and experimental data, a more comprehensive understanding of the guanosine oxidation process can be achieved.

In parallel to investigating the mechanism of guanosine oxidation, this study also aims to develop an electrochemical sensor utilizing a carbon microfiber electrode.

### 1.1.2 Creatinine

Creatinine is a natural component of muscle tissues and blood, stemming from its ongoing generation as a metabolic byproduct during muscle breakdown, and is typically eliminated from the body through urine. (Persson and Rossing, 2018) It is evident that creatinine levels correlate with the estimated glomerular filtration rate, which is crucial for diagnosing a range of renal and muscular conditions. (Rakesh Kumar, Shaikh, Kumar, Liu, and Chuang, 2023) Creatinine is among the most frequently analyzed biomolecules in clinical settings, especially in the context of chronic kidney disease. As a result, it is extensively studied and monitored, often following glucose in terms of clinical significance. (Kashani, Rosner, and Ostermann, 2020)

In the past, creatinine was typically assessed in centralized laboratories through the costly and labor-intensive colorimetric Jaffe method. However, when evaluating factors like cost-efficiency, dependability, and simplicity, biosensors emerge as a viable option for conducting creatinine tests at the point of care. (Pundir, Kumar, and Jaiwal, 2019) The presence of multiple bonding sites in the creatinine molecule improves its capacity to form complex with various redox-active metallic centers, such as Zn(II) (Chhillar, Kukkar, Deep, Yadav, and Kim, 2023; Kushwaha et al., 2024), Co(II) (Dasgupta, Kumar, Krishnaswamy, and Bhat, 2020; Meera, Neena, Pradeep, Nair, Vasu, and Babu, 2024), Ni(II) (Babamiri, Salimi, Hallaj, and Hasanzadeh, 2018), and Cu(II) (X.

Gao, Gui, Guo, Wang, and Liu, 2019). In this work Cu(II) was chosen as it have been reported to have improved affinity toward complexation with creatinine, which typically undergoes via a redox-active site facilitated by a simple process of physical adsorption. (R. R. Kumar, Shaikh, and Chuang, 2021)

This work synthesizes Cu(II)-complex with an imidazole-based histidine ligand, (*E*)-N-((1H-imidazol-4-yl)methylene)-4-(methylthio)aniline, shortened as ImaSMe. This Cu(II)-ImaSMe complex will subsequently be immobilized on a gold macroelectrode as the underlying surface to avoid interference with any weak redox signals that may arise from the electrode surface (L. Wang, Wang, and Zhou, 2004). Additionally, it functions as a substrate binder through interactions with the ImaSMe ligand. This modified electrode is then utilized for creatinine analysis.

## 1.2 Research objectives

- 1.2.1 To study the electrochemical properties of guanosine at a glassy carbon macrodisk (GCE), a glassy carbon rotating disk (RDE), and a carbon fiber microdisk (CFM).
- 1.2.2 To develop an electrochemical sensor for guanosine detection using carbon-based electrodes.
- 1.2.3 To synthesize and investigate the physicochemical and electrochemical properties of the Cu(II)-ImaSMe complex and the ImaSMe ligand.
- 1.2.4 To study the electrochemical reactions of creatinine at the Cu(II)-ImaSMe complex modified gold macroelectrode.
- 1.2.5 To develop an electrochemical sensor for the determination of creatinine based on the use of the Cu(II)-ImaSMe complex.

## CHAPTER II

### LITERATURE REVIEWS

#### 2.1 Guanosine

##### 2.1.1 Oxidative stress

Oxidative stress is caused by the loss in homeostatic balance between the production and accumulation of reactive oxygen species (ROS) in cells and tissues. The commonly found ROS in biological systems include superoxide radicals ( $O_2^{\cdot-}$ ), hydrogen peroxide ( $H_2O_2$ ), hydroxyl radicals ( $\cdot OH$ ), and singlet oxygen ( $^1O_2$ ). ROS are generated from both endogenous and exogenous sources. Endogenously, ROS are formed as by-products during the process of cellular respiration and enzymatic metabolism. Exposure to environmental pollutants, heavy metals, smokes, alcohol, radiations, and certain drugs are responsible for the exogenous intake of ROS. (Pizzino et al., 2017)

The reactions with ROS can induce extensive protein oxidation, lipid peroxidation, and DNA damage such as single- and double-strand breaks, base oxidation, and intra- and inter-strand crosslinks (Figure 2.1). (Chiorcea-Paquim and Oliveira-Brett, 2021) High ROS concentrations in brain can diminish long-term potentiation, synaptic signaling, and brain plasticity mechanisms. For example, the ROS-mediated production of amyloid  $\beta$  causes impaired membrane permeability and activates excitotoxicity mechanisms, which alter the neurotransmission and cognitive functions. ROS accumulation or oxidative stress is thus a cellular threat that can cause significant neuronal damage especially in hippocampus, amygdala, and cerebellar granule cells which are the most susceptible to oxidative stress parts of the brain. In addition to CNS diseases, oxidative damage is directly related to the pathogenesis of various diseases such as cancer, diabetes mellitus, Down's syndrome, Fanconi's anemia, rheumatoid arthritis, aging, etc. (Cooke, Evans, Dizdaroglu, and Lunec, 2003)

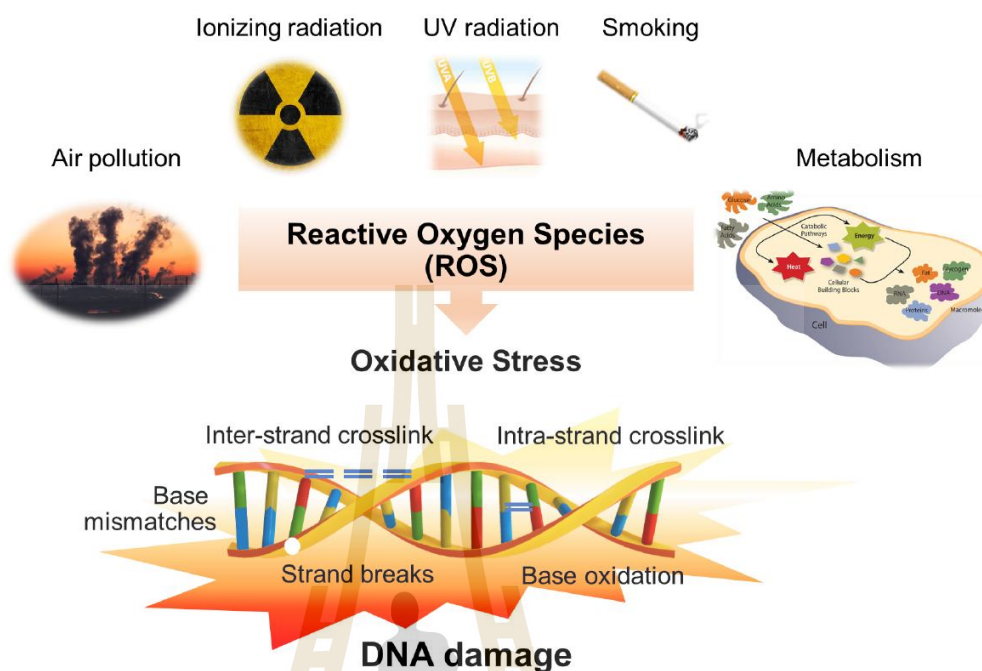


**Figure 2.1** Schematic representation of DNA damage caused by reactive oxygen species (ROS).

### 2.1.2 Properties and clinical significance of guanosine

Guanosine (Figure 2.2) is a purine nucleoside in which guanine is attached to ribofuranose via a beta-N(9)-glycosidic bond. It plays important roles in cell metabolisms, synthesis of nucleic acids, proteins, RNA, and acts as an intercellular messenger in the central nervous system. Guanosine can be phosphorylated to become guanosine monophosphate (GMP), cyclic guanosine monophosphate (cGMP), guanosine diphosphate (GDP), and guanosine triphosphate (GTP) which are factors in signal transduction pathways.

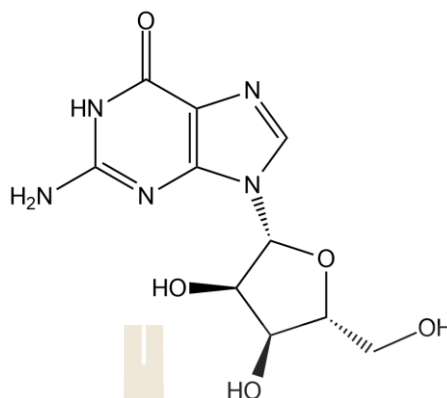


**Figure 2.2** Chemical structure of guanosine.

Guanosine promotes neuroprotection through reduction of ROS levels by i) inhibiting nuclear factor kappa B activation, ii) preventing inducible nitric oxide synthase induction, iii) increasing antioxidant defenses such as glutathione and superoxide dismutase activity (Figure 2.3a). (Lanznaster, Dal-Cim, Piermartiri, and Tasca, 2016) Guanosine also reduces extracellular levels of glutamate and protects against glutamate excitotoxicity (cell death mechanism triggered by excessive glutamate release). (Lanznaster, Dal-Cim, Piermartiri, and Tasca, 2016) Guanosine also displays neurotrophic effects by i) promoting the reorganization of extracellular matrix proteins fibronectin and laminin, ii) increasing the number of cerebellar neurons in culture, iii) increasing intracellular cAMP, CREB phosphorylation, and BDNF mRNA levels, iv) promoting cellular proliferation and the synthesis and release of neurotrophic factors (Figure 2.3b). (Lanznaster, Dal-Cim, Piermartiri, and Tasca, 2016)

Guanosine has attracted considerable interest as a biomarker of oxidative stress (Bolin and Cardozo-Pelaez, 2007) and CNS diseases such as Alzheimer's disease, (Ugarte et al., 2015) Parkinson's disease, (Giuliani et al., 2012) Segawa disease. (Segawa, Nomura, and Nishiyama, 2003) The compound has also been reported to associate with airborne and systemic exposure to metals in welders. The concentrations of guanosine in healthy human bodily fluids are  $1.10 \pm 0.06 \mu\text{M}$  in blood plasma and  $0.39 \pm 0.24 \mu\text{mol/g}$  of creatinine in urine. (R. N. Goyal, Oyama, and Tyagi, 2007; Jakob et al., 1994)

The importance of guanosine monitoring has thus been demonstrated. In the next section, the detection methods of guanosine will be discussed.



**Table 2.1** Electrochemical sensors for guanosine detection.

Electrode	Method	pH	Linear range	Limit of detection	Ref.
Fullerene-C <sub>60</sub> -modified glassy carbon	DPV	7.2	0.5×10 <sup>-6</sup> to 1.0×10 <sup>-3</sup> M	1.45×10 <sup>-7</sup> M	(R. N. Goyal, Gupta, Oyama, and Bachheti, 2007)
Gold nanoparticles modified indium tin oxide	DPV	7.2	0.1×10 <sup>-6</sup> to 10×10 <sup>-6</sup> M	9.8×10 <sup>-8</sup> M	(R. N. Goyal, Oyama, and Tyagi, 2007)
Multi-walled carbon nanotubes modified carbon ionic liquid	CV, DPV	5.0	1.0×10 <sup>-6</sup> to 4.0×10 <sup>-5</sup> M	7.8×10 <sup>-8</sup> M	(W. Sun, Li, Duan, and Jiao, 2009)
N-butylpyridinium hexafluorophosphate modified carbon paste	CV	4.5	1.0×10 <sup>-6</sup> to 1.0×10 <sup>-4</sup> M	2.61×10 <sup>-7</sup> M	(W. Sun, Duan, Li, Gao, and Jiao, 2009)
Carbon paste electrode modified with 1-ethyl-3-methylimidazolium ethylsulfate	DPV	3.5	1.0×10 <sup>-6</sup> to 1.6×10 <sup>-4</sup> M	1.83×10 <sup>-7</sup> M	(H. Gao, Duan, Xi, and Sun, 2011)
Graphene, chitosan and Fe <sub>3</sub> O <sub>4</sub> nanoparticles modified glassy carbon	DPV	7.0	2.0×10 <sup>-6</sup> to 3.5×10 <sup>-4</sup> M	7.5×10 <sup>-7</sup> M	(Yin, Zhou, Ma, Ai, Chen, and Zhu, 2010)

**Table 2.1** Electrochemical sensors for guanosine detection (Continued).

Electrode	Method	pH	Linear range	Limit of detection	Ref.
Oleylamine capped CuO nanoparticles on multi-walled carbon nanotubes	CV, AMP	7.0	$0.3 \times 10^{-6}$ to $1.89 \times 10^{-5}$ M	$8.4 \times 10^{-8}$ M	(D. R. Kumar, Manoj, and Santhanalakshmi, 2013)
Graphene-ZrO <sub>2</sub> nanocomposite modified carbon ionic liquid	DPV	6.0	$0.4 \times 10^{-6}$ to $2.0 \times 10^{-4}$ M	$1.23 \times 10^{-7}$ M	(W. Sun et al., 2013)
Hierarchical and hollow boron/nitrogen co-doped yolk-shell mesoporous carbon nanospheres attached to reduced graphene oxide	DPV	7.0	$8.22 \times 10^{-8}$ to $1.28 \times 10^{-4}$ M	$4.62 \times 10^{-8}$ M	(Zhu, Chu, et al., 2021)
In situ hierarchical encapsulation of bimetallic selenides into honeycomb-like nitrogen doped porous carbon nanosheets multi-walled carbon nanotubes	DPV	7.0	$5.30 \times 10^{-8}$ to $2.27 \times 10^{-4}$ M	$1.20 \times 10^{-8}$ M	(Zhu, Zhen, et al., 2021)

(AMP: Amperometry, CV: Cyclic voltammetry, DPV: Differential pulse voltammetry)

Despite its potential applications, the commercialization of electrochemical sensors for health monitoring remains challenging. The difficulty of electrochemical measurement in biological samples lies in the production of reproducible and robust electrodes, and the requirement of supporting (redox-inert) electrolytes such as KCl,

$\text{KNO}_3$ , and  $\text{NaClO}_4$ . Typically, supporting electrolytes of up to 100 times in excess of the redox analyte are required at macroscopic electrodes for the systems to be considered diffusion-only. (Dickinson, Limon-Petersen, Rees, and Compton, 2009; Toh, Batchelor-McAuley, Tschulik, Uhlemann, Crossley, and Compton, 2013; Ward Jones, Campbell, Baron, Xiao, and Compton, 2008) Under insufficient electrolytic supports, the analysis of electrochemical responses is complicated due to the contribution of migration. Significant distortion of voltammetry also occurs in the absence of supporting electrolytes due to Ohmic drop and the alteration in the electrical double layer, reducing the accuracy and sensitivity of the measurement.

The ionic strength of urine is approximately 0.2 M, with the strength decreasing with age. (Hesse, Classen, Knoll, Timmermann, and Vahlensieck, 1986) To overcome the limitations arising from relatively low ionic strengths of urine samples, this project thus develops electrodes and methodology based on the use of microscopic electrodes for direct *in-vitro* measurements in urine samples. The use of a microscopic electrode relaxes the requirement of electrolytic support (passing low currents which typically require only 30 times in excess of the redox analyte), (Ngamchuea, Batchelor-McAuley, and Compton, 2018) making it practical for medical applications.

#### 2.1.4 Mechanisms of guanosine electro-oxidation

The electrochemical oxidation of guanosine occurs via the formation of an 8-oxoderivative intermediate which mimic the primary effects of oxidative stress in biological systems. This then leads to the formation of a number of different products such as diimine species and 5-guanidinohydantoin. Some of the products can adsorb on electrode surfaces such as pyrolytic graphite and gold, strongly affecting the measured electrochemical signals. (de-los-Santos-Álvarez, de-los-Santos-Alvarez, Lobo-Castañón, López, Miranda-Ordieres, and Tuñón-Blanco, 2007; González-Fernández, de-los-Santos-Álvarez, Lobo-Castañón, Miranda-Ordieres, and Tuñón-Blanco, 2008; Oliveira-Brett, Silva, and Brett, 2002) The proposed oxidation mechanisms of guanosine and purine nucleosides and oligonucleotides in general are presented in Figure 2.4.

The electrochemical responses and the stoichiometry of the formed products depend on the choice of voltage scan rates which allows different times for the chemical steps (as opposed to the electrochemical electron transfer steps) such as electrolysis to occur. The pH of the solution also plays important role in determining the electrochemical responses and the species generated due to the influence of

protons in many steps of the reactions. In the development of an electrochemical sensor for guanosine detection, it is thus highly important to understand the effects of electrochemical and chemical parameters such as scan rates, pH, adsorption conditions, electrode materials and geometries, etc. to develop the most efficient and selective sensor. The understanding of the redox properties of guanosine could also potentially explain how the compound contributes to the pathogenesis of the relevant diseases.

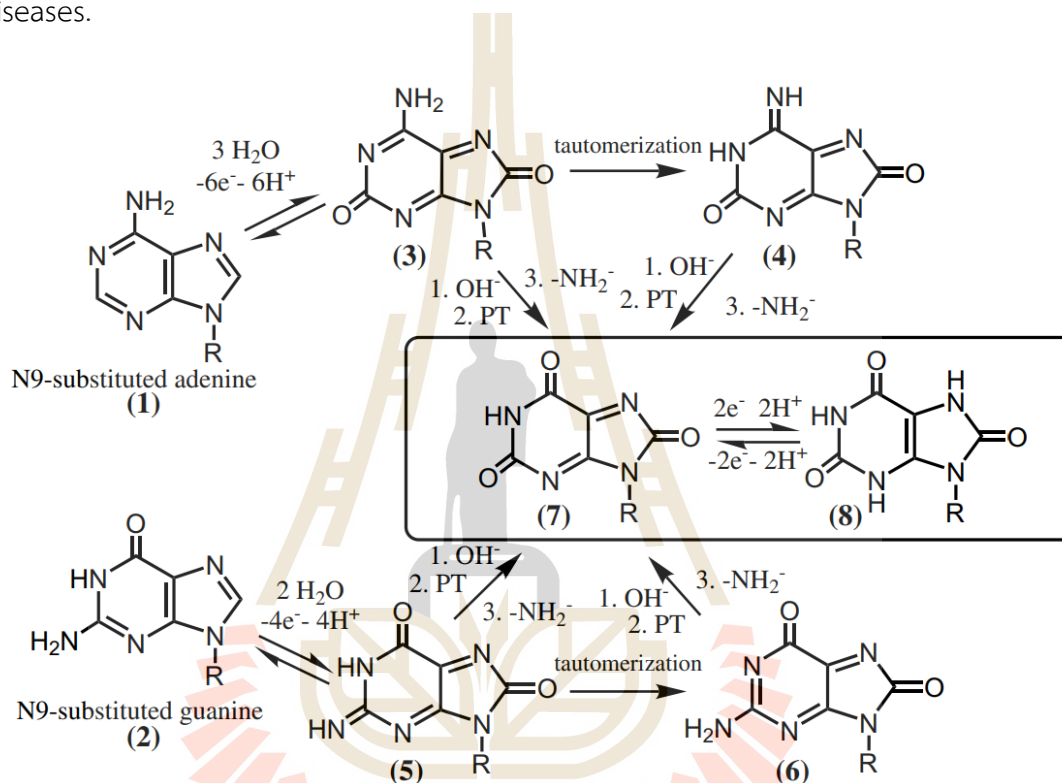


**Figure 2.4** Proposed electrochemical oxidation pathways of purine nucleosides and oligonucleotides. (de-los-Santos-Álvarez, de-los-Santos-Alvarez, Lobo-Castañón, López, Miranda-Ordieres, and Tuñón-Blanco, 2007)

## 2.2 Creatinine

### 2.2.1 Properties and clinical significance of creatinine

Creatinine or 2-Amino-1-methyl-5H-imidazol-4-one (Figure 2.5) is a breakdown product of creatine phosphate from muscle and protein metabolism, which is filtered out of the blood by the kidneys and excreted in urine. In clinical laboratories, the measurement of creatinine levels in biological fluids is routinely conducted to evaluate various physiological conditions such as renal function, muscle damage, nutritional status, and thyroid function. (V. Kumar et al., 2017)

In addition, creatinine levels are also associated with the estimated glomerular filtration rate (eGFR), based on which organizations such as the Kidney Foundation in New York classify five different stages of chronic kidney disease (CKD) according to the information in Table 2.2 (Bauer, Melamed, and Hostetter, 2008)

**Table 2.2** Stages of chronic kidney disease (CKD).

Stage	GFR (mL/min per 1.73 m <sup>2</sup> )*	Description
1	≥90	Kidney damage with normal or increased GFR
2	60 to 89	Kidney damage with mild decreased GFR
3	30 to 59	Moderate decreased GFR
4	15 to 29	Severe decreased GFR
5	<15 or dialysis	Kidney failure

\* GFR: glomerular filtration rate. Estimates of glomerular filtration rate are normally expressed per 1.73 m<sup>2</sup> body surface area, which is an average surface area for an adult.

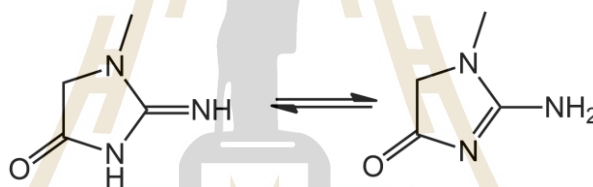


**Figure 2.5** Chemical structure of creatinine.

The normal clinical range for serum creatinine is 0.63 – 1.16 mg/dL for men and 0.48 – 0.93 mg/dL for women. (Delanaye, Cavalier, and Pottel, 2017) However, serum creatinine levels can vary based on age and gender, as indicated by existing literature. After birth, serum creatinine levels rapidly decrease to approximately 0.25 mg/dL within the first month of life. Following this initial decline, serum creatinine levels begin to increase linearly with age. For the average healthy individual, serum creatinine levels remain relatively constant between the ages of 20 and 70, with a mean of 0.90 mg/dL for men and 0.70 mg/dL for women. Beyond the age of 70, serum creatinine levels gradually start to increase again in both genders, as presented in Figures 2.6 and 2.7.

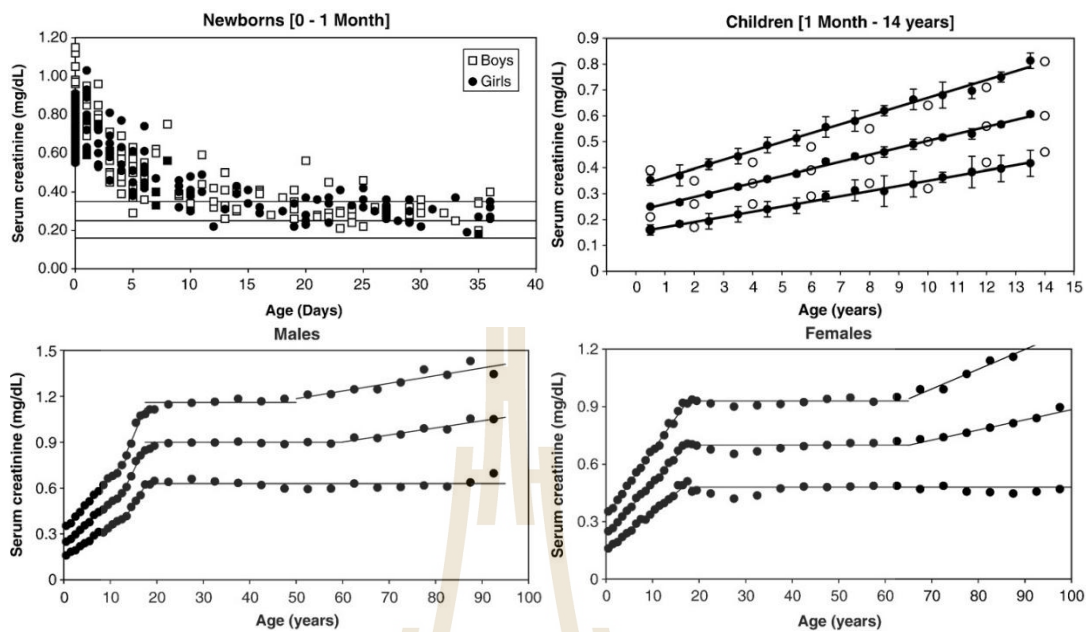


Figure 2.6 An example illustrating the dependency of serum creatinine levels on age and gender. (Pottel, Vrydags, Mahieu, Vandewynckele, Croes, and Martens, 2008)

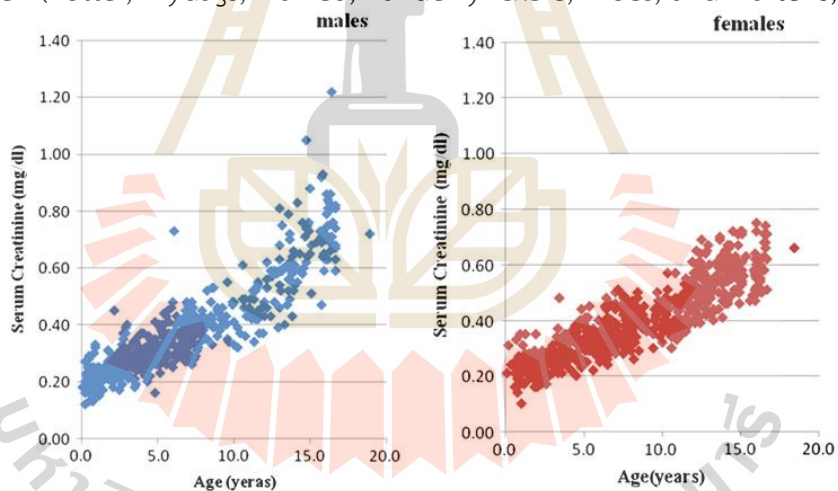
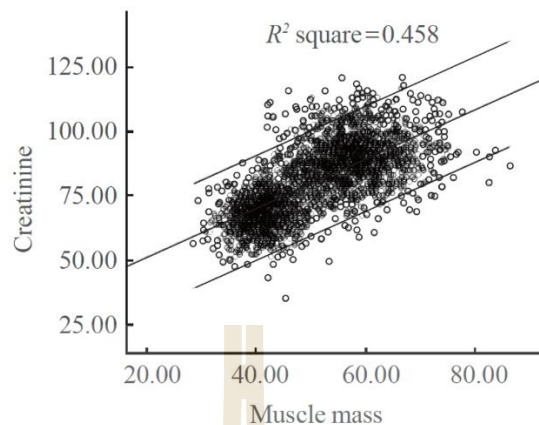


Figure 2.7 Illustration depicting the relationship between serum creatinine levels and age/gender dependency. (Uemura et al., 2011)

Furthermore, serum creatinine levels depend significantly on muscle mass. This relationship underscores the importance of considering muscle mass as a crucial factor when interpreting serum creatinine levels in clinical assessments. Understanding this association aids in more accurate evaluations of renal function and overall health status. Drawing upon the literature reviewed, the ensuing results are outlined in figure 2.8 below.



**Figure 2.8** An example depicting the relationship between serum creatinine levels and muscle mass. (Moon, Lee, and Yoon, 2013)

Creatinine levels are critical for evaluating kidney function. Thus, it is essential to establish reliable methods for sample collection to accurately analyze and diagnose kidney diseases.

The above study focuses on the level of creatinine in the blood, which is an invasive method of analysis. This invasiveness is partly due to the lack of simple testing methods for creatinine and the difficulty of blood collection. As an alternative, less invasive bodily fluids such as urine can provide real-time information about molecular biomarkers in the body. Urine testing offers several advantages over blood analysis, including ease of collection, storage, and shipment of specimens, as well as the ability to collect multiple samples. The normal concentrations creatinine in urine range between 3.3 to 27 mM (Not separated by gender). (Gonzalez-Gallardo, Arjona, Álvarez-Contreras, and Guerra-Balcázar, 2022) There are two main types of urine creatinine tests: the random (spot) urine test and the 24-hour creatinine test. The random urine test involves collecting a urine sample at any time of the day and bringing it to the lab for analysis.

In contrast, the 24-hour creatinine test requires collecting all urine produced over a full 24-hour period in a special container before submitting it for laboratory analysis. (Price, Newall, and Boyd, 2005)

Instructions for collecting a 24-hour urine sample may vary by laboratory. Generally, the first morning urine is discarded. All urine produced over the next 24 hours, including the following morning's first specimen, is collected in laboratory-provided containers. A preservative solution is added to stabilize the sample. After 24 hours, the total volume is recorded, and a representative sample is submitted for analysis. (Corder, Rathi, Sharif, and Leslie, 2018) and significant decreases in urine

creatinine levels were observed only after prolonged storage at high temperatures (30 days at 558 °C). When stored for 2 days at 558 °C, the decrease in urine creatinine levels was less than 3%. Therefore, we conclude that, except under extreme conditions, such as prolonged storage at high temperatures, urine creatinine levels remain largely unaffected by storage time and temperature. (Spierto, Hannon, Gunter, and Smith, 1997) However, collecting samples for 24 hours can be difficult and inconvenient for some patients. Therefore, a study was conducted to confirm the feasibility of estimating creatinine clearance values over a 2-hour period rather than over a 24-hour period. It was determined that there was no statistically significant difference in creatinine clearance values between urine samples collected at 2 hours and those collected at 24 hours. Therefore, it is possible to collect a urine sample for only 2 hours to check for creatinine levels. (DeVanand and Chithrapavai, 2013)

In addition to creatinine, there are several other biomarkers that play pivotal roles in the assessment and management of kidney disease. These biomarkers include Blood Urea Nitrogen (BUN), estimated Glomerular filtration rate (eGFR), Fasting Blood Sugar (FBG), Lipid profile and Urine Microalbumin (UMA)

There is also, patients who have the following medical background are identified as being at a heightened risk for chronic kidney disease (CKD). CKD is associated with various risk factors and comorbidities, including the use of nonsteroidal anti-inflammatory drug (NSAIDs), as well as conditions such as myocardial infarction (MI), congestive heart failure (CHF), stroke, diabetes mellitus (DM), cancer, systemic lupus erythematosus (SLE), osteoarthritis, rheumatoid arthritis (RA), gout, kidney and ureter calculi, and hypertension. (Hsu et al., 2015)

Moreover, certain medications can lead to inaccurately elevated plasma creatinine levels due to their interference with the analytical methods used to measure creatinine. The use of cimetidine to aid creatinine clearance offers a promising approach that is both convenient and cost-effective for accurately measuring glomerular filtration rate (GFR). It has the potential to replace traditional GFR measurement methods, which are more costly and less practical for long-term renal function studies. Additionally, plotting reciprocal values of serum creatinine against time while using cimetidine could enhance the reliability of monitoring renal deterioration. Cimetidine may also increase the sensitivity of serum creatinine in detecting subtle changes in renal function by reversing the blunted inverse relationship between serum creatinine and GFR caused by increased tubular secretion and reduced GFR. (Choi et al., 1993)

It has been observed that individuals with normal renal function may experience a reversible increase in serum creatinine while undergoing treatment with trimethoprim. These findings suggest that trimethoprim inhibits the tubular secretion of creatinine. The magnitude of the increase in serum creatinine could be substantial enough to mimic conditions such as dehydration or renal function deterioration. Therefore, any changes in serum creatinine levels during trimethoprim therapy should be carefully assessed and interpreted. (Kastrup, Petersen, Bartram, and Hansen, 1985)

Pyrimethamine, both alone and in combination with dapsone, has been reported to increase plasma creatinine levels by approximately 20% in healthy volunteers and by 27% in HIV-infected patients. (Opravil, Keusch, and Lüthy, 1993) In some conditions, such as salt depletion, advanced age, liver cirrhosis, renal diseases, and renal failure, salicylates can induce a rise in plasma creatinine concentration. This occurs due to decreased renal plasma flow and glomerular filtration rate (GFR). It is proposed that salicylates could either disrupt the binding of creatinine to serum proteins or competitively inhibit the tubular secretion of creatinine. Although these results have not been confirmed by all studies, they are frequently cited as an example of anionic substances capable of inhibiting creatinine tubular secretion. (Andreev, Koopman, and Arisz, 1999)

Other drugs, such as phenacemide, corticosteroids, and vitamin D derivatives, can affect plasma creatinine levels. Specifically, an increase in plasma creatinine has been shown to be caused by the anticonvulsant drug phenacemide, and this increase is completely reversible upon discontinuation of the drug. Similarly, treatment with calcitriol or alfacalcidol can also lead to a rise in plasma creatinine and/or a decrease in creatinine clearance. Since neither free nor ionized calcium levels were measured, the possibility of hypercalcemia as a contributing cause cannot be completely excluded. However, in two studies, the glomerular filtration rate (GFR), measured through inulin clearance, appeared to remain unchanged. The mechanisms by which vitamin D elevates plasma creatinine concentrations are unclear, but they may involve decreased tubular secretion and/or increased creatinine production. (Andreev, Koopman, and Arisz, 1999)

## 2.2.2 Gold standard methods for measuring creatinine

### 2.2.2.1 Alinity c Creatinine (Enzymatic) Reagent Kit

Alinity c Creatinine (Enzymatic) Reagent Kit is used for the quantitative determination of creatinine in human serum, plasma, and urine on the Alinity c analyzer.

**Explanation of the test:** Creatinine is eliminated from blood by glomerular filtration. Reduced renal function results in an increased serum creatinine concentration. Measurement of serum creatinine is used to diagnose and monitor acute and chronic renal disease, estimate glomerular filtration rate (GFR), or assess the status of renal dialysis patients. Urine creatinine analysis is used to calculate creatinine clearance, confirm completeness of 24-hour collections, or serve as a reference quantity for other analytes, such as in calculation of the albumin/ creatinine ratio.

**Principle of the procedure:** Creatinine in the sample is hydrolyzed by creatininase to creatine. Creatine is in turn hydrolyzed by creatinase to sarcosine and urea. Sarcosine from this reaction is oxidized by sarcosine oxidase to glycine and formaldehyde, with the concomitant production of hydrogen peroxide. The hydrogen peroxide reacts with 4-aminoantipyrine and ESPMT\* in the presence of peroxidase to yield a quinoneimine dye. The resulting change in absorbance at 548 nm is proportional to the creatinine concentration in the sample. This enzymatic method is sensitive and specific for creatinine and is not affected by endogenous substances, such as ketoacids, cephalosporins, and bilirubin that interfere with the Jaffe method.

\* ESPMT = N-ethyl-N-sulfopropyl-m-toluidine

### Specimen collection and preparation for analysis, as shown in table 2.3

#### Specimen types

The specimen types listed below were verified for use with this assay. Other specimen types, collection tube types, and anticoagulants have not been verified with this assay

**Table 2.3** Specimen collection and preparation for analysis.

Specimen Types	Collection Vessel	Special Conditions
Serum	Serum tubes (with or without gel barrier)	Glass tubes were not tested.
Plasma	Collection tubes Acceptable anticoagulants are:	EDTA is not recommended.
Plasma (Continued)	Lithium heparin (with or without gel barrier) Sodium heparin	An internal study showed decreased results. Glass tubes were not tested.
Urine (random specimens of timed specimens collected over intervals shorter than 24 hours)	Clean plastic or glass container without preservatives	
Urine (24 hour)	Clean plastic or glass container with preservatives	The preferred preservatives are boric acid and hydrochloric acid.

**Specimen conditions:**

1. For accurate results, serum and plasma specimens should be free of fibrin, red blood cells, and other particulate matter. Serum specimens from patients receiving anticoagulant or thrombolytic therapy may contain fibrin due to incomplete clot formation.
2. For accurate results, plasma specimens should be free of platelets and other particulate matter. Ensure centrifugation is adequate to remove platelets.
3. Urine specimens must be inspected for particulates. If present, centrifuge the specimen to remove particulates prior to testing.
4. To prevent cross contamination, use of disposable pipettes or pipette tips is recommended.

**Preparation for analysis:**

1. Follow the tube manufacturer's processing instructions for collection tubes. Gravity separation is not sufficient for specimen preparation.
2. Specimens should be free of bubbles. Remove bubbles with an applicator stick before analysis. Use a new applicator stick for each specimen to prevent cross-contamination.
3. To ensure consistency in results, recentrifuged specimens prior to testing if they contain fibrin, red blood cells, or other particulate matter.

NOTE: If fibrin, red blood cells, or other particulate matter are observed, mix by low speed vortex or by inverting 10 times prior to recentrifugation. and Table 2.4 shows specimen storage for analysis.

**Table 2.4** Specimen storage.

Specimen Type	Temperature	Maximum Storage time
Serum/Plasma	20 to 25 °C	7 days
	2 to 8 °C	7 days
	-20 °C	3 months
Urine	20 to 25 °C	2 days
	2 to 8 °C	6 days
	-20 °C	6 months

**Limitation:**

1. Very rarely unreliable results (i.e. pseudohypercreatininemia) secondary to occurrence of monoclonal protein have been described in patients affected by Waldenstrom's macroglobulinemia 13 (only IgM type) or by monoclonal gammopathy of unknown significance 13 (IgG or IgM).
2. N-acetyl-L-cysteine at therapeutically achieved concentrations may lead to falsely low results in serum/plasma samples.
3. Alpha-methyl dopa may cause falsely low results in serum/plasma samples. (Core Laboratory at Abbott, 2018)

**2.2.3 Analytical methods for the detection of creatinine**

Several methods have been developed for creatinine detection such as liquid chromatography, (Hewavitharana and Bruce, 2003) mass spectroscopy, chemiluminescence, (Hanif, John, Gao, Saqib, Qi, and Xu, 2016) enzymatic assays, (Piéroni et al., 2011) and microfluidics (Lin et al., 2013) However, the applicability of

these methods in point-of-care testing and onsite monitoring is limited by issues such as laborious sample preparation, time-consuming analysis, costly reagents, and the need for sophisticated instrumentation. Table 2.5 summarizes methods for the measurement of creatinine.

**Table 2.5** Analytical methodologies reported for the detection of creatinine.

Methods	Detection limit	Ref.
LC-UV with 0.045 M ammonium sulfate mobile phase (C 18 column)	0.17±0.06 $\mu\text{g mL}^{-1}$ (~1.5 $\mu\text{M}$ )	(Dash and Sawhney, 2002)
Advantage: high peak capacity small molecule analyte		
Disadvantage: band-broadening		
HPLC with sample de-proteination	0.156 $\mu\text{g mL}^{-1}$ (~1.38 $\mu\text{M}$ )	(Jen, Hsiao, and Liu, 2002)
Advantage: simultaneous detection of creatinine and uric acid		
Disadvantage: the sample requires pretreatment		
Low-capacity cation-exchange chromatography	0.02 $\mu\text{M}$	(Yokoyama, Tsuji, and Sato, 2005)
Advantage: can detect multiple analytes in urine		
Disadvantage: column efficiency is less		
Surface-enhanced Raman spectroscopy upon silver colloidal suspensions	10 $\text{mg L}^{-1}$ (~88 $\mu\text{M}$ )	(Y. Wang et al., 2012)
Advantage: improved sensitivity and selectivity		
Disadvantage: requires coupling with nanoparticles		
High performance capillary electrophoresis	0.04 $\text{mg dL}^{-1}$ (~0.35 $\mu\text{M}$ )	(Shi, Ma, and Ma, 1995)
Advantage: high separation efficiency, low sample and electrolyte		
Disadvantage: lower sensitivity and lower repeatability		

This work focuses on developing a low-cost electrochemical method for creatinine detection that reduces both the time and complexity involved. As illustrated in Table 2.6, which offers a detailed analysis of current electrochemical sensors

developed for the measurement of creatinine levels, it becomes clear that these devices exhibit notable variations in sensitivity, linear range, and limit of detection.

**Table 2.6** Electrochemical sensors for creatinine detection.

Electrode	method	Sensitivity	Linear range	Limit of detection	Ref.
Cu/GC Cu/SPE	DPV DPV	$7.7 \pm 0.45$ $\mu\text{A mM}^{-1}$	0.083–20.0 mM 0.28–3.0 and 3.0–20.0 mM	0.025 mM 0.084 mM	(Jankhunthod, Kaewket, Termsombut, Khamdang, and Ngamchuea, 2023a)
PAA gel- Cu(II)/Cu <sub>2</sub> O NPs/SPCE	CV/DPV	12.96 $\mu\text{A}/\ln\text{M}$	0.20–100 mM	6.5 $\mu\text{M}$	(Kalasin, Sangnuang, Khownarumit, Tang, and Surareungchai, 2020)
Fe <sub>2</sub> O <sub>3</sub> /PANI- 1/GCE	DPV	153 $\mu\text{A}$ $\mu\text{M}^{-1}$	0.1 $\mu\text{M}$ –13 mM	0.144 $\mu\text{M}$	(Sriramprabha, Sekar, Revathi, Viswanathan, and Wilson, 2020)
MXene/Cu ions/SPCE	SWV	–	10–400 $\mu\text{M}$	1.2 $\mu\text{M}$	(J. Liu et al., 2019)

Table 2.6 Electrochemical sensors for creatinine detection (Continued).

Electrode	method	Sensitivity	Linear range	Limit of detection	Ref.
Pt macrodisc	CV	$347 \pm 13$ $A m^{-2}M^{-1}$	1.00–10.00 mM	0.10 mM	(Kaewket and
Pt microdisc	LSV	$2097 \pm 80$ $A m^{-2}M^{-1}$	0.00–5.00 mM	0.670 mM	Ngamchuea,
Pt-MEA	LSV	$5401 \pm 99$ $A m^{-2}M^{-1}$	0.00–5.00 mM	0.059 mM	2023)
Cu/GC	CV	$6.09 \pm 0.13$ $\mu A mM^{-1}$	0–10 mM	0.035 mM	(Ngamchuea, Wannapaiboon, Nongkhunsan, Hirunsit, and Fongkaew, 2022)
MIP/Ni@PANI NPs/MCGE	DPV	$150.18 \mu A$ $\mu M^{-1}$	0.004–0.8 $\mu M$	0.0002 $\mu M$	(Rao et al., 2017)
Pectin– MWCNT/ CPE	DPV	$0.1168 \pm$ $0.0128$ $\mu A \mu M^{-1}$	0.016–3.3 $\mu M$	0.6241 $\mu M$	(Yazhini, Suja, Bagyalaksmi, and Pavalamalar, 2018)
Cu/SPE	CV	–	6–378 $\mu M$	0.0746 $\mu M$	(Raveendran, Resmi, Ramachandran, Nair, and Babu, 2017)

**Table 2.6** Electrochemical sensors for creatinine detection (Continued).

Electrode	method	Sensitivity	Linear range	Limit of detection	Ref.
CuO@MIP/CPE	AMP	0.211 $\mu\text{A } \mu\text{M}^{-1}$	0.5– 200 $\mu\text{M}$	0.083 $\mu\text{M}$	(Nontawong et al., 2019)
$\text{Fe}^{3+}$ /CB NPs/SPCE	DPV	18.28 $\mu\text{A } \text{mM}^{-1}$	100– 6500 $\mu\text{M}$	43 $\mu\text{M}$	(Fava et al., 2020)
Array of 16 gold electrodes	AMP	19.17 nA (mg/dL) <sup>-1</sup>	0– 11.33 mg/dL	0.46mgdL <sup>-1</sup> (~4 $\mu\text{M}$ )	(Wei et al., 2012)
$\text{Fe}_2\text{O}_3$ @Polyaniline NPs	DPV		20 nM– 1.0 $\mu\text{M}$	0.35 nM	(Wen et al., 2014)

(CV: Cyclic voltammetry, DPV: Differential pulse voltammetry, LSV: Linear sweep voltammetry, AMP: Amperometry, SWV: square wave voltammetry)

## 2.2.4 Cu(II)-ImaSMe complex

### 2.2.4.1 Electronic configuration of Cu(II)

A copper (Cu) atom, which has 29 electrons, achieves extra stability by having a fully-filled 3d subshell and a half-filled 4s subshell. To attain this stable configuration, one electron from the 4s<sup>2</sup> subshell jumps to the 3d<sup>9</sup> subshell, resulting in the electron configuration: 1s<sup>2</sup> 2s<sup>2</sup> 2p<sup>6</sup> 3s<sup>2</sup> 3p<sup>6</sup> 3d<sup>10</sup> 4s<sup>1</sup>. The Cu<sup>2+</sup> ion is attained by the removal of two electrons, one from the 4s<sup>1</sup> subshell and one from the 3d<sup>10</sup> subshell, resulting in the electron configuration 1s<sup>2</sup> 2s<sup>2</sup> 2p<sup>6</sup> 3s<sup>2</sup> 3p<sup>6</sup> 3d<sup>9</sup>. When subjected to reductive potentials, the Cu(II) center in the Cu(II) complex can be reduced to Cu(I) or Cu(0). When determining the electron configuration for Cu(I), we start with the electron configuration of a neutral copper atom, which is [Ar] 3d<sup>10</sup> 4s<sup>1</sup>. To form Cu(I), we remove one electron from the 4s orbital, leaving us with the following electron configuration: 1s<sup>2</sup> 2s<sup>2</sup> 2p<sup>6</sup> 3s<sup>2</sup> 3p<sup>6</sup> 3d<sup>10</sup>.

### 2.2.4.2 Properties of Cu(II)-ImaSMe complex

The copper(II) ion demonstrates typical behavior characteristic of transition metals in forming coordination complexes. However, it departs from the conventional by displaying reluctance towards assuming regular octahedral or tetrahedral stereochemistry. This departure stems from the absence of cubic symmetry in its  $3d^9$  outer electron configuration, leading to distorted manifestations of the fundamental stereochemistry. While coordination numbers of four, five, and six are prevalent, each structure showcases variations due to bond length or bond-angle distortions. The  $d^9$  configuration simplifies the system theoretically, representing a single positive hole within an otherwise filled  $d^{10}$  configuration. The behavior of this positive hole varies across different stereochemistry. (Hathaway and Billing, 1970)

### 2.2.4.3 Example for Cu(II)-ImaSMe complex with sulfur ligand

A cis-dichloro copper(II) complex with a novel tridentate thiomethyl substituted imidazole based Schiff base ligand L, obtained from 2-methylthioaniline and 2-imidazolecarboxaldehyde, as presented in figure 2.9.

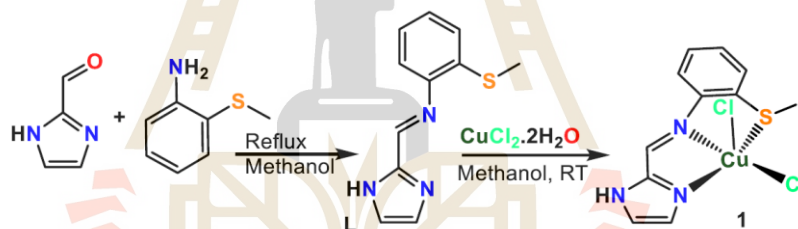


Figure 2.9 Preparation of ligand and its copper complex.

The present complex has two labile chloride ligands, similar to cisplatin, and the presence of imidazole in the backbone prompted us to investigate its anticancer and antibacterial properties. Herein, along with the phenoxazinone synthase (PHS) activity. The PHS is an important naturally occurring pentacopper containing oxidase, found in the bacterium *Streptomyces antibiotus*. They have also reported the antibacterial activity of 1 against *E. coli*, *Staphylococcus aureus* and *K. pneumoniae*, as well as its anticancer activity against the human colorectal adenocarcinoma (HT-29) cancerous cell line. (Bandopadhyay et al., 2022)

### 2.2.5 Copper(II)–creatinine complex formation

Creatinine is classified as an electrochemically inactive species, meaning it does not produce an electrochemical response within the potential window typically used for measurements in aqueous solutions. This characteristic limits the direct electrochemical detection of creatinine, necessitating alternative methods or modifications to detect its presence accurately in electrochemical analyses.

In humans, copper is essential for the synthesis of red blood cells, proteins, and enzymes, as well as for the metabolism of iron, glucose, and cholesterol (Gupta and Lutsenko, 2009), (Uauy, Olivares, and Gonzalez, 1998); moreover, copper plays crucial roles in the chemistry and catalysis of biological systems. (Festa and Thiele, 2011) The diverse functions of copper in biological systems stem from its unique ability to cycle between its reduced ( $\text{Cu}^+$ ) and oxidized ( $\text{Cu}^{2+}$ ) forms. This redox cycling allows copper to participate in various biochemical reactions and interact effectively with nitrogen, oxygen, and sulfur donor functional groups commonly found in biomolecules. (Selden, Schilling, Godfrey, and Yee, 2024)

In their study, (Ngamchuea, Wannapaiboon, Nongkhunsan, Hirunsit, and Fongkaew, 2022) they developed a method to detect creatinine in aqueous solutions through the formation and electrochemical detection of a copper(II)–creatinine complex. The approach involves the creation of a stable complex between copper ions and creatinine, which can be monitored through electrochemical techniques.

## 2.3 Detection and characterization methods

### 2.3.1 Cyclic voltammetry

Cyclic voltammetry (CV) is a highly effective electrochemical technique widely used to study the reduction and oxidation processes of molecular species. CV is also invaluable for studying electron transfer-initiated chemical reactions. CV is performed by cycling the potential of a working electrode against a reference electrode, which maintains a constant potential, and measuring the resulting current. The potential is changed linearly with time and reversed at a certain point (Figure 2.10a). The cyclic voltammograms were obtained from the measurement of the current of the working electrode during the potential scan. (Figure 2.10b) An electrochemical cell setup is commonly used in various electrochemical experiments, as shown in Figure 2.10c.

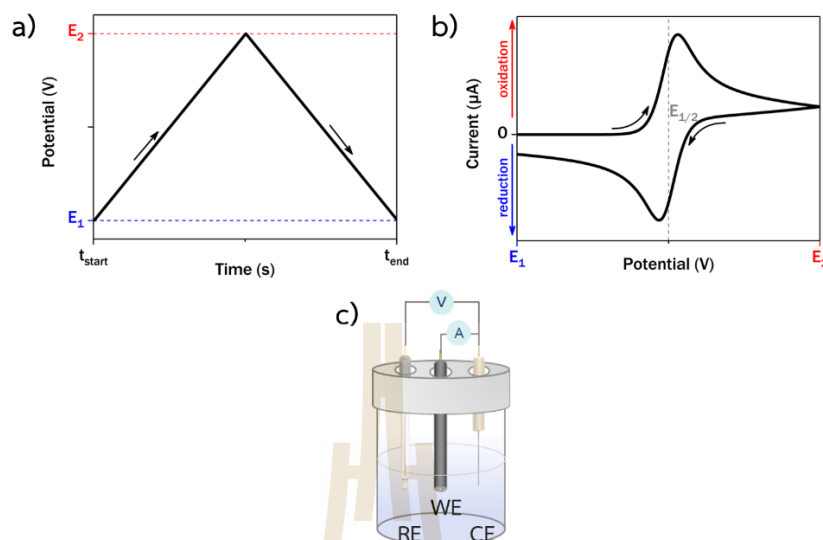


**Figure 2.10** a) A plot of the applied potential with time in CV. b) Cyclic voltammogram. c) Setup of three-electrode in electrochemical.

### 2.3.2 Electrochemical impedance spectroscopy (EIS)

Electrochemical Impedance Spectroscopy (EIS) is an electrochemical technique to measure the impedance of a system in dependence of the AC potentials frequency. That can be used in a broad range of applications, such as microbiological analysis, food products screening, corrosion monitoring, quality control of coatings and cement paste, characterization of solid electrolytes and human body analysis. (Grossi and Riccò, 2017)

In a conventional electrochemical cell, matter–(redox species)–electrode interactions include the concentration of electroactive species, charge-transfer, and mass-transfer from the bulk solution to the electrode surface in addition to the resistance of the electrolyte. Each of these features is characterized by an electrical circuit that consists of resistances, capacitors, or constant phase elements that are connected in parallel or in a series to form an equivalent circuit, as shown in Figure 11. Thus, the EIS could be used to explore mass-transfer, charge-transfer, and diffusion processes. Accordingly, the EIS has the ability to study intrinsic material properties or specific processes that could influence conductance, resistance, or capacitance of an electrochemical system. A basic approach for describing the EIS circuit and the redox reaction occurs at the surface of working electrodes in a conventional electrochemical cell, as illustrated in the Figure 2.11.

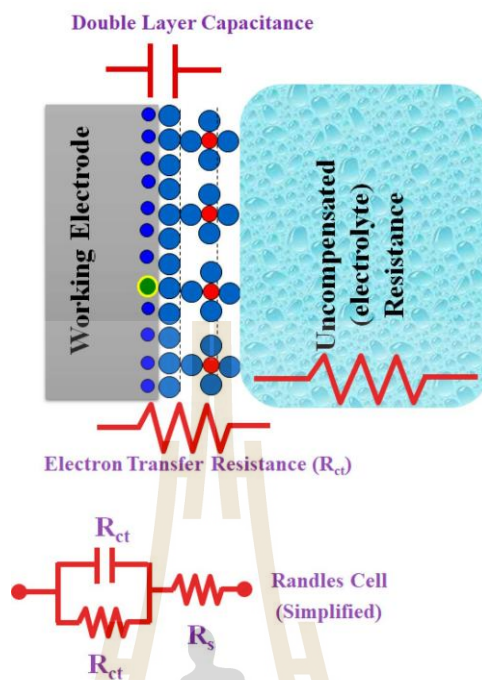


**Figure 2.11** A simple scheme to describe the EIS circuit and the redox reaction takes place at the surface of working electrodes in a conventional-electrochemical cell. (Magar, Hassan, and Mulchandani, 2021)

### 2.3.3 Scanning electron microscope (SEM)

The scanning electron microscope (SEM) is an electron microscope that employs a focused beam of high-energy electrons to investigate materials, as opposed to a light beam, due to the smaller wavelength of the electron beam. Consequently, SEM offers superior magnification capabilities. It operates by scanning a focused electron beam across the surface of materials to generate an image. The interaction between the electrons in the beam and the materials produces various signals, yielding valuable descriptive information about the surface morphology of the materials. Schematic diagram of the core components of an SEM microscope as presented in Figure 2.12.

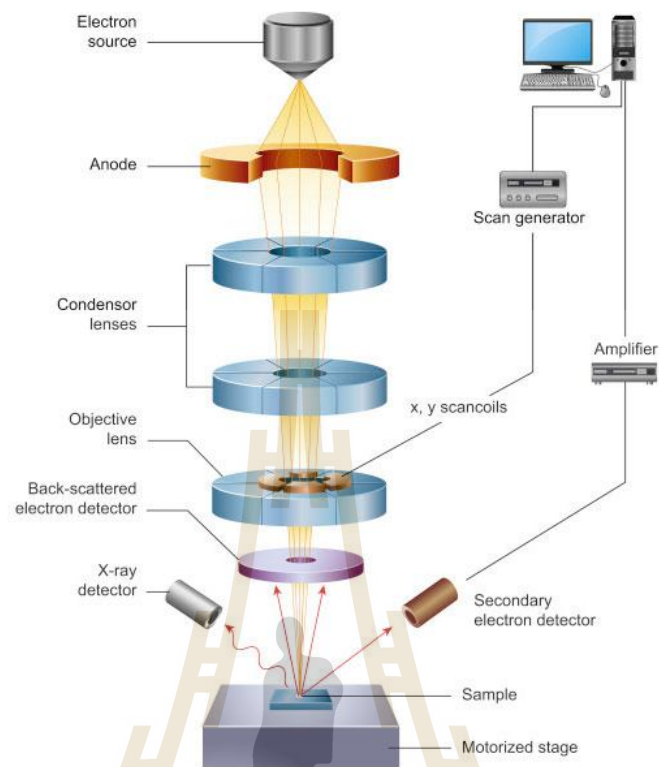


**Figure 2.12** Schematic diagram of the core components of an SEM microscope. (Inkson, 2016)

### 2.3.4 X-ray diffraction spectroscopy (XRD)

X-ray diffraction spectroscopy is a generic term for phenomena associated with changes in the direction of X-ray beams due to interactions with the electrons around atoms. This occurs through elastic scattering, where the energy of the waves remains unchanged. The resulting map, showing the directions of X-rays far from the sample, is called a diffraction pattern. This is distinct from X-ray crystallography, which uses X-ray diffraction to determine atomic arrangements in materials and includes methods to translate experimental diffraction data into atomic positions. Schematic of the experimental principle for X-ray diffraction as shown in Figure 2.13.

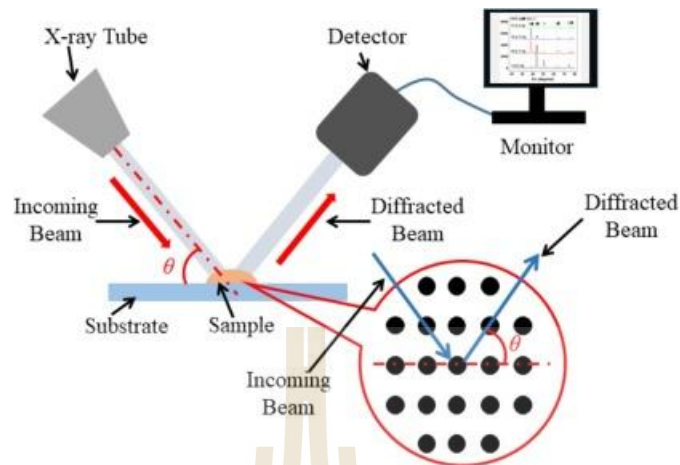


**Figure 2.13** Schematic of the experimental principle for X-ray diffraction. (Zhao, Wang, Zhong, Akhtaruzzaman, Liang, and Chen, 2023)

### 2.3.5 X-ray adsorption spectroscopy (XAS)

X-ray absorption spectroscopy is used to measure and study the absorption intensity of incident X-rays in matter, such as atoms, molecules, and condensed systems, as a function of their energy or wavelength. The incident X-ray is absorbed when its energy exceeds the excitation energy of deep-core electrons of a specific element in the sample, causing an edge-like absorption spectrum. The X-ray absorption near-edge structure (XANES), within tens of eV of the edge, provides information on the symmetry-projected conduction band density of states (DOS), which relates to electronic properties such as oxidation state, crystal-field splitting, and magnetic spin pairing. The extended X-ray absorption fine structure (EXAFS), extending to several hundreds of eV above the edge, provides local structural information, which is particularly valuable for studying amorphous materials or samples in low concentrations where the X-ray diffraction (XRD) method is inapplicable. As the information shown in the Figure 2.14.

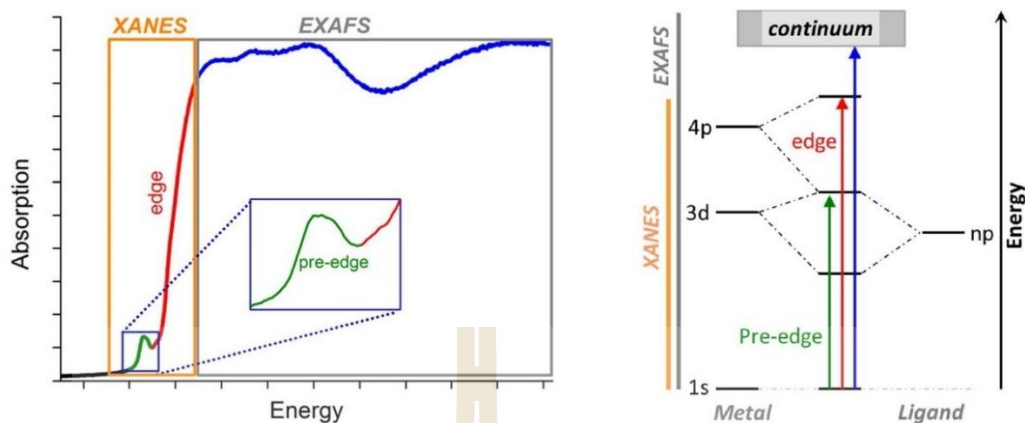


**Figure 2.14** Separation into the XANES and EXAFS range. And on the right the corresponding energy level diagram with the associated transitions. (Zimmermann et al., 2020)

### 2.3.6 CHNS analysis

CHNS elemental analysis, determines the percentage of Carbon (C), Hydrogen (H), Nitrogen (N) and Sulfur (S) present in a sample. The technique is reliable and cost-effective to assess the purity and chemical composition of compounds. CHNS/O configuration as depicted in the Figure 2.15.

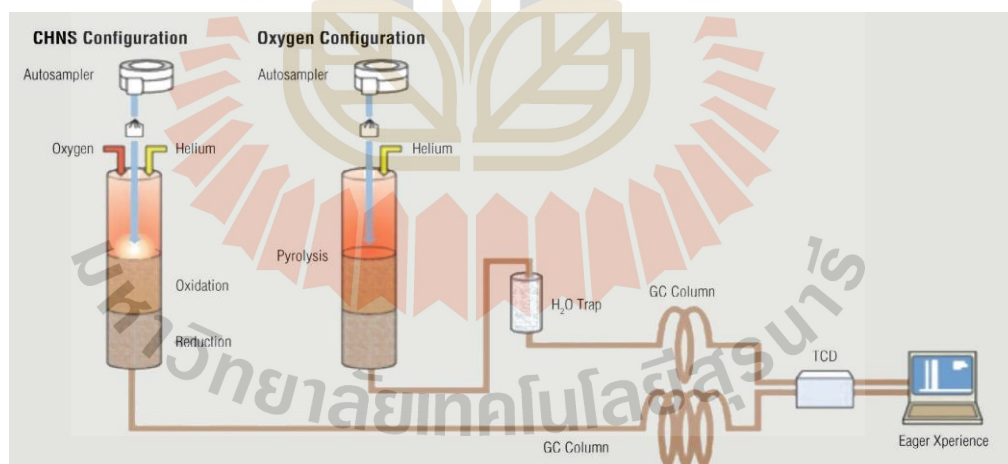


**Figure 2.15** CHNS/O configuration. (Ebere and Ngozi, 2019)

### 2.3.7 Thermogravimetry analysis (TGA)

Thermogravimetric analysis (TGA) is a powerful technique for the measurement of thermal stability of materials including polymers. In this method, changes in the weight of a specimen are measured while its temperature is increased, as indicated by the Figure 2.16.

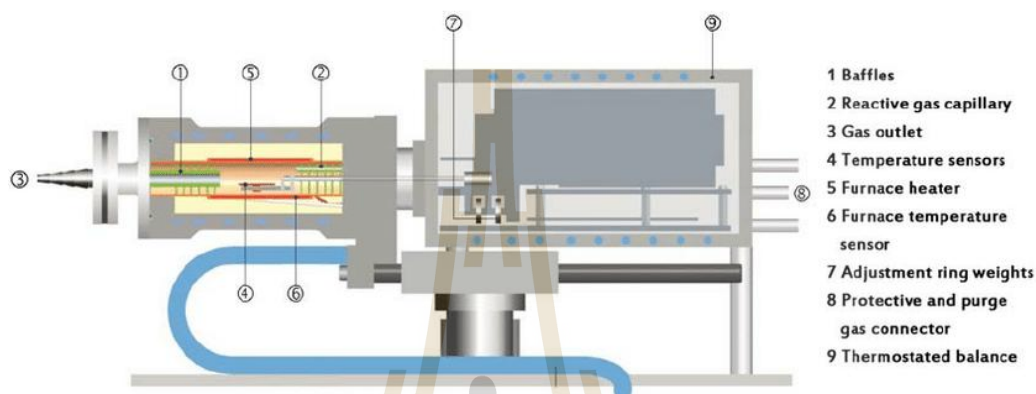


Figure 2.16 Scheme of thermogravimeter. (Ház, Jablonský, Orságová, and Šurina, 2013)

### 2.3.8 Ultraviolet–visible (UV–vis) spectroscopy

Ultraviolet–visible (UV–vis) spectroscopy is a method that examines the interaction of a chemical species with light in the ultraviolet and visible regions of the spectrum. Many molecules and ions absorb energy in these ranges and are known as chromophores. When a photon is absorbed, it excites an electron in the chromophore to higher-energy molecular orbitals, creating an excited state. For organic chromophores, four types of transitions can occur:  $\pi-\pi^*$ ,  $n-\pi^*$ ,  $\sigma-\sigma^*$ , and  $n-\sigma^*$ . Transition metal complexes often exhibit colors due to the multiple electronic states arising from partially filled d orbitals. Schematic diagram of the UV-Visible Spectrophotometer as demonstrated in the Figure 2.17.

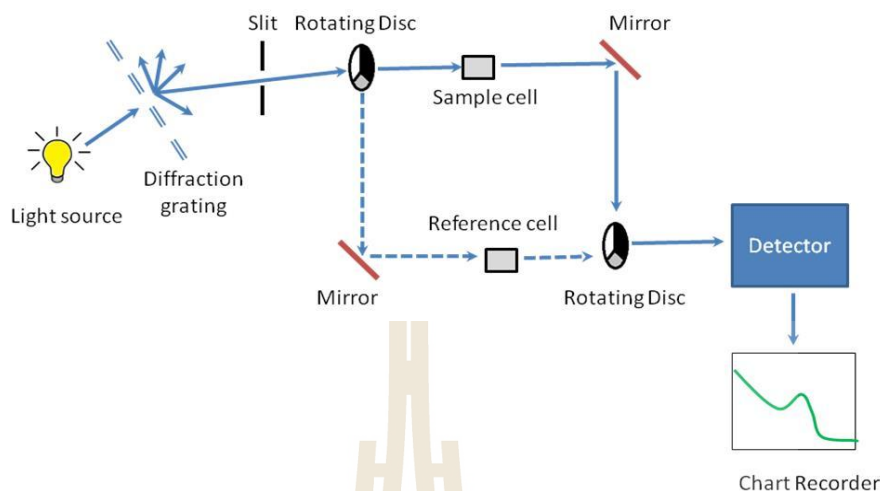


Figure 2.17 Schematic diagram of the UV-Visible Spectrophotometer.

### 2.3.9 Fourier transform infrared (FTIR) spectroscopy

Fourier Transform Infrared (FTIR) spectroscopy is the preferred method of infrared spectroscopy. IR radiation is transmitted through a sample in infrared spectroscopy. The sample absorbs some of the infrared energy, and some of it is transferred (passed through). The resulting spectrum gives the sample a molecular fingerprint by displaying the molecule's absorption and transmission. Principle and instrumentaion of Fourier transform infrared (FTIR) spectroscopy are illustrated in Figure 2.18.

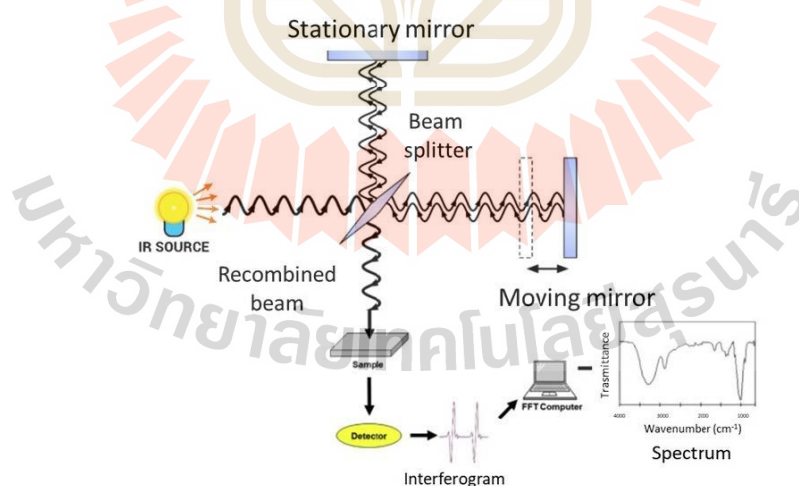
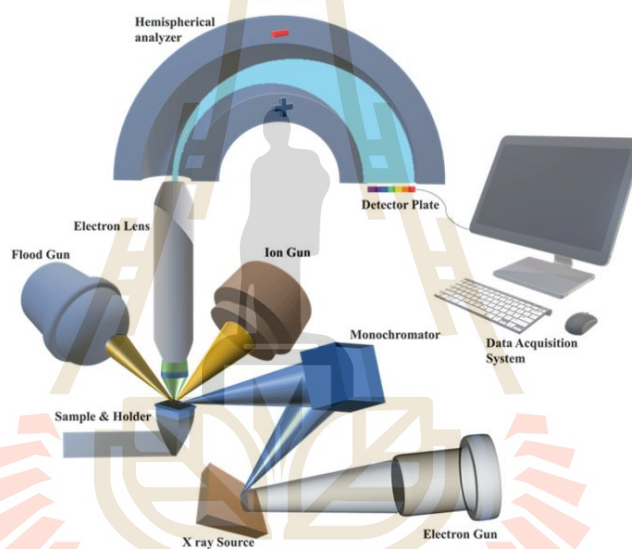


Figure 2.18 Principle and instrumental of Fourier transform infrared (FTIR) spectroscopy. (Famarzi, Moggio, Diano, Portaccio, and Lepore, 2023)

### 2.3.10 X-ray photoelectron spectroscopy (XPS)

X-ray photoelectron spectroscopy (XPS) is a commonly employed technique for determining the elemental composition and chemical state of materials. It measures the kinetic energy of emitted photoelectrons, from which the electron binding energy is derived based on the wavelength of the photoelectrons and the energy of the incident X-rays. By plotting the photoelectron intensity against binding energy, it is possible to identify the elements present in the material and assess the oxidation states of each element. Furthermore, variations in binding energy for the same atom in the same oxidation state can reveal differences in the local coordination environment. As the information shown in the Figure 2.19.



**Figure 2.19** Schematic diagram of the instrumental operation of the X-ray photoelectron spectroscopy (XPS). (A. Khan, Fayyaz, Shakoor, and Mansoor, 2022)

## CHAPTER III

### MATERIALS AND METHODS

#### 3.1 Guanosine detection

##### 3.1.1 Chemical reagents

All chemical reagents were of analytical grades and used as received without further purification: potassium hexacyanoferrate(II) trihydrate ( $K_4[Fe(CN)_6] \cdot 3H_2O$ ,  $\geq 98.5\%$ , Sigma-Aldrich), guanosine ( $C_{10}H_{13}N_5O_5$ ,  $\geq 98.0\%$ , TCI Chemical), potassium chloride (KCl, 99.5-100.5 %, Fluka), urea ( $CH_4N_2O$ ,  $\geq 98\%$ , Sigma-Aldrich), hydrochloric acid (HCl, 37% V/V, RCI Labscan), citric acid anhydrous ( $C_6H_8O_7$ , 99.5%, QRëC), sodium citrate tribasic dihydrate ( $C_6H_5Na_3O_7 \cdot 2H_2O$ ,  $\geq 99\%$ , Sigma-Aldrich), sodium phosphate monobasic ( $NaH_2PO_4 \cdot 2H_2O$ , 99%, QRëC), di-sodium hydrogen phosphate anhydrous ( $Na_2HPO_4$ , 99%, QRëC), sodium hydrogen carbonate ( $NaHCO_3$ , 99.7%, QRëC), and sodium hydroxide (NaOH, 100%, Sigma-Aldrich). Deionized water (DI) which was used for all experiments was obtained from the Elga Purelab Ultra water purification system (18.2 M $\Omega$ ·cm Elga Labwater, UK). Buffer solutions were freshly prepared to achieve specific pH levels as follows: 0.10 M hydrochloric acid (HCl) for pH 1.0, a mixture of 0.10 M citric acid and 0.10 M sodium citrate for pH 4.0, 0.10 M sodium phosphate monobasic ( $NaH_2PO_4$ ) and 0.10 M sodium phosphate dibasic ( $Na_2HPO_4$ ) for pH 6.0, 0.10 M sodium carbonate ( $Na_2CO_3$ ) and 0.10 M sodium bicarbonate ( $NaHCO_3$ ) for pH 9.0, 0.10 M sodium bicarbonate ( $NaHCO_3$ ) and 0.10 M sodium hydroxide (NaOH) for pH 10.0, and different concentrations of sodium hydroxide (NaOH) for pH 12.0, 13.0, and 14.0. All buffer solutions contain 0.10 M potassium chloride (KCl) as a supporting electrolyte. The pH of the buffer solutions was measured at 25 °C using a digital pH meter (F20 Five Easy with LE409 pH glass electrode, Mettler Toledo, calibrated at pH 4.01, 7.00, and 10.01) and adjusted to the required levels by adjusting the volume ratios of the buffer components.

### 3.1.2 Electrochemical measurements

All electrochemical experiments were performed using a standard three electrode setup in a Faraday cage thermostated at the temperature of 25 °C. A stationary glassy carbon macrodisk electrode (GCE, 3.0 mm diameter, ItaSens, Netherlands), a rotating glassy carbon macrodisk electrode (RDE, 3.0 mm diameter, ALS, Japan), or a stationary carbon fiber microdisk electrode (CFE, 7.0 μm diameter, ALS, Japan) was employed as a working electrode. A silver/silver chloride (Ag/AgCl in 3.4 M KCl, ItaSens) and a platinum wire were used as reference and counter electrodes respectively. The working electrodes were polished on water-alumina slurry (1.00 μm, 0.3 μm and 0.05 μm, Buehler, USA) dispersed on soft lapping pads (Buehler, USA) prior to use. Measurements at a rotating electrode were performed with the RRDE-3A Rotating Ring Disk Electrode Apparatus Ver.3.0 (ALS, Japan), while experiments with the stationary electrode were conducted with an Autolab PGSTAT302N potentiostat (Metrohm, Netherlands).

To eliminate potential oxygen-related interference, all solutions were deoxygenated by purging with a nitrogen gas (99.995% purity) flow for 5 minutes prior to electrochemical measurements. (S.-W. Sun, Liu, Zhou, Wang, and Xia, 2017; Wallace, 1985) Electrochemical measurements were then performed immediately after the electrodes were immersed into the deoxygenated solutions.

### 3.1.3 Computational detail

To study the reaction mechanisms of guanosine conversion, we utilized the density functional theory (DFT) (Kohn and Sham, 1965) method as implemented in the TURBOMOLE version 7.5 program to obtain equilibrium structures and total energies of all considered intermediates. (Ahlich, Bär, Häser, Horn, and Kölmel, 1989) The B3LYP method with a combination of Becke's 3-parameter hybrid exchange functional and the dynamic correlation functional was employed. (Hertwig and Koch, 1997) The triple-zeta basis set with polarization function (def2-TZVP) was used. (Kossmann and Neese, 2009; Weigend and Ahlich, 2005) The convergence of electronic energy was set to  $1.0 \times 10^{-7}$  Hartree and the standard grid (m3) for numerical quadrature was used.

Solvation effects ( $\epsilon = 78.40$ ) (Tajkhorshid and Suhai, 1999) toward the optimized structures and their total energies were included using the conductor-like screening model (COSMO). (Klamt and Schüürmann, 1993; Voityuk and Vyboishchikov, 2019) The energy of H<sup>+</sup> addition and abstraction processes were calculated as  $E_p - (E_R + E_{H^+})$  and  $(E_p + E_{H^+}) - E_R$ , where  $E_p$  and  $E_R$  are the total energies of

product and reactant, respectively. The energy of  $H^+$  ( $E_{H^+}$ ) was calculated as half of the total energy of an isolated  $H_2$  molecule. The potential energy profile of all reaction pathways was constructed based on the reaction energies of elementary steps.

## 3.2 Creatinine detection

### 3.2.1 Chemical reagents

All chemical reagents were of analytical grades and used as received without further purification: 4-(methylthio)aniline ( $C_7H_9NS$ , >98.0%, TCI Chemicals), copper(II) chloride dihydrate ( $CuCl_2 \cdot 2H_2O$ , 99%, APS Finechem), 4-imidazolecarboxaldehyde ( $C_4H_4N_2O$ , 98%, Sigma-Aldrich), ethanol ( $C_2H_5OH$ ,  $\geq 99.9\%$ , Merck KGaA), methanol ( $CH_3OH$ , 99.7%, RCI Labscan), diethyl ether ( $(C_2H_5)_2O$ ,  $\geq 99.9\%$ , PanReac AppliChem), creatinine (2-amino-1-methyl-2-imidazolin-4-one,  $\geq 98.0\%$ , Sigma-Aldrich), tetrabutylammonium hexafluorophosphate (TBAPF<sub>6</sub>,  $\geq 99.0\%$ , Sigma-Aldrich), L-ascorbic acid ( $C_6H_8O_6$ ,  $\geq 99.0\%$ , Sigma-Aldrich), uric acid ( $C_5H_4N_4O_3$ ,  $\geq 99.0\%$ , Sigma-Aldrich), dopamine hydrochloride ( $(HO)_2C_6H_3CH_2CH_2NH_2 \cdot HCl$ ,  $\geq 97.5.0\%$ , Sigma-Aldrich), urea ( $CH_4N_2O$ ,  $\geq 98\%$ , Sigma-Aldrich), sodium L-lactate ( $C_3H_5NaO_3$ ,  $\geq 99.0\%$ , Sigma-Aldrich), L-arginine ( $C_6H_{14}N_4O_2$ , >98%, Acros Organics), creatine monohydrate ( $C_4H_9N_3O_2 \cdot H_2O$ ,  $\geq 98\%$ , HiMedia) and potassium chloride (KCl, 99.5-100.5 %, Fluka). Deionized water which was used for all experiments was obtained from the Elga Purelab Ultra water purification system (18.2 M $\Omega$ ·cm, Elga LabWater, UK).

### 3.2.2 Synthesis of Cu(II)-ImaSMe

To initiate the synthesis, 192.8 mg of 4-imidazolecarbaldehyde ( $C_4H_4N_2O$ ) was placed in a mortar, to which 244.2 mg of 4-(methylthio)aniline ( $C_7H_9NS$ ) was added. The mixture was grounded for 5 minutes until a homogeneous pinkish-brown solid was obtained, indicating the formation of the ligand, designated as ImaSMe. Subsequently, 89 mg of ImaSMe was dispersed in 1.00 mL of ethanol. Concurrently, 36.0 mg of copper(II) chloride dihydrate ( $CuCl_2 \cdot 2H_2O$ ) was dissolved in 1.00 mL of ethanol. The copper(II) chloride solution was then added dropwise to the ImaSMe ligand solution under stirring, with an additional 1.00 mL of ethanol used to rinse the container. The reaction mixture was allowed to stir for 16 hours. Following this, the suspension was filtered through filter paper (cellulose Whatman No.1, 11  $\mu m$  pore size). The resulting solid was rinsed sequentially with cold methanol and cold diethyl ether. The final product was then air-dried.

### 3.2.3 Characterization of Cu(II)-ImaSMe

The morphology and size distribution of the Cu(II)-ImaSMe complex were analyzed using a field emission scanning electron microscope (FE-SEM, 3.00 kV, Zeiss AURIGA, Germany). Powder X-ray diffraction (PXRD) analysis was performed in Debye–Scherrer geometry using Kapton capillaries at Beamline 1.1 W: Multiple X-ray Techniques, Synchrotron Light Research Institute (SLRI, Thailand).

X-ray absorption spectroscopy (XAS), including both X-ray absorption near edge structure (XANES) and extended X-ray absorption fine structure (EXAFS), focused on the Cu K-edge, was conducted at Beamline 1.1 W: Multiple X-ray Techniques at SLRI (Thailand) in transmission mode at ambient temperature and pressure. The measurements were performed simultaneously with a Cu foil as a reference standard for in-line energy calibration during synchrotron operation. The resulting data were processed and analyzed using ATHENA and ARTEMIS software. (Ravel and Newville, 2005)

X-ray photoelectron spectroscopy (XPS) was used to analyze the elemental composition and oxidation states of the samples' surfaces. This analysis was performed at the SUT-NANOTEC-SLRI Joint Research Facility, Synchrotron Light Research Institute (SLRI), Thailand, with the PHI5000 VersaProbe II instrument from ULVAC-PHI, Japan. A monochromatic Al-K $\alpha$  X-ray source ( $h\nu = 1486.6$  eV) was applied to excite the samples. The resulting XPS spectra were processed using the PHI MultiPak XPS software, incorporating Gaussian–Lorentzian line shapes and Shirley background subtraction. Survey spectra were collected with a 1.000 eV energy step and a pass energy of 117.4 eV, while high-resolution spectra were recorded with a 0.05 eV energy step and a pass energy of 46.95 eV. The C1s spectrum, with a binding energy of 284.8 eV corresponding to C–C/C–H, was used as the reference peak.

Elemental analysis (carbon, hydrogen, nitrogen, sulfur) (CHNS, Eurovector EA3000 analyzer, Italy). were conducted to confirm the composition of the synthesized complex.

Thermogravimetric analysis/differential scanning calorimetry (TGA/DSC, Mettler Toledo, United States) was performed at a heating rate of 5 °C min<sup>-1</sup> under a nitrogen flow of 100 mL min<sup>-1</sup> over the temperature range of 35–300 °C.

UV-visible spectrophotometer (UV-vis, PG Instrument T80+ Double Beam Spectrophotometer, United States) was used to analyze the absorption bands of the ImaSMe ligand and its Cu(II)-ImaSMe in 96:4 %V/V acetonitrile-water solutions at varying concentrations. Spectral measurements were recorded in the range of 200–900 nm. Attenuated total reflectance-Fourier transform infrared spectroscopy (ATR-FTIR, Tensor

27, Bruker, Germany) was employed to acquire infrared absorption spectra of the ImaSMe ligand and the Cu(II)-ImaSMe complex.

### 3.2.4 Electrochemical studies

All electrochemical experiments were conducted at 25 °C within a Faraday cage using a standard three-electrode setup. The working electrode was a 2.0 mm diameter gold electrode (CH Instruments, USA). A silver/silver chloride electrode (Ag/AgCl in saturated KCl, ItalSens, Netherlands) served as the reference electrode, and a platinum wire was used as the counter electrode. Prior to each experiment, the working electrode was polished sequentially with water-alumina slurries of 1.0  $\mu\text{m}$ , 0.30  $\mu\text{m}$ , and 0.050  $\mu\text{m}$  (Buehler, USA) on soft lapping pads (Buehler, USA). All electrochemical experiments were performed using a PalmSens4 potentiostat (PalmSens, Netherlands).

The electrochemical characterization of the Cu(II)-ImaSMe was carried out in a solution containing 1.0 mM of the complex and 0.10 M tetrabutylammonium hexafluorophosphate (TBAPF<sub>6</sub>) in a 96:4 %V/V acetonitrile-water mixture, using a gold electrode over a potential range of -2.0 to +2.0 V, with scan rates of 10, 25, 50, 100, 200, and 400 mV s<sup>-1</sup>. Electrochemical impedance spectroscopy (EIS) was used to investigate the electron transfer at the electrode/solution interface. Measurements were conducted in a solution of 5.0 mM [Fe(CN)<sub>6</sub>]<sup>3-/4-</sup> in 0.10 M KCl, covering a frequency range from 1 Hz to 10<sup>5</sup> Hz with an amplitude of 5 mV.

### 3.2.5 Creatinine analysis

Urine samples were collected from three healthy volunteers following ethical guidelines. Ethical approval for the study was granted by the Human Research Ethics Office of the Institute of Research and Development, Suranaree University of Technology (approval code: EC-67-0149). The samples were immediately stored at 4 °C and analyzed within three days. Before analysis, the urine samples were diluted ten-fold with 0.10 M KCl and analyzed using cyclic voltammetry at 25 °C. Measurements were conducted using a Cu(II)-ImaSMe-modified gold macroelectrode over a potential range of -0.7 V to +0.7 V at a scan rate of 50 mV s<sup>-1</sup>. Creatinine quantification was performed using the standard addition method, where known concentrations of creatinine (2.0, 5.0, 10.0, and 15.0 mM) were added to the diluted urine samples. Cyclic voltammetry measurements were repeated under the same conditions after each addition.

## CHAPTER IV

### RESULTS AND DISCUSSION

#### 4.1 Guanosine detection

First, the electrooxidation of guanosine was investigated using voltammetric techniques at both stationary and rotating electrodes. Subsequently, DFT calculations were performed to enhance our understanding of the guanosine oxidation mechanism and explore the most favorable reaction pathway. Finally, an electrochemical sensor utilizing a carbon fiber microelectrode was developed for detection of guanosine.

##### 4.1.1 Cyclic voltammetry of guanosine at a stationary glassy carbon electrode

Cyclic voltammetry of guanosine showed an oxidation peak at 1.07 V at a scan rate of 10 mV s<sup>-1</sup> (Figure 4.1a). No reduction peak was observed in the backward scan, indicating a chemically irreversible nature of the oxidation process of guanosine.

##### 4.1.1.1 Tafel analysis

The cyclic voltammetry results were next subjected to Tafel analysis (equation (1)) to investigate the kinetics of electron transfer in the oxidation of guanosine. (Batchelor-McAuley and Compton, 2012)

$$\frac{\partial \ln I}{\partial E} = \frac{(n' + \beta_{n'+1})F}{RT} \quad (1),$$

where  $I$  is the electrical current,  $E$  is the applied potential,  $n'$  is the number of electrons transferred before the rate determining electron transfer step,  $\beta_{n'+1}$  is the anodic transfer coefficient of the rate determining electron transfer step,  $R$  is the molar gas constant (8.314 J K<sup>-1</sup> mol<sup>-1</sup>),  $T$  is absolute temperature (K), and  $F$  is the Faraday's constant (96485 C mol<sup>-1</sup>).

The Tafel analysis was performed using currents within the range of 15% to 50% of the peak currents ( $E = 0.89$  to  $0.95$  V, plotted in red in Figure 4.1a) to minimize the influence represents the number of electrons transfer before the rate-determining step, and as such, it can only assume integer values (0, 1, 2, ...). Meanwhile,  $\beta_{n'+1}$  denotes the transfer coefficient for the rate-determining electron transfer step, and its value must fall within of solution-phase mass transport.

From the Tafel analysis, the value of  $n' + \beta_{n'+1}$  was determined to be  $0.67 \pm 0.02$  (see inlay of Figure 4.1a). It is important to note that  $n'$  the range of  $0 < \beta_{n'+1} < 1$ . Given that  $n'$  and  $\beta_{n'+1}$  contribute to  $n' + \beta_{n'+1}$ , which is measured as  $0.67 \pm 0.02$ , the only feasible values for  $n'$  and  $\beta_{n'+1}$  are 0 and  $0.67 \pm 0.02$ , respectively. The results therefore revealed the value of  $n'$  to be zero, indicating that the first electron transfer is a rate-determining step (RDS) with the anodic transfer coefficient of this RDS ( $\beta_{n'+1}$ ) of  $0.67 \pm 0.02$ .

#### 4.1.1.2 Effects of scan rates

The effect of scan rates on the electrooxidation of guanosine was investigated in Figure 4.1b. The oxidation peak currents exhibited a linear increase with the square root of the scan rates ( $\sqrt{\nu}$ ), as demonstrated in the inlay of Figure 4.1b. These results suggest that guanosine oxidation at a glassy carbon electrode follows a diffusion-controlled process. Moreover, as the scan rate ( $\nu$ ) increased, the peak position shifted towards higher overpotentials, indicating the electrochemically irreversible nature of the process. The plot of  $E_p$  against  $\log \nu$  yielded a slope of  $24 \pm 3$  mV per decade of  $\log \nu$ .

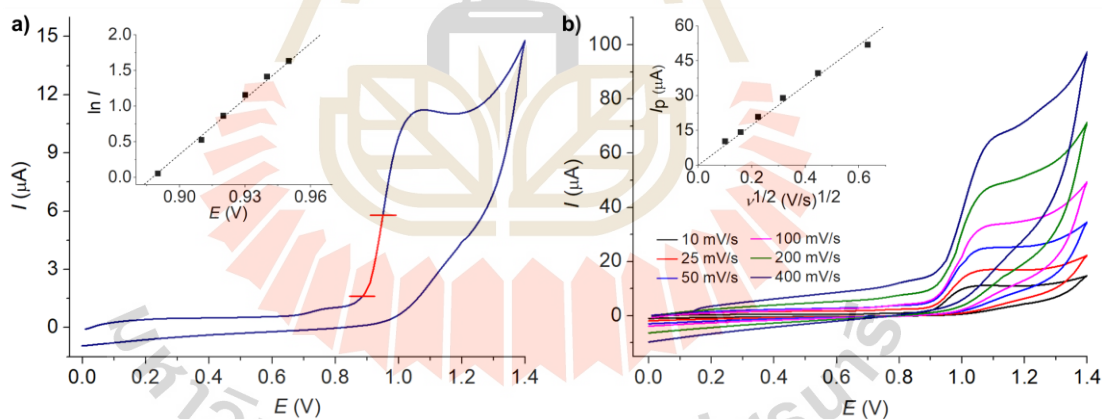
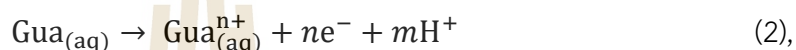


**Figure 4.1** Cyclic voltammogram of 1.0 mM guanosine at a stationary glassy carbon macroelectrode in a PBS buffer solution pH 7.0 a) at a scan rate of  $10 \text{ mV s}^{-1}$ . The inlay shows the plot of  $\ln I$  vs.  $E$  in Tafel analysis, b) at different scan rates ( $10 - 400 \text{ mV s}^{-1}$ ). The inlay shows the plot of peak currents ( $I_p$ ) against the square root of scan rates ( $\nu^{1/2}$ ).

#### 4.1.1.3 Effects of pH

The effect of pH on the electrooxidation of guanosine was investigated in the pH range from 1.00 to 14.0, and the results are presented in Figure 4.2. The findings revealed that as the pH of the solution increased, the oxidation peaks shifted to lower overpotentials. This observation suggests that the oxidation of guanosine becomes more thermodynamically favorable at higher pH, indicating the involvement of a deprotonation process in the electrooxidation of guanosine (Gua), as described by equation (2).



The plot of peak potentials ( $E_p$ ) against pH exhibited a linear relationship with a slope of  $41.2 \pm 1.2 \text{ mV pH}^{-1}$  (see the inlay of Figure 4.2). According to the Nernst equation (equation (3)), the experimentally observed value is close to the theoretical value of an  $ne^{-} n\text{H}^{+}$  process, (Chang, Cheng, and Chao, 2004) similar to the previous literature report. (Zhu, Chu, et al., 2021)

$$E_p = E^0 - \frac{RT}{nF} \ln \frac{[\text{Gua}^{n+}]}{[\text{Gua}]} + 2.303 \frac{mRT}{nF} \text{pH} \quad (3),$$

where  $E_p$  is the peak potential,  $E^0$  is the standard electrode potential,  $R$  is the molar gas constant ( $8.314 \text{ J K}^{-1} \text{ mol}^{-1}$ ),  $T$  is the absolute temperature (K),  $n$  is the total number of electrons transfer,  $F$  is the Faraday's constant ( $96485 \text{ C mol}^{-1}$ ),  $m$  is the number of protons transfer, and  $n$  is the number of electrons transfer.

The peak currents were 45.7, 33.9, 30.0, 35.1, 33.0, and 33.2  $\mu\text{A}$  for pH 1.0, 4.0, 7.0, 11.0, 13.0, and 14.0, respectively. Notably, the highest current was recorded at pH 1.0. However, it is important to note that at this acidic pH, the oxidation response of guanosine was interfered by the oxygen evolution reaction. In consideration of practical applications and physiological relevance, we have selected the neutral pH condition (pH 7.0) for further investigation in the subsequent sections.

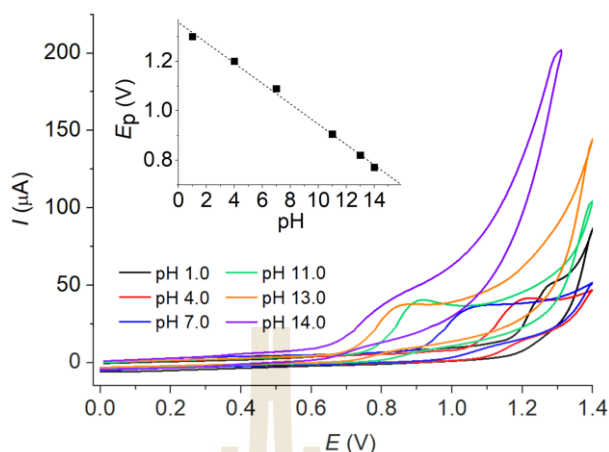


**Figure 4.2** Cyclic voltammograms of 1.00 mM guanosine at a stationary glassy carbon macroelectrode in buffer solutions of different pH (from 1.0 to 14.0) at a scan rate of  $100 \text{ mV s}^{-1}$ . The inlay shows the plot of peak potentials ( $E_p$ ) against pH

#### 4.1.1.4 Calibration plots

Figure 4.3a shows cyclic voltammograms of guanosine at various concentrations in a PBS buffer solution with a pH of 7.0. The peak currents exhibited a linear relationship with guanosine concentrations within the range of 0.067 – 1.00 mM. The sensitivity of the method was determined to be  $30.64 \pm 0.86 \mu\text{A mM}^{-1}$ , with a limit of detection of 0.02 mM ( $3S_B/m$ ). The method also demonstrated excellent reproducibility with the relative standard deviation (RSD) of 2.72% ( $n = 5$ ) for the measurement at 1.00 mM guanosine.

In addition to voltammetry, the concentrations of guanosine can be evaluated using chronoamperometric measurements by the application of a high overpotential of 1.20 V, as shown in Figure 4.3b. The amperometric currents increased linearly with guanosine concentrations in the range of 0.00 – 1.00 mM. The amperometric method exhibited a sensitivity of  $9.88 \pm 0.28 \mu\text{A mM}^{-1}$ , and a limit of detection of 0.02 mM ( $3S_B/m$ ).

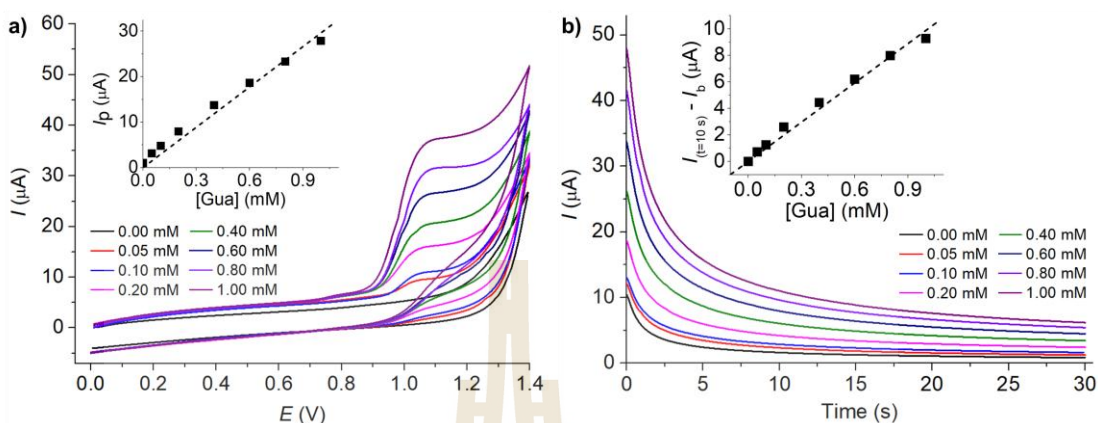


**Figure 4.3** a) Cyclic voltammograms at a scan rate of  $100 \text{ mV s}^{-1}$  and b) chronoamperograms at the applied potential of  $1.20 \text{ V}$  at a stationary glassy carbon macroelectrode of varied concentrations of guanosine in a PBS buffer solution pH 7.0. The inlays show the calibration plots of a) peak currents ( $I_p$ ) and b) the background subtracted amperometric currents at  $10 \text{ s}$  ( $I_{(t=10s)} - I_b$ ) against the concentrations of guanosine.

#### 4.1.2 Cyclic voltammetry of guanosine at a rotating glassy carbon macroelectrode

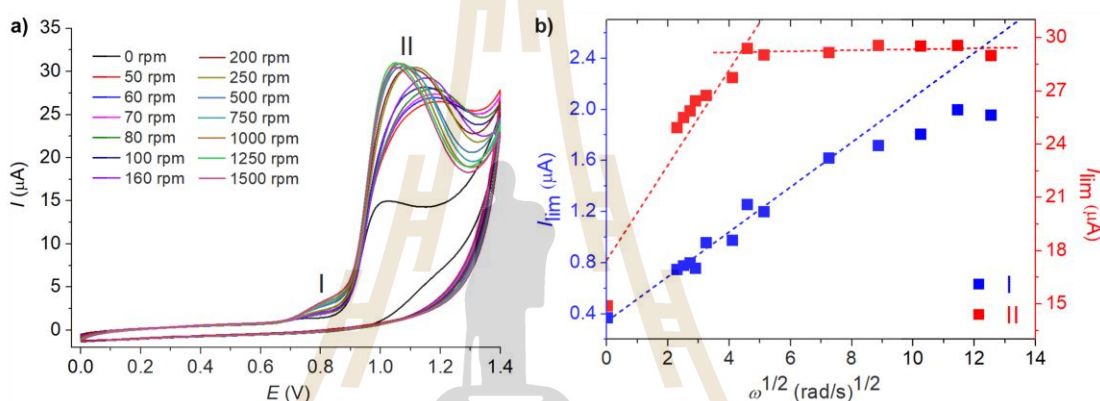
In the voltammetry experiments conducted with a rotating glassy carbon macroelectrode, two distinct types of oxidation responses were observed: a steady-state response (designated as I in Figure 4.4a) and a peak response (designated as II in Figure 4.4a). The steady-state response indicates a mass transport-controlled process, which occurs in the potential range of approximately  $0.75 - 0.85 \text{ V}$ . Interestingly, a small peak was also observed at the stationary macroelectrode (Figure 4.1a) within this range. Notably, the appearance of Peak II at a rotating electrode suggests the occurrence of a subsequent process that is not governed by mass transport (diffusion/convection). This process takes place after the mass transport-controlled process in the steady-state region. One possible explanation is the formation of an adsorbed product that inhibits further electron transfer.

Figure 4.4b analyzes the relationship between the electrochemical responses of guanosine and the electrode rotation speeds. The magnitudes of both responses, I and II, exhibited an increase with the rotation speed of the electrode.

However, at fast rotation speeds, the currents deviated from the linear trend predicted by the Levich equation (equation 4) for limiting currents ( $I_{lim}$ ) and the square root of electrode rotation speeds ( $\omega^{1/2}$ ).

$$I_{lim} = 0.62nAFD^{2/3}\omega^{1/2}\nu^{-1/6}c^* \quad (4),$$

where  $I_{lim}$  is the limiting current,  $n$  is the number of electrons transferred,  $F$  is the Faraday constant ( $96,485 \text{ C mol}^{-1}$ ),  $A$  is the surface area of the electrode,  $D$  is the diffusion coefficient,  $\omega$  is the electrode rotation speed ( $\text{rad s}^{-1}$ ),  $\nu$  is the kinetic viscosity, and  $c^*$  is the bulk concentration of guanosine.



**Figure 4.4** a) Cyclic voltammograms of 1.00 mM guanosine in a pH 7.0 PBS buffer solution at a rotating glassy carbon macroelectrode at various electrode rotation speeds ( $\omega = 0 - 1500 \text{ rpm}$ ). b) The Levich plots of  $I_{lim}$  vs  $\omega^{1/2}$ .

#### 4.1.3 Cyclic voltammetry of guanosine at a stationary carbon fiber microelectrode (CFE)

The oxidation of guanosine was further investigated using a stationary carbon fiber microdisk electrode (CFE). Figure 4.5 illustrates that even at a slow scan rate of  $10 \text{ mV s}^{-1}$ , the voltammograms at the microelectrode displayed peak-shaped responses instead of reaching steady state. These findings suggest the presence of electrochemically inert products forming on the electrode's surface, (Ngamchuea, Tharat, Hirunsit, and Suthirakun, 2020) consistent with the observations at the rotating electrode in the previous section.

Figure 4.5 also demonstrates that the peak currents exhibited a linear relationship with guanosine concentrations within two distinct linear ranges:  $0.010 - 0.13 \text{ mM}$  and  $0.13 - 1.00 \text{ mM}$ . The sensitivities for these ranges were determined to be  $1.13 \pm 0.05 \text{ nA mM}^{-1}$  and  $0.08 \pm 0.003 \text{ nA mM}^{-1}$ , respectively. The presence of the two distinct linear ranges may be attributed to the complex nature of guanosine oxidation.

While the reaction was determined to be diffusion-controlled, the oxidation of guanosine is, in fact, a complex multi-step process, as discussed in the following section. At a microelectrode, the convergent diffusion regime is significantly different from the planar diffusion at a macroelectrode. This variance results in a higher level of efficiency in the diffusion of intermediates or products away from the electrode surface. This affects the extent of interaction between relevant species with the electrode, as well as interactions among different species in the vicinity of the electrode, leading to adjustments in the concentrations of the involved species in the vicinity of the electrode interface. These alterations have the potential to influence the extent of dominant pathway of the reaction, consequently affecting the sensitivity of the measurements. The limit of detection for guanosine measurement at the CFE was determined to be 0.003 mM ( $3S_B/m$ ). To assess the reproducibility of guanosine measurements at the CFE, a PBS buffer solution at pH 7.0 with a guanosine concentration of 0.60 mM was evaluated, resulting in a relative standard deviation (RSD) of 2.01% ( $n = 5$ ).

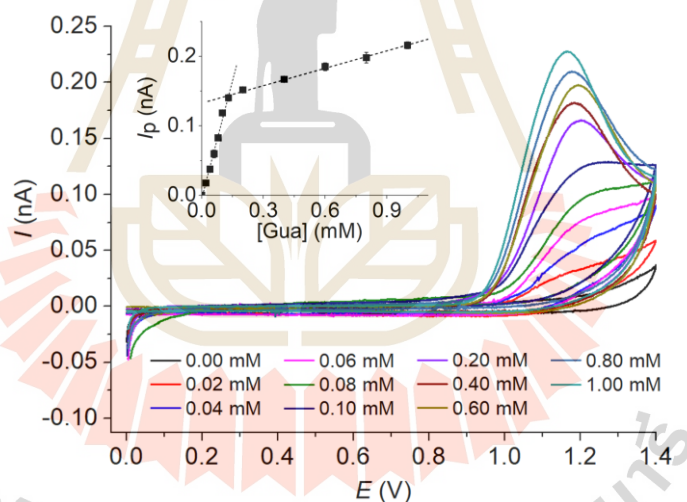


**Figure 4.5** Cyclic voltammograms at a stationary carbon fiber microelectrode of varied guanosine concentrations (0.00 – 1.00 mM) in a pH 7.0 PBS buffer solution at a scan rate of  $10 \text{ mV s}^{-1}$ . The inlay shows the calibration plot of peak currents ( $I_p$ ) against guanosine concentrations.

#### 4.1.4 Stationary glassy carbon macroelectrode vs. rotating glassy carbon macroelectrode vs. stationary carbon fiber microelectrode

This section provides a summary and comparison of the oxidation of guanosine at the three types of working electrodes under investigation.

The voltammetric responses obtained from a stationary macroelectrode revealed a linear relationship between peak currents and the square root of scan rates, indicating that the main oxidation peak of guanosine at ca. 1.07 V was controlled by diffusional mass transport. However, when using a rotating electrode, the voltammetric response at the same potential increased with electrode rotation speeds only at relatively low speeds. At faster electrode rotation, the currents at this potential were no longer affected by changes in electrode rotation speeds. Additionally, a peak-shaped response was observed instead of a steady-state response at the rotating electrode, which was different from typical mass-transport-controlled systems.

The difference observed between stationary and rotating macroelectrodes can be attributed to the fact that, at the stationary macroelectrode, only a relatively small quantity of inert product is generated within the experimental timescale. Consequently, any effect of electrode fouling at the stationary macroelectrode is only evident as an influence on the apparent electron transfer kinetics. In contrast, when using the rotating electrode, hydrodynamic flow enhances the reaction at the electrode, leading to a significant buildup of electrode fouling, ultimately blocking the electrode from further reactions. Similar to the observations at the rotating electrode, a carbon fiber microelectrode, with the efficient convergent/radial diffusion, also exhibited a peak-shaped response rather than a steady-state response. This finding is consistent with the hypothesis that the formation of an adsorbed inert product inhibits further electron transfer at the electrode surface.

#### 4.1.5 Mechanistic studies by DFT calculation

To gain insights into the reaction mechanisms involved in the oxidation of guanosine in an aqueous solution, we conducted density functional theory (DFT) calculations to investigate the most favorable reaction pathway. The calculated reaction energies for all elementary steps are presented in Figure 4.6.

The energy profile (Figure 4.6a) of guanosine (G1) conversion reveals that the initial step involves an electron transfer coupled with a proton abstraction from guanosine, resulting in the formation of the G2 radical intermediate. This initial step requires substantial potential energy of 8.84 eV. The high-energy G2 intermediate formed in the first step is susceptible to hydrolysis, leading to the formation of the G3 radical. Subsequently, this radical can further lose an electron, resulting in the formation of 8-hydroxyguanosine (G4). The hydrolysis of guanosine, guanine, and their derivatives as well as the formation of 8-hydroxyguanosine in guanosine oxidation have

been experimentally observed in the literatures. (R. Goyal and Dryhurst, 1982; R. N. Goyal, Jain, and Garg, 1997; R. N. Goyal, Puri, and Jain, 2001)

Although 8-hydroxyguanosine (G4) itself is relatively energetically stable, the energy required for the conversion of G4 to G5 (Pathway A), which amounts to 7.18 eV, is lower than the energy required for the conversion of G1 to G2 (8.84 eV). Consequently, the energy provided is sufficient for the further reaction of 8-hydroxyguanosine. This results in a spontaneous subsequent reaction, leading to the formation of G8 and G9 as intermediates, and G12 and G13 as the final products. The compounds G12 (2-iminodihydropyrimidine-4,5,6(1H)-trione) and G13 (urea ribose) have been previously detected in the oxidation of guanosine at pH ~3. (R. N. Goyal, Jain, and Garg, 1997)

Meanwhile, the conversion of G4 to G6 in Pathway B requires an energy of 11.07 eV. Although this step requires higher energy compared to the G4 to G5 conversion in Pathway A, in the context of electrochemical measurements, where a high overpotential is applied to drive the oxidation of guanosine, this step can occur. More importantly, the formation of the G7 dimer is considerably more energetically favorable than the formation of G6. In addition, the formation of the stable dimer product aligns with experimental data, indicating the presence of electrochemically inert products formed on the electrode's surface. The occurrence of the dimer product is also supported by previous mass spectrometry reports. (R. N. Goyal, Jain, and Garg, 1997) It is therefore proposed that the oxidation of guanosine can occur via both Pathways A and B, as summarized in Figure 6b. However, by combining experimental and computational findings, it is suggested that in the neutral conditions employed in this work, Pathway B, which leads to the formation of the dimer product, is likely the dominant pathway.

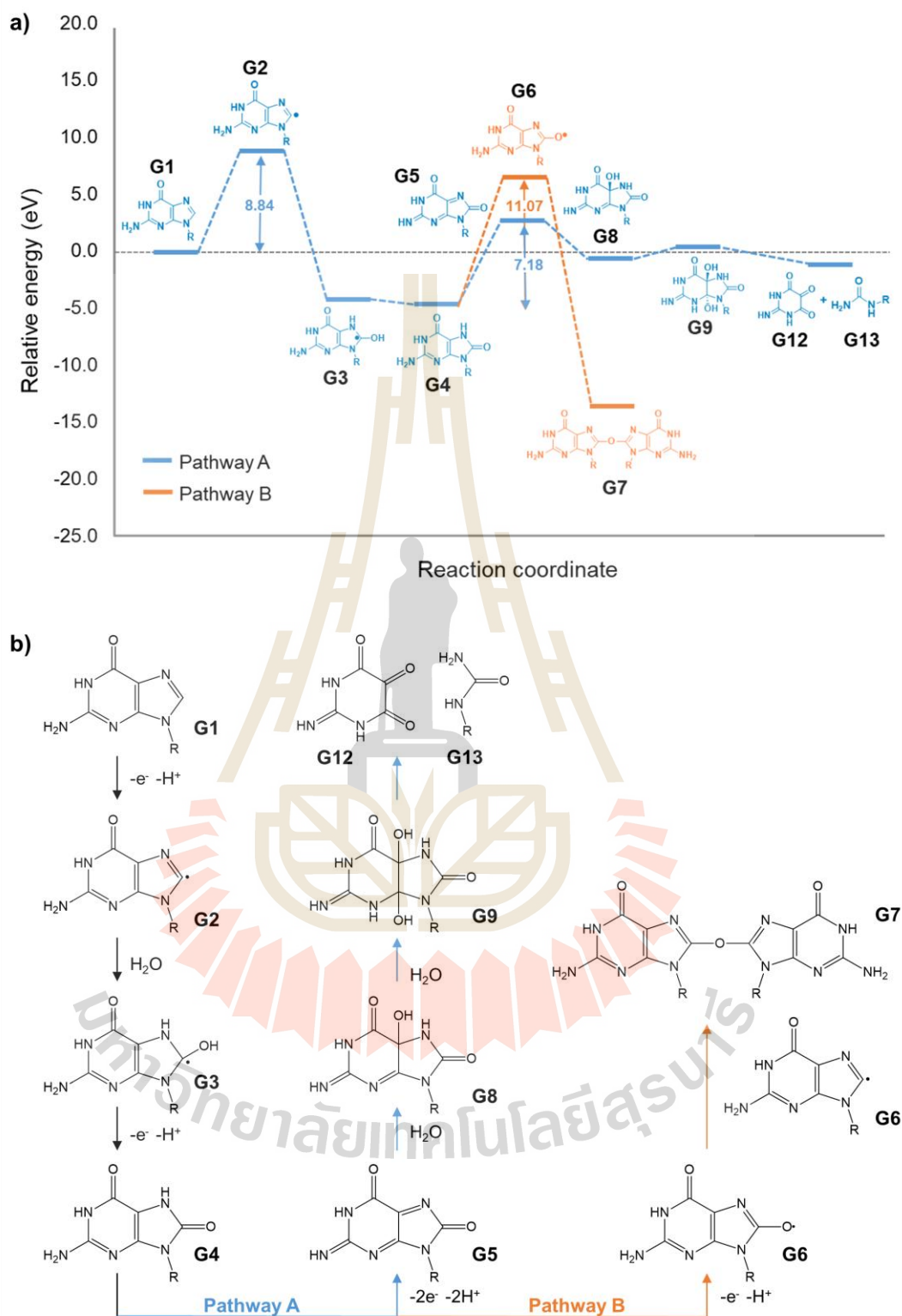


**Figure 4.6** a) The calculated energy profile for guanosine oxidation in an aqueous solution. b) The proposed reaction mechanism of guanosine oxidation.

#### 4.1.6 Interference studies and application in synthetic urine sample

The selectivity of the sensor was tested using potential interferences at concentrations ten times that of guanosine. The tested interferences included common molecular metabolites in urine, such as glucose and creatinine, as well as cations like  $\text{Li}^+$ ,  $\text{Na}^+$ ,  $\text{K}^+$ ,  $\text{Mg}^{2+}$ , and anions such as  $\text{Cl}^-$ ,  $\text{Br}^-$ ,  $\text{CO}_3^{2-}$ ,  $\text{SO}_4^{2-}$ . No significant changes (<5%) in the peak currents were observed during guanosine measurements at the carbon fiber microelectrode upon the addition of all the tested interferences, demonstrating excellent selectivity of the developed sensor for guanosine detection (Figure 4.7).

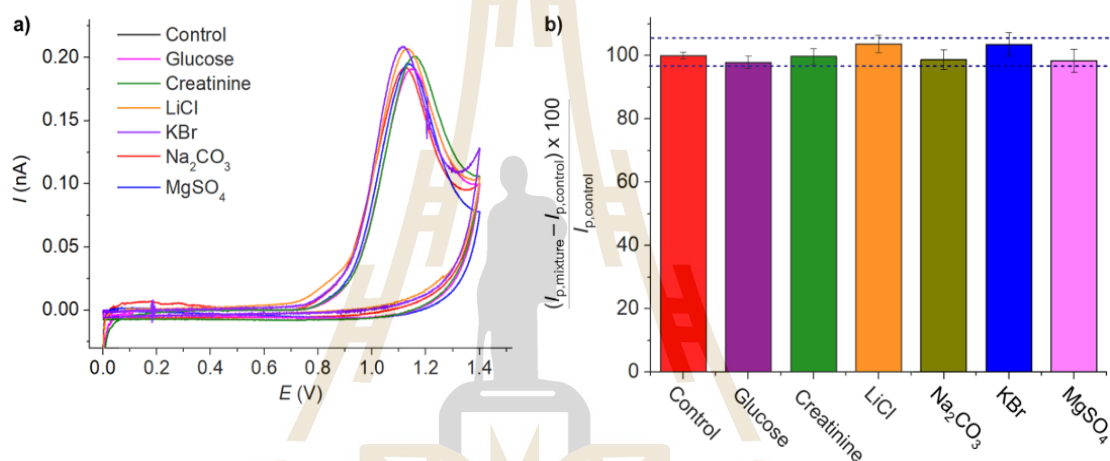


**Figure 4.7** a) Cyclic voltammograms of 1.00 mM guanosine in PBS pH 7.0 in the absence and presence of interferences at a stationary carbon fiber microelectrode at a scan rate of  $10 \text{ mV}^{-1}$ . b) The analysis of  $(I_{p,\text{mixture}} - I_{p,\text{control}}) \times 100 / I_{p,\text{control}}$  for different interfering species.

The method of guanosine detection at a carbon fiber microelectrode was next validated through spiking and recovery tests (standard addition) in synthetic urine, both in the presence and absence of supporting electrolytes. The synthetic urine sample was prepared according to Jiang, et al. (Jiang et al., 2016) with the following composition: 170.0 mM urea, 1.1 mM sodium L-lactate, 2.0 mM citric acid, 25.0 mM sodium bicarbonate, 90.0 mM sodium chloride, 2.0 mM magnesium sulfate, 10.0 mM sodium sulfate, 7.0 mM sodium phosphate monobasic, 7.0 mM sodium phosphate dibasic, and 25.0 mM ammonium chloride.

The synthetic urine sample was spiked with 0.05 mM guanosine and diluted 20-fold in either a pH 7.0 PBS buffer solution (with 0.10 M KCl) or deionized water. Voltammetric measurements were then performed at a CFE. Standard addition tests were conducted by subsequently spiking the solutions with increasing

concentrations of guanosine. The results were expressed as percentage recoveries, calculated as the mean value of triplicate measurements  $\pm$  standard deviation. The percentage recoveries were determined to be  $98.39 \pm 3.69\%$  (RSD = 4.66%) and  $99.71 \pm 4.02\%$  (RSD = 4.95%) in the presence and absence of added supporting buffer electrolyte, respectively. For additional details on recovery studies, please refer to Table 4.1. We have therefore demonstrated that guanosine can be detected directly at the carbon fiber microelectrode and this method proves to be effective in detecting guanosine in samples with low ionic strength, eliminating the requirement for electrolyte supplementation. Notably, our approach exhibits remarkable selectivity for guanosine even in the presence of interfering substances within the synthetic urine matrix.

**Table 4.1** Spike and recovery tests of guanosine in synthetic urine.

Sample	Guanosine added (mM)	Guanosine detected (mM)	%Recovery	%RSD
Synthetic urine in the presence of PBS buffer pH 7.0 and 0.10 M KCl	0.050	0.0492	98.39	4.66
Synthetic urine in the absence of added supporting electrolyte	0.050	0.0499	99.71	4.95

## 4.2 Creatinine detection

This study focused on exploring the physical and chemical characteristics of Cu(II)-ImsMe in detail. The electrochemical behavior of creatinine on a gold electrode modified with Cu(II)-ImsMe was analyzed using cyclic voltammetry to understand the underlying reaction mechanism. Furthermore, an electrochemical sensor was developed for creatinine detection and successfully utilized to measure creatinine levels in real samples, demonstrating its practical applicability.

### 4.2.1 Physicochemical properties of Cu(II)-ImsMe

To elucidate the structural features of the synthesized Cu(II)-ImsMe complex, single-crystal X-ray diffraction analysis was performed on suitable yellowish-brown

block crystals obtained by slow evaporation from a CH<sub>2</sub>Cl<sub>2</sub>:MeOH solution. The results revealed that the complex crystallizes in the triclinic space group  $P\bar{1}$ .

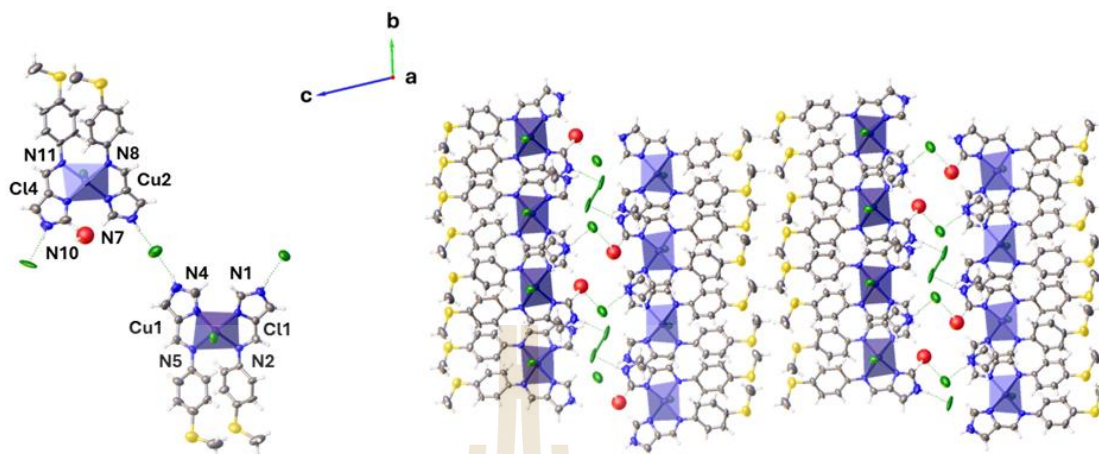
At 150 K, the asymmetric unit comprises two distinct Cu(II) centers, chloride counterions, and one H<sub>2</sub>O molecule. Each Cu(II) center has a distorted trigonal bipyramidal geometry (Addison, Rao, Reedijk, van Rijn, and Verschoor, 1984), as indicated by  $\tau_5$  values of 0.74 (see Table 4.2), formed by two bidentate lmaSMe ligand and one chloride. The two Cu(II) centers are very similar with only small differences in their Cu(II)–N bond distances (Table 4.2).

Figure 4.8 shows the packing is generated by strong hydrogen bonding between the imidazole N–H and the chloride counter ion forming a one-dimensional chain. Neighbouring chains face each other with the chloride and water molecules forming channels in between the chains. In this arrangement the methylthiophenyl groups face each other held together by multiple C–H...S interactions creating an amphiphilic-like sheet in the *bc* plane. These sheets are further linked by C–H... $\pi$  and C–H...Cl<sub>ligand</sub> interactions within the *ab* plane. The preferential orientation of the S–Me groups likely allows efficient self-assembly of the compound on the Au surface due to strong Au...S interactions or even coordination bonds. This leaves the imidazole unit which has multiple H–bond donor and acceptor sites free to interact with creatinine analyte.

To further confirm the crystalline nature of the synthesized Cu(II)-lmaSMe, powder X-ray diffraction (XRD) analysis was conducted, as shown in Figure 4.9. The XRD pattern exhibits distinct diffraction peaks at specific  $2\theta$  angles, notably at 4.26°, 6.41°, 9.28°, 10.70°, 12.53°, 14.23°, and 16.22°. These peaks indicate well-defined crystal planes and corroborate the findings from the single-crystal XRD analysis.

**Table 4.2** Bond lengths and geometry parameters of the Cu(II)-lmaSMe complex.

	Cu1	Cu2
T (K)	150	150
Cu–N <sub>imidazole</sub> (Å)	1.966(5), 2.022(5)	1.975(5), 2.002(5)
Cu–N <sub>imine</sub> (Å)	2.153(5), 2.037(5)	2.150(5), 2.047(5)
Cu–Cl (Å)	2.4038(16)	2.4041(16)
$\tau_5$	0.74 (trigonal bipyramidal)	0.74 (trigonal bipyramidal)



**Figure 4.8** Asymmetric unit and amphiphilic-like packing of the Cu(II)-ImaSMe complex.

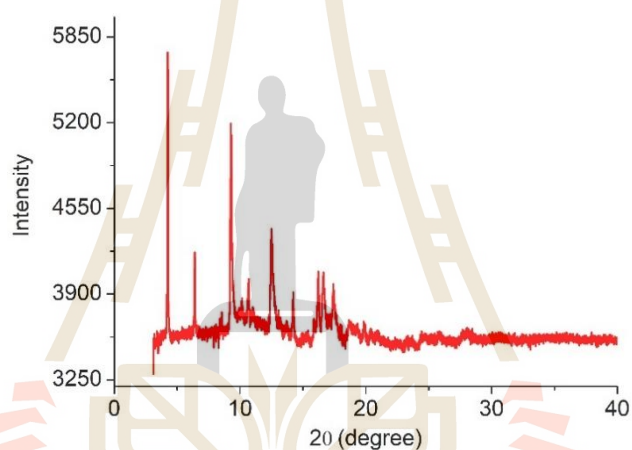


**Figure 4.9** Powder XRD of Cu(II)-ImaSMe complex.

To further investigate the oxidation state and local environment of the copper centers in the Cu(II)-ImaSMe complex (figure 4.10a), X-ray Absorption Near Edge Structure (XANES) and Extended X-ray Absorption Fine Structure (EXAFS) analyses were performed at the Cu K-edge, as depicted in Figure 4.10b. The Cu K-edge peak was observed at 8996 eV, indicating that copper is in the +2 oxidation state (Huang, Wang, and Lee, 2003).

The K-edge energy prior to the scattering path was found to be 8987 eV, matching values reported for Cu(II) complex (Gaur, Shrivastava, and Joshi, 2009). The EXAFS data in R-space were fitted to a scattering model derived from the single-crystal X-ray diffraction (SCXRD) structure of complex (Pinitsoontorn et al., 2014). The data fit well to the model of the Cu2 center from the structure within a range of 3 Å, achieving an R-factor of 0.028, as shown in Figure 4.10c.

The first coordination shell in the EXAFS fitting includes the nitrogen donor atoms from the imidazole and imine motifs of the ligand, which corresponds well to the signal up to 2 Å. The subsequent shell fitting was completed using scattering paths consistent with the carbon backbone of the ligand. Slight differences between the crystal structure and the material beyond the coordination sphere are expected, given that interaction between the Cu(II)-ImaSMe complex and the gold surface may alter the precise orientation of the ImaSMe ligand.

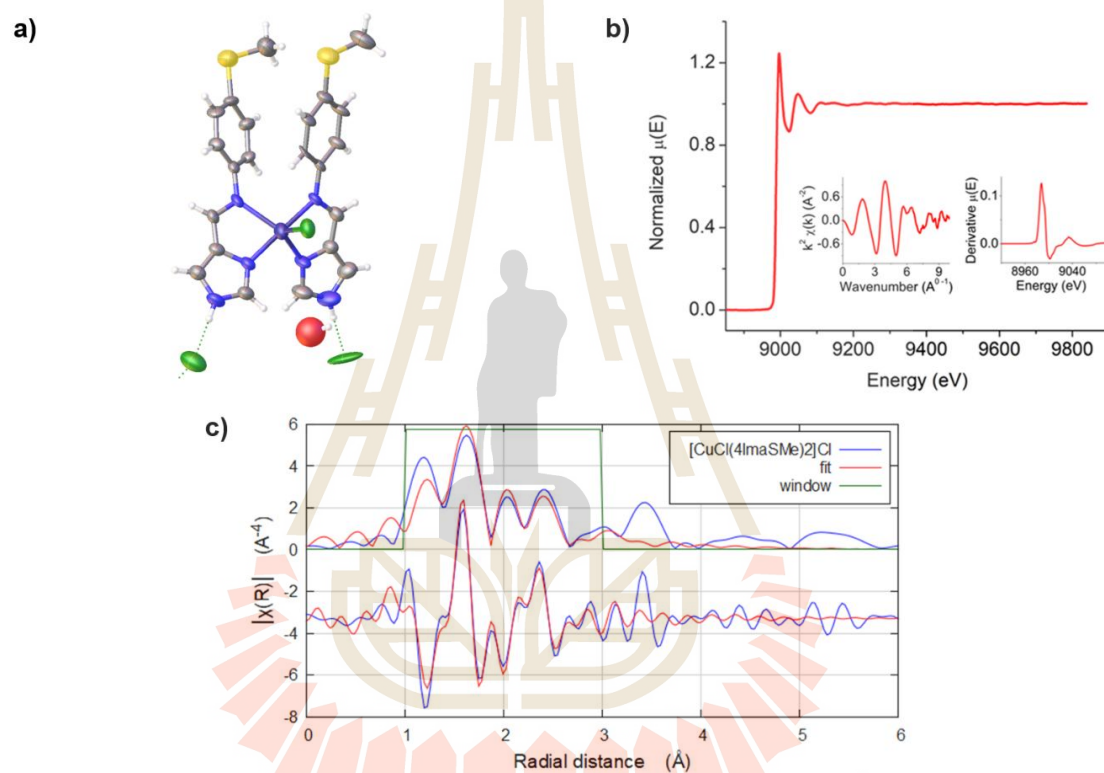


**Figure 4.10** a) structure of Cu(II)-ImaSMe complex, b) Cu K-edge EXAFS data, and c) model fitting in *R*-space and *k*-space alongside with the atoms contributing to the scattering path.

The X-ray photoelectron spectra of the Cu(II)-ImaSMe complex, both before and after its interaction with creatinine, are presented in Figure 4.11. The XPS results for Cu 2p<sub>3/2</sub> and Cu 2p<sub>1/2</sub> reveal distinct features before and after interaction, indicating changes in the electronic environment of copper. Prior to interaction, the Cu 2p<sub>3/2</sub> and Cu 2p<sub>1/2</sub> peaks were split into two components, with binding energies of 933.0 and 952.8 eV corresponding to Cu<sup>2+</sup> and additional peaks at 935.6 and 955.4 eV associated with Cu<sup>+</sup>. (Li, Wang, Chai, and Yang, 2023)

Following electrochemical detection of creatinine, similar splitting was observed; however, the binding energies shifted slightly to 934.8 and 954.6 eV for  $\text{Cu}^{2+}$  and 937.1 and 956.9 eV for  $\text{Cu}^+$ , reflecting modifications in copper's chemical state. In the C 1s spectrum, peaks at 285.8 eV (C=N/C-N) and 286.7 eV (C-S/C-S-C) confirm the presence of these functional groups. (D. Chen et al., 2019) The N 1s spectrum shows peaks at 399.1 eV (Cu-N), 400.3 eV (C=N/C-N) and 401.6 eV (-NH). (Ge, Li, Zhang, and Liu, 2022) In the S 2p spectrum, peaks at 163.4 eV and 164.6 eV are attributed to C-S and C-S-C bonds. (Varodi et al., 2021) Additionally, the Cl 2p<sub>3/2</sub> and Cl 2p<sub>1/2</sub> peaks, observed at binding energies of 197.9 eV and 199.5 eV, respectively, are consistent with  $\text{Cl}^-$  species. (Moreira Da Silva et al., 2023)

After electrochemical detection of creatinine, notable shifts were observed in the spectra. In the C 1s spectrum, the C=N/C-N peak shifted to 286.0 eV, the (C-S/C-S-C) peak shifted to 286.9 eV and new peak at 287.9 eV (C=O). In the N 1s spectrum, the (Cu-N) shifted to 399.5 eV, the C=N/C-N peak shifted to 401.1 eV, and the -NH peak to 402.3 eV. Similarly, in the S 2p spectrum, the C-S and C-S-C peaks shifted to 165.3 eV and 166.5 eV, reflecting alterations in sulfur-containing bonds. Lastly, the Cl 2p<sub>3/2</sub> and Cl 2p<sub>1/2</sub> peaks shifted to 199.4 eV and 201.1 eV, respectively, indicating changes in the chloride environment.

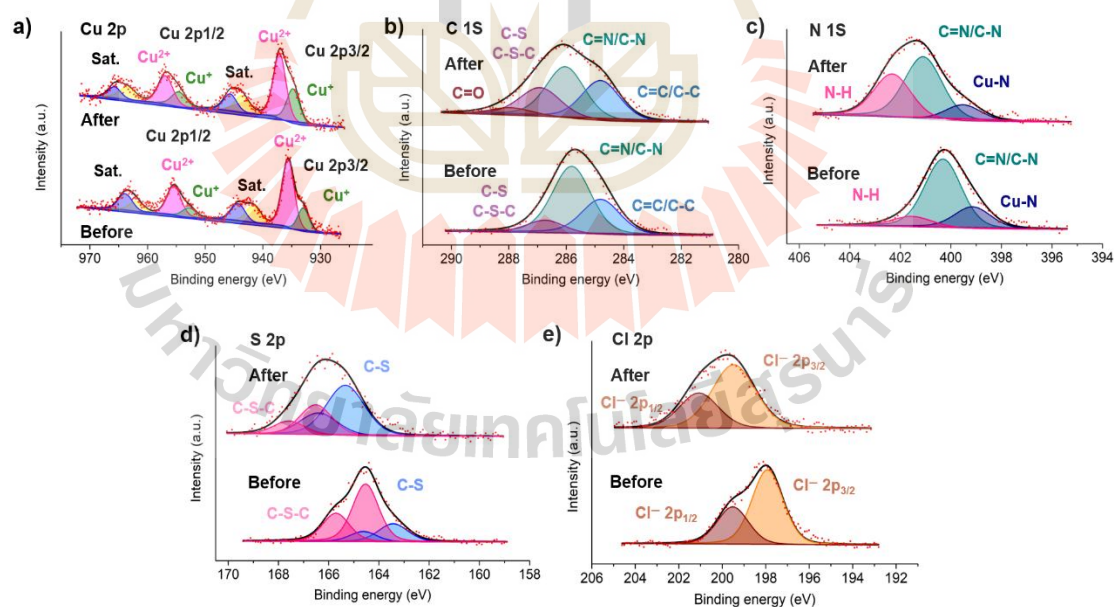


**Figure 4.11** XPS spectra of the Cu(II)-ImaSMe complex are presented, illustrating the peaks for a) Cu 2p, b) C 1s, c) N 1s, d) S 2p, and e) S 2p, both before and after electrochemical detection of creatinine.

The scanning electron microscopy (SEM) images of the synthesized Cu(II)-ImaSMe complex, as illustrated in Figure 4.12a, reveal the particles predominantly exhibiting rectangular or rod-like geometries with well-defined edges.

The average Feret diameter of these particles is  $121 \pm 38$  nm, with sizes ranging from 63 nm to 275 nm.

Elemental analysis (carbon, hydrogen, nitrogen, sulfur) was performed to confirm the composition of the synthesized complex. The analysis yielded the following percentages: 44.71% C, 3.97% H, 14.41% N, and 10.71% S. These values are slightly lower than the theoretical percentages calculated for the formula  $C_{22}H_{22}Cl_2CuN_6S_2$ , which are 46.44% C, 3.90% H, 14.77% N, and 11.27% S. The slight discrepancies between the calculated and observed values suggest the presence of additional components, such as water molecules or solvent residues, within the crystalline lattice.

To investigate this further, thermogravimetric analysis (TGA) was carried out to determine and quantify the presence of water molecules or other volatile components in the complex. Figure 4.12b shows the TGA curves for the Cu(II)-ImaSMe complex. The TGA measurements were performed under a nitrogen atmosphere with a flow rate  $100 \text{ mL min}^{-1}$  and a heating rate of  $5 \text{ }^\circ\text{C min}^{-1}$ , ranging from 35 – 300  $^\circ\text{C}$ . An initial weight loss of 3.07% is observed between 35 and 100  $^\circ\text{C}$ , corresponding to the loss of one water molecules. This observation aligns with the elemental analysis results, confirming the presence of water in the crystalline lattice. The Cu(II)-ImaSMe complex starts to decompose at approximately 200  $^\circ\text{C}$ , as evidenced by a significant weight loss due to the breakdown of the ligand framework. Because the electrochemical study was conducted at temperatures below 200  $^\circ\text{C}$ , this decomposition does not impact the experimental results.

The Fourier-transform infrared (FTIR) spectra of the ImaSMe ligand and the Cu(II)-ImaSMe complex were recorded in the region of  $4000 - 400 \text{ cm}^{-1}$ , as shown in Figure 4.12c. For the ImaSMe ligand, the C=N stretching vibration (imine) was observed at  $1627 \text{ cm}^{-1}$ , while the aromatic C–N stretching (amine) appeared at  $1329 \text{ cm}^{-1}$ . The S–H stretching vibration (thiol) occurred at  $2590 \text{ cm}^{-1}$ , and the aromatic C=C bending was detected at  $1540 \text{ cm}^{-1}$ . In the FT-IR spectrum of the Cu(II)-ImaSMe complex, several shifts in vibrational frequencies were observed, indicating coordination between the ligand and the metal ion. The C=N stretching vibration shifted to  $1606 \text{ cm}^{-1}$ , and the aromatic C–N stretching appeared at  $1292 \text{ cm}^{-1}$ . Additionally, a new band corresponding to the Cu–N bond was observed at  $420 \text{ cm}^{-1}$ . (Baran, 2005)

The S–H stretching vibration was detected at  $2599\text{ cm}^{-1}$ , and the aromatic C=C bending occurred at  $1524\text{ cm}^{-1}$ .

The observed shifts in the vibrational frequencies of the C=N and C–N bonds suggest that the nitrogen atoms of the imine and amine groups are involved in coordination with the Cu(II) ion. The appearance of the Cu–N stretching vibration at  $420\text{ cm}^{-1}$  further confirms the formation of metal–ligand bonds. (Baran, 2005) The minimal change in the S–H stretching frequency suggests that the sulfur atom is not directly coordinating to the metal center. The red shifts in the C=N and C–N stretching frequencies upon complexation are consistent with ligand-to-metal charge transfer (LMCT), indicating a weakening of these bonds due to coordination.

The UV-Vis spectroscopy of the ImaSMe ligand and the Cu(II)-ImaSMe complex was investigated at different concentrations over the wavelength range of 200 to 800 nm, with the results for the Cu(II)-ImaSMe complex shown in Figure 4.12d and those for the ImaSMe ligand in Figure 4.12e. The UV-Vis absorption spectrum of the ImaSMe ligand exhibited prominent bands at 270 nm and 331 nm, corresponding to intense  $\pi \rightarrow \pi^*$  and  $n \rightarrow \pi^*$  transitions, respectively. The extinction coefficients ( $\epsilon$ ) for these bands were calculated to be  $3,828 \pm 111\text{ M}^{-1}\text{ cm}^{-1}$  at 270 nm and  $4,588 \pm 92\text{ M}^{-1}\text{ cm}^{-1}$  at 331 nm.

In contrast, the Cu(II)-ImaSMe complex displayed a characteristic absorption band at 260 nm and 339 nm (Figure 6c), with an extinction coefficient of  $35,348 \pm 1,131\text{ M}^{-1}\text{ cm}^{-1}$  and  $11,156 \pm 1,775\text{ M}^{-1}\text{ cm}^{-1}$ , which can be attributed to ligand-to-metal charge transfer (LMCT) transitions. (Nazeeruddin, Zakeeruddin, and Kalyanasundaram, 1993) The shift in absorption bands upon complexation indicates successful coordination between the ligand and the copper(II) ion. The hypsochromic shift (blue shift) from 270 nm in the free ligand to 260 nm in the complex suggests an increase in the energy gap due to metal coordination. (X.-C. Chen, Tao, Wang, Peng, Huang, and Qian, 2012) Additionally, the bathochromic shift (red shift) to 339 nm of the band at 331 nm in the complex's spectrum implies that the  $n \rightarrow \pi^*$  transitions are involved in bonding with the metal center. (Hernández et al., 2024)

To further understand the electronic properties of the ImaSMe ligand and the Cu(II)-ImaSMe, the HOMO-LUMO energy gaps were calculated using the onset of the absorption edge in the UV-Vis spectra. The energy gap ( $E_g$ ) can be estimated using the equation 5 (Luo et al., 2023)

$$E_g = \frac{hc}{\lambda_{\text{onset}}} \quad (5),$$

where  $h$  is Planck's constant ( $6.626 \times 10^{-34}$  J s),  $c$  is the speed of light ( $3.00 \times 10^8$  m s<sup>-1</sup>), and  $\lambda_{\text{onset}}$  is the wavelength at the absorption in meters.  $\lambda_{\text{onset}}$  is determined by from the intersection of the absorption onset line and the adjusted baseline. (Shafiee, Salleh, and Yahaya, 2011)

Using the UV-Vis spectroscopy to determine the  $\lambda_{\text{onset}}$  values, the  $E_g$  for the ImaSMe ligand and the Cu(II)-ImaSMe complex were determined to be 3.25 eV and 3.05 eV respectively. The decrease in the energy gap upon complexation indicates that the Cu(II) ion stabilizes the lowest unoccupied molecular orbital (LUMO), leading to a reduced gap between the LUMO and the highest occupied molecular orbital (HOMO), facilitating electronic transitions at lower energies.

These spectral changes, along with the calculated extinction coefficients and HOMO-LUMO gaps, provide further evidence for the formation of the Cu(II)-ImaSMe and support the structural conclusions drawn from single-crystal X-ray diffraction and EXAFS analyses. The UV-Vis data corroborate the coordination environment around the copper center and the electronic interactions between the ligand and the metal ion.

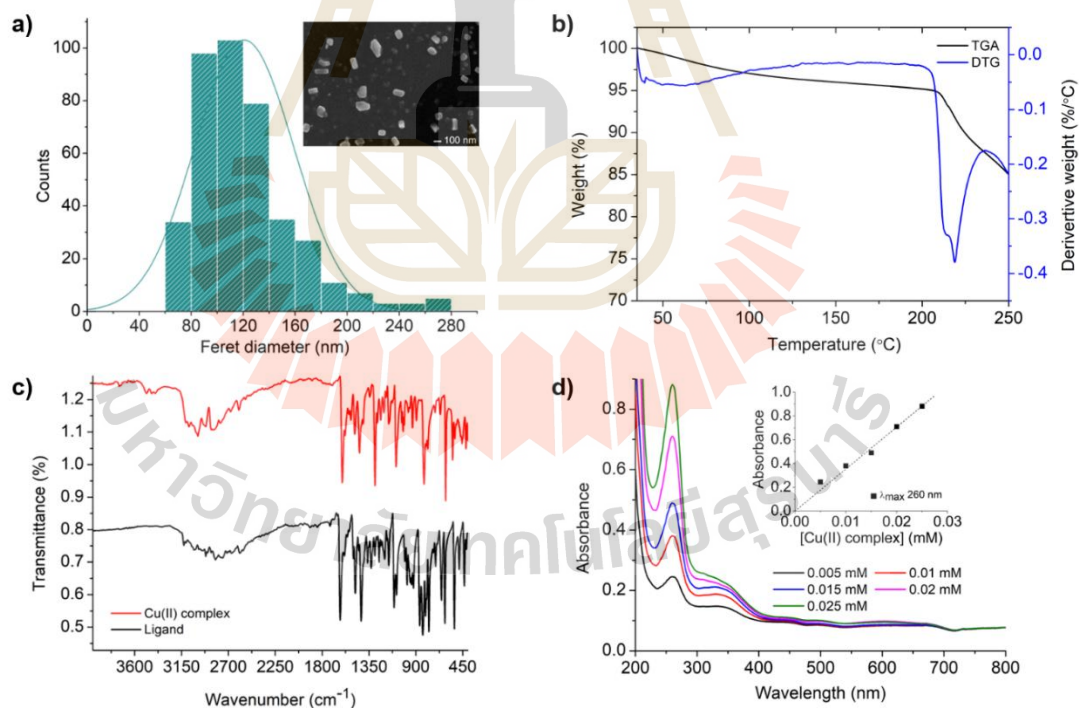


**Figure 4.12** a) SEM image of Cu(II)-ImaSMe. and size distribution from SEM imaging. b) Thermogravimetric analysis (TGA) curve (black line) and Differential Thermogravimetric Analysis (DTG) curve (blue line) of Cu(II)-ImaSMe. c) FT-IR spectra of powder ImaSMe ligand (black line) and Cu(II)-ImaSMe (red line). d) UV-vis spectra of Cu(II)-ImaSMe. e) UV-vis spectra of ImaSMe ligand.

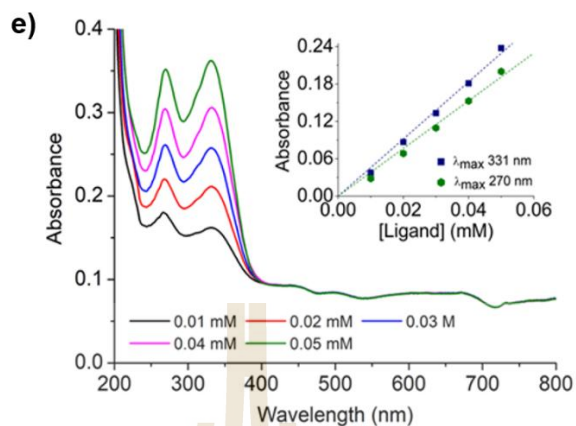


**Figure 4.12** a) SEM image of Cu(II)-ImaSMe. and size distribution from SEM imaging. b) Thermogravimetric analysis (TGA) curve (black line) and Differential Thermogravimetric Analysis (DTG) curve (blue line) of Cu(II)-ImaSMe. c) FT-IR spectra of powder ImaSMe ligand (black line) and Cu(II)-ImaSMe (red line). d) UV-vis spectra of Cu(II)-ImaSMe. e) UV-vis spectra of ImaSMe ligand (Continued).

The electrochemical characterization of the Cu(II)-ImaSMe complex, as depicted in Figure 4.13, was performed using cyclic voltammetry in deoxygenated 96:4 %V/V acetonitrile-water. The experimental setup included a gold working electrode, a platinum wire as the counter electrode, and an Ag/Ag<sup>+</sup> reference electrode. The ferrocene/ferrocenium (Fc/Fc<sup>+</sup>) redox couple was employed as the internal reference, and 0.10 M TBAPF<sub>6</sub> was used as the supporting electrolyte.

The voltammograms for the ImaSMe ligand and its Cu(II) complex, Cu(II)-ImaSMe, are shown in Figure 4.13. For the ImaSMe ligand, the cyclic voltammetry reveals two oxidation peaks at 0.379 V and 1.140 V and three reduction peaks at 0.559 V, -1.159 V, and -1.523 V. In contrast, the Cu(II)-ImaSMe voltammogram displays two oxidation peaks at 0.607 V and 1.275 V, along with two reduction peaks at 0.572 V and -1.191 V. Noteworthy is the similarity in the oxidation peak at 1.140 V for the ImaSMe ligand and 1.275 V for Cu(II)-ImaSMe, as well as the reduction peak at 0.559 V for ImaSMe and 0.607 V for Cu(II)-ImaSMe. Further studies will be performed in comparison with DFT calculation to evaluate and identify these peaks.

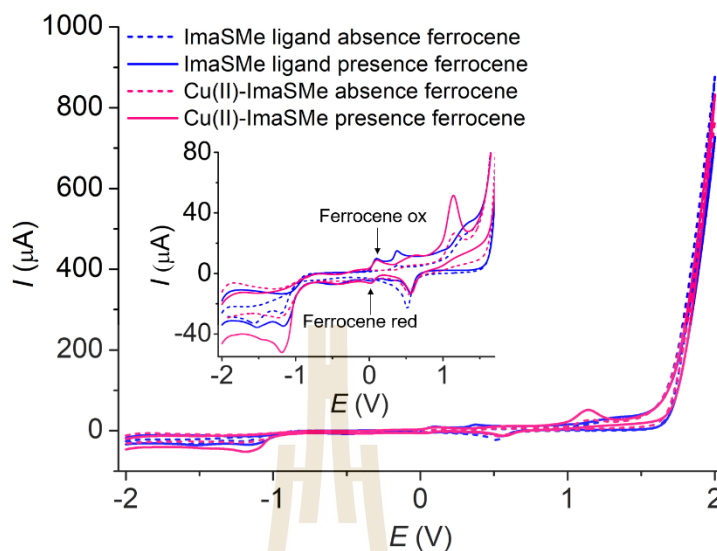


**Figure 4.13** Cyclic voltammograms of 1.0 mM Cu(II)-ImaSMe complex (pink line) and 1.0 mM ImaSMe ligand (blue line) in acetonitrile with 0.10 M TBAPF<sub>6</sub> at a scan rate of 100 mV s<sup>-1</sup>. Solid lines indicate the presence of ferrocene, while dashed lines correspond to the absence of ferrocene.

#### 4.2.2 Electrochemical properties the Cu(II)-ImaSMe complex in aqueous environment

To evaluate the potential of the Cu(II)-ImaSMe complex in electrochemical applications, its electrochemical properties were investigated in an aqueous environment.

##### 4.2.2.1 Charge transfer resistances

Electrochemical impedance spectroscopy (EIS) in 5.0 mM [Fe(CN)<sub>6</sub>]<sup>3-/4-</sup> and 0.10 M KCl aqueous solution was employed to study the charge transfer resistances and to gain insights into the interfacial processes occurring at the Cu(II)-ImaSMe complex when interfaced with a gold electrode. Figure 4.14a illustrates the Nyquist plots of the bare gold electrode, the gold electrode modified with the ImaSMe ligand, and the gold electrode modified with the Cu(II)-ImaSMe complex.

Randle's equivalent circuit (depicted in Figure 4.14a, inlay) was utilized for the analysis of the EIS spectra. where  $R_{ct}$  is the electron transfer resistance,  $C_{dl}$  is the double layer capacitance,  $R_s$  is the resistance of the electrolyte solution, and  $Z_w$  is the Warburg resistance arising from the diffusion process.

The double layer capacitances ( $C_{dl}$ ) were determined to be  $3.29 \times 10^{-7} \pm 0.17 \times 10^{-7}$  F for the bare gold electrode,  $1.48 \times 10^{-7} \pm 0.07 \times 10^{-7}$  F for the gold electrode

modified with ImaSMe ligand, and  $2.67 \times 10^{-7} \pm 0.29 \times 10^{-7}$  F for the gold electrode modified with Cu(II)-ImaSMe complex. The values of  $R_{ct}$  were determined to be  $381 \pm 11 \Omega$  for the bare gold electrode,  $369 \pm 10 \Omega$  for the gold electrode modified with ImaSMe, and  $160 \pm 9 \Omega$  for the gold electrode modified with Cu(II)-ImaSMe, respectively. The  $R_{ct}$  at the ImaSMe modified electrode was lower than that of the unmodified gold surface.

This reduction in resistance can be attributed to the ImaSMe ligand containing imidazole rings and conjugated systems that facilitate electron delocalization. These conjugated systems provide efficient pathways for electron tunneling between the electrode and the redox probe ( $[\text{Fe}(\text{CN})_6]^{3-/4-}$ ), thereby reducing the resistance to electron flow. The  $R_{ct}$  at the Cu(II)-ImaSMe modified electrode was found to be lower than that at both the ImaSMe ligand modified electrode and the bare gold electrode. This indicates that the Cu(II)-ImaSMe enhances electron transfer at the electrode/solution interface more effectively than either the ImaSMe ligand alone or the unmodified gold surface. The presence of redox-active Cu(II) centers within the complex facilitates electron transfer due to their ability to participate in redox processes, thereby further decreasing the charge transfer resistance.

#### 4.2.2.2 Fingerprinting the redox processes

Figure 4.14b presents the cyclic voltammograms of the bare gold electrode (Au), the gold electrode modified with the ImaSMe ligand (ImaSMe/Au), and the gold electrode modified with the Cu(II)-ImaSMe complex (Cu(II)-ImaSMe/Au) in Britton–Robinson buffer (B-R buffer) at pH 2.00 at a scan rate of  $50 \text{ mV s}^{-1}$ . This pH was chosen for the fingerprinting studies as it provides the most well-defined peaks, facilitating clearer interpretation of the electrochemical processes.

The results showed that no voltammetric peaks were observed at the bare gold electrode within the scanned potential range. This absence of peaks indicates that the unmodified gold surface does not exhibit significant electrochemical activity under these conditions. At the ImaSMe/Au electrode, a prominent oxidation peak was observed at 0.70 V, along with a corresponding reduction peak at 0.27 V. These peaks are likely attributed to the redox activity of the imidazole functional group present in the ImaSMe ligand. (Jayabharathi, Sundharesan, Prabhakaran, and Karunakaran, 2015)

For the Cu(II)-ImaSMe/Au electrode, the cyclic voltammogram exhibited three oxidation peaks at potentials of 0.04 V, 0.39 V, and 0.68 V, and corresponding reduction peaks at 0.32 V, -0.31 V, and -0.49 V. The oxidation peak at 0.68 V and the reduction peak at 0.32 V coincide with those observed for the ImaSMe/Au electrode, suggesting

that the imidazole functional group remains electroactive in the Cu(II)-ImaSMe complex. The emergence of the additional peaks at 0.04 V and 0.39 V (oxidation) and  $-0.31$  V and  $-0.49$  V (reduction) exclusively in the complex indicates new electrochemical processes associated with the copper center.

These additional peaks are likely attributed to the redox transitions of the copper ion within the complex and demonstrate that the copper ion in the Cu(II)-ImaSMe complex is electrochemically active. The oxidation peak at 0.39 V and the reduction peak at  $-0.31$  V can be assigned to the Cu(II)/Cu(I) redox couple, representing the reversible oxidation of Cu(I) to Cu(II) and reduction of Cu(II) to Cu(I), respectively. The oxidation peak at 0.04 V and the reduction peak at  $-0.49$  V may correspond to the Cu(I)/Cu(0) redox couple, indicating the possible reduction of Cu(I) to metallic copper and its subsequent oxidation. The shifts in peak potentials compared to standard copper redox potentials suggest that the ligand environment significantly influences the redox behavior of the copper ion, likely due to coordination effects and changes in electron density around the metal center.

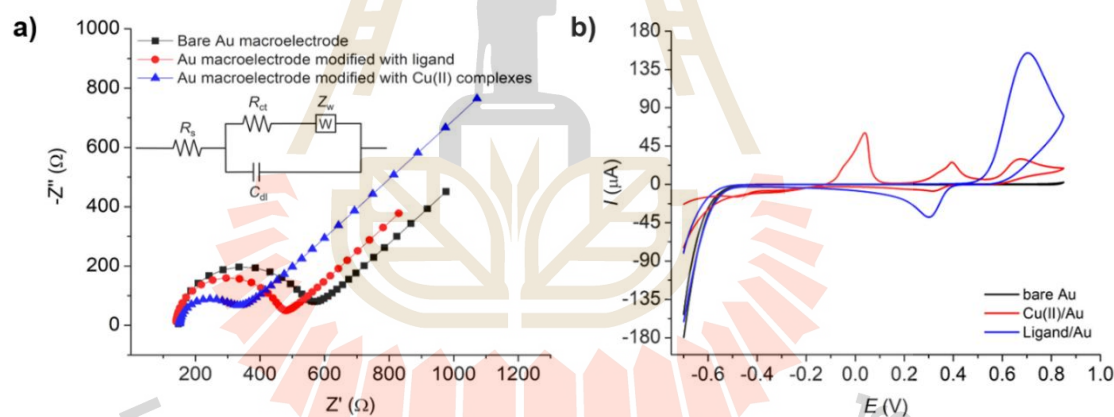


**Figure 4.14** a) EIS spectra of the bare gold electrode, ImaSMe/Au, and Cu(II)-ImaSMe/Au in 5.0 mM  $[\text{Fe}(\text{CN})_6]^{3-/4-}$  and 0.10 M KCl aqueous solution. The inset shows Randle's equivalent circuit used for fitting the EIS data. b) Cyclic voltammograms of Cu(II)-ImaSMe/Au in B-R buffer pH 2.00 aqueous solution at a scan rate of  $50 \text{ mV s}^{-1}$ .

#### 4.2.2.3 Effects of pH

The effect of pH on the voltammetric response of the Cu(II)-ImaSMe/Au electrode was examined over a pH range of 2.00 to 12.00 using Britton–Robinson buffer solutions (Figure 4.15b). The cyclic voltammograms revealed that there was no significant shift in the peak potentials across the pH range studied,

indicating that the redox processes of the Cu(II)-ImaSMe complex are not significantly influenced by protonation or deprotonation events.

However, the intensities of both the oxidation and reduction peaks diminished progressively with increasing pH levels, suggesting that the complex is more stable and electrochemically active in acidic environments.

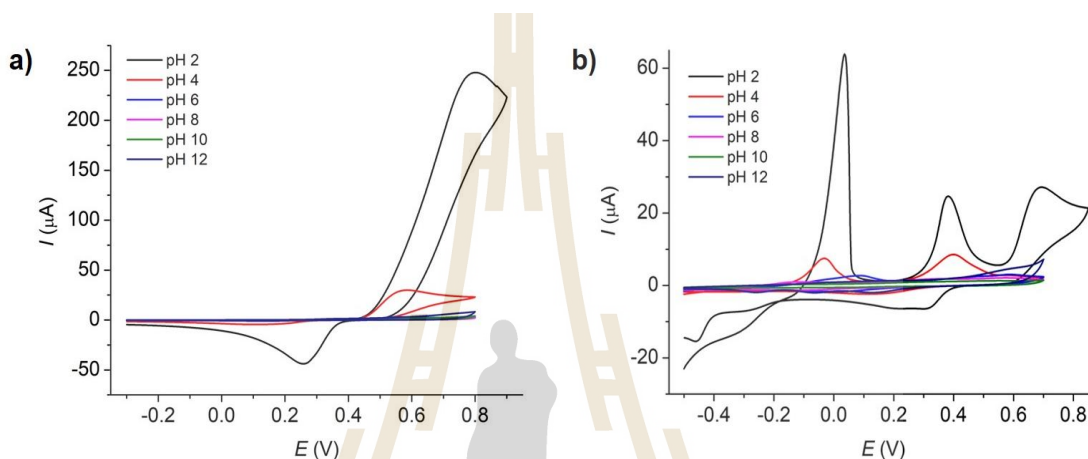


**Figure 4.15** a) Cyclic voltammograms of ImaSMe/Au and b) Cu(II)-ImaSMe/Au electrode in B-R buffer aqueous solution at a scan rate of  $50 \text{ mV s}^{-1}$ . at various pH.

#### 4.2.2.4 Effects of potential scan rates

The influence of scan rates on the electrochemical behavior of the ImaSMe/Au and Cu(II)-ImaSMe/Au electrodes was investigated, as presented in Figure 4.16. For the ImaSMe/Au electrode (Figure 4.16a), the peak currents exhibited a linear relationship with the square root of the scan rate ( $(\sqrt{\nu})$ ), indicating a diffusion-controlled process. In contrast, for the Cu(II)-ImaSMe/Au electrode (Figure 4.16b), the peak currents increased linearly with the scan rate ( $\nu$ ), as shown in the inlay. However, analyzing the final oxidation peak proved challenging because the current from the second peak did not return to the baseline before the onset of the last peak.

This linear relationship suggests that the redox processes are surface-controlled. The linear dependence of peak current on scan rate for a surface-confined redox couple is described by equation 6 (Cui et al., 2015):

$$I_p = n^2 F^2 A \Gamma \nu / (4RT) \quad (6),$$

where  $I_p$  is the peak current,  $n$  is the number of electrons transferred,  $F$  is the Faraday constant ( $96,485 \text{ C mol}^{-1}$ ),  $A$  is the electrode surface area,

$\Gamma$  is the surface coverage of the electroactive species ( $\text{mol cm}^{-2}$ ),  $\nu$  is the scan rate,  $R$  is the gas constant ( $8.314 \text{ J K}^{-1} \text{ mol}^{-1}$ ), and  $T$  is the absolute temperature.

The analysis of kinetic parameters was further evaluated by plotting the peak potentials ( $E_p$ ) against  $\ln(\nu)$ , according to equation 7: (Tang, Zhang, Li, and Zeng, 2014)

$$E_p = E^0 + \frac{RT}{\beta nF} \ln \left( \frac{RTk^0}{\beta nF\nu} \right) \quad (7),$$

where  $E^0$  is the formal potential,  $\beta$  is the anodic transfer coefficient, and  $k^0$  is the standard heterogeneous electron transfer rate constant ( $\text{cm s}^{-1}$ ). The analysis yielded the values of  $\beta$  and  $k^0$  of 0.5 and  $23.64 \text{ cm s}^{-1}$ , respectively.

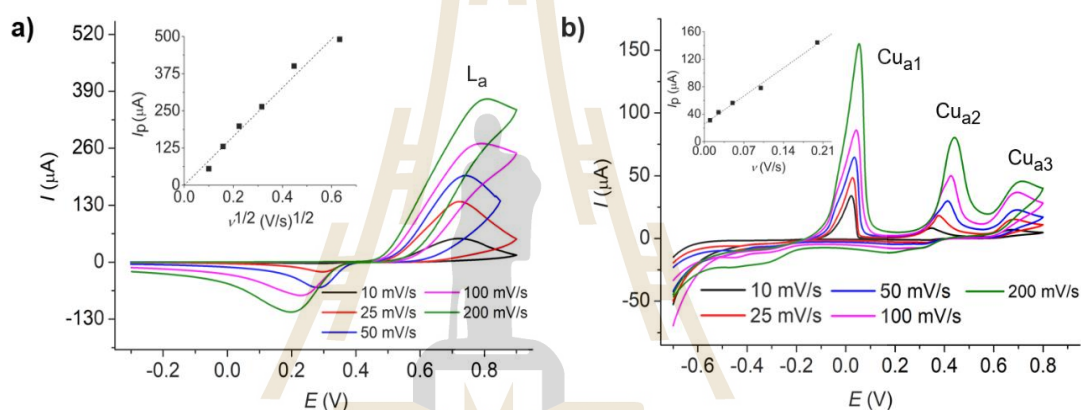


**Figure 4.16** a) Cyclic voltammograms of ImaSMe b) Cu(II)-ImaSMe dropcasted on gold electrode in B-R buffer pH 2.00 aqueous solution at various scan rates.

#### 4.2.2.5 Multiple cycles

Figure 4.17 depicts the multiple cycles of a gold electrode modified with a ImaSMe ligand and a Cu(II)-ImaSMe complex in both B-R buffer at pH 2.00 and 0.10 M KCl solution. In Figure 4.17a, the electrode modified with the ImaSMe ligand is shown under B-R buffer at pH 2.00. It is observed that the first peak oxidation increases with the number of scans, whereas the second oxidation peak and the reduction peak decrease with the number of scans. Conversely, in the case of the electrode modified with the complex (Figure 4.17b), all peaks decrease with the number of scans increase.

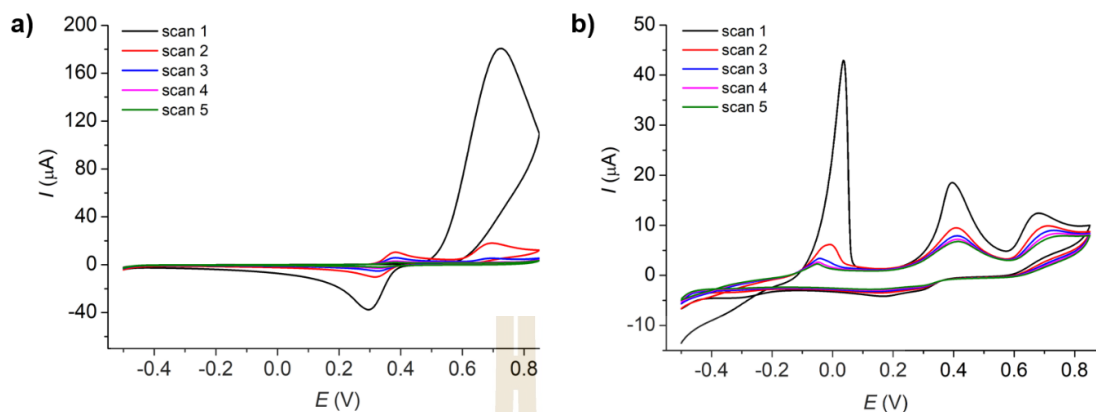


**Figure 4.17** a) Cyclic voltammetry of multiple cycles at ImaSMe/Au and b) Cu(II)-ImaSMe/Au B-R buffer pH 2.00 aqueous solution at a scan rate of  $50 \text{ mV s}^{-1}$ .

### 4.2.3 Application of Cu(II)-ImaSMe in creatinine analysis

The Cu(II)-ImaSMe complex, featuring a five-coordinate geometry, exhibits excellent electroactivity and the capacity to accommodate or exchange additional ligands, making it highly suitable for diverse electrochemical applications. This work demonstrates the effective use of the Cu(II)-ImaSMe complex in the electrochemical analysis of creatinine.

#### 4.2.3.1 Voltammetry of creatinine at Cu(II)-ImaSMe/Au

This acidic pH was initially selected as it yielded the highest and most well-defined peaks for the Cu(II)-ImaSMe complex, facilitating clear identification of electrochemical processes. However, our studies demonstrated that at pH 2.00, there was no significant change in the voltammetric response with varying creatinine concentrations (refer to Figure 4.18). This lack of responsiveness indicates that the acidic environment does not favor the interaction between creatinine and the Cu(II)-ImaSMe complex, limiting the sensor's effectiveness under these conditions.

In contrast, performing the analysis at neutral pH proved advantageous for creatinine detection. (Figure 4.18a) Neutral pH not only supports a more responsive voltammetric behavior in the presence of creatinine (discussed later), but it also aligns closely with physiological conditions, enhancing the relevance of the sensor for biomedical applications. Consequently, to optimize both the sensitivity and practical applicability of the sensor, all subsequent creatinine analyses were conducted at pH 7.00.

No voltammetric peak was observed at the bare Au electrode, indicating that creatinine is electrochemically inert under the tested conditions, refer to Figure 4.19a Similarly, the ImaSMe/Au electrode showed no significant voltammetric

response, suggesting that the ImaSMe ligand alone does not facilitate the electrochemical detection of creatinine. In contrast, a clear oxidation peak was observed at 0.01 V at the Cu(II)-ImaSMe/Au electrode (Figure 4.18a). This prominent peak signifies the effective interaction between creatinine and the Cu(II)-ImaSMe complex. The physical origin behind this phenomenon will be investigated in detail by a combination of electrochemical and *ex-situ* characterization techniques in Section 4.2.1 and 4.2.2.

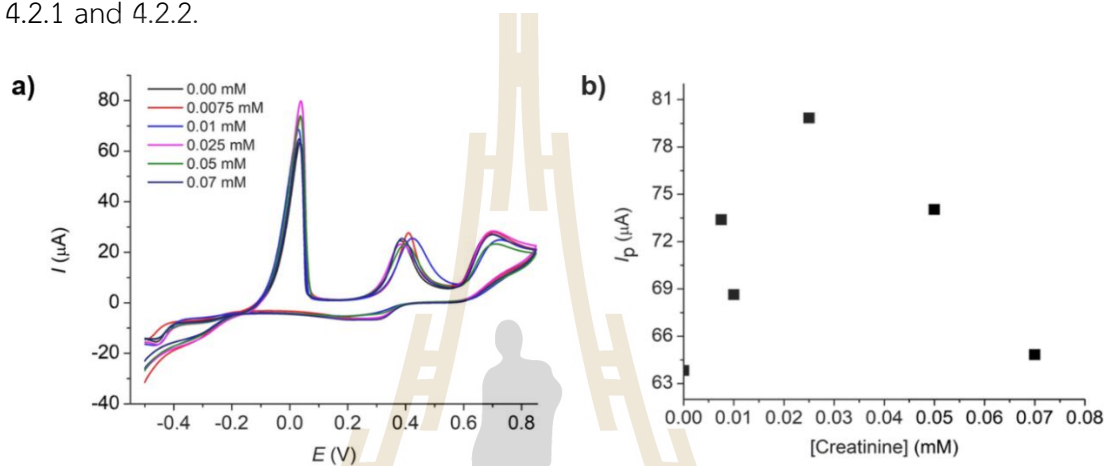


**Figure 4.18** Cyclic voltammograms of Cu(II)-ImaSMe complex dropcasted on gold macroelectrode in various creatinine concentrations in B-R buffer pH 2.0 containing 0.10 M KCl aqueous solution at a scan rate of  $50 \text{ mV s}^{-1}$ .

#### 4.2.3.2 Effects of potential scan rates on creatinine analysis

The effect of scan rate on electrochemical response 10.0 mM creatinine was investigated by cyclic voltammetry and the results are shown in Figure 4.19b. The oxidation peak current demonstrated a linear increase with the scan rates ( $\nu$ , as depicted in the Inlay of Figure 4.19b), suggesting that copper-creatinine oxidation at the gold electrode is governed by a adsorption-controlled process. As the reaction occurs exclusively on the electrode surface, the current is constrained by the adsorption rate of the substance to the electrode. Lower scan rates prolong the scanning duration, leading to heightened consumption of reactants near the electrode surface and consequently resulting in a diminished peak current. Conversely, higher scan rates facilitate a rapid conclusion of the scan, resulting in a heightened peak.

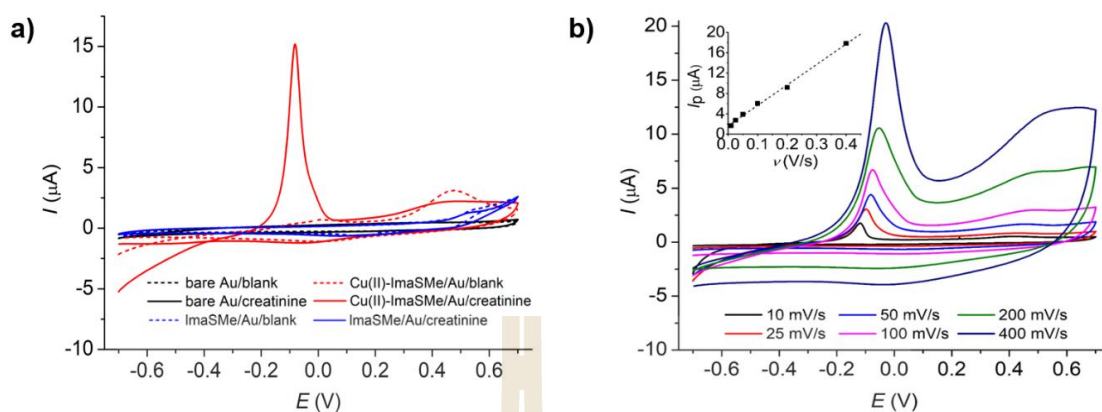


**Figure 4.19** a) Cyclic voltammograms of 20.0 mM creatinine at bare Au electrode modified Au electrode with ImaSMe ligand and Cu(II)-ImaSMe at a scan rate of  $50 \text{ mV s}^{-1}$  b) Cyclic voltammograms of Cu(II)-ImaSMe electrode in 10.0 mM creatinine containing 0.10 M KCl aqueous solution at various scan rates.

#### 4.2.3.3 Calibration plots

Figure 4.20a displays the cyclic voltammograms of the Cu(II)-ImaSMe/Au electrode for various concentrations of creatinine recorded at a scan rate of  $50 \text{ mV s}^{-1}$ . The results demonstrate that the peak currents increase linearly with creatinine concentrations within the range of 0.14 – 20.0 mM. The sensitivity of the method was determined to be  $0.78 \pm 0.01 \mu\text{A mM}^{-1}$ , with a limit of detection of 0.04 mM ( $3s_b/m$ ).

#### 4.2.3.4 Reproducibility and selectivity studies

Voltammetric analyses performed on three Cu(II)-ImaSMe/Au electrodes yielded relative standard deviations (RSD) of 3.13%, 2.23%, and 2.90% ( $n = 3$ ) for creatinine concentrations of 1.0 mM, 10.0 mM, and 15.0 mM, respectively. These results highlight the electrode's reproducibility and consistent performance across varying creatinine concentrations.

The selectivity of the Cu(II)-ImaSMe/Au sensor towards creatinine was evaluated in the presence of potential interferences such as ascorbic acid, uric acid, dopamine, urea, lactate, arginine, and creatine. Experiments were carried out using a fixed creatinine concentration of 10.0 mM, alongside various concentrations of potential interfering species: 10.0 mM ascorbic acid, 0.25 mM uric acid, 2.5 mM dopamine, 250 mM urea, 0.6 mM lactate, 0.1 mM arginine, and 0.1 mM creatine. The concentrations of these interfering substances were chosen based on their typical physiological levels in human urine. (Abellán-Llobregat, González-Gaitán, Vidal, Canals, and Morallon, 2018; Abellán-Llobregat, Vidal, Rodríguez-Amaro, Berenguer-Murcia,

Canals, and Morallón, 2017; Dalirirad and Steckl, 2020; M. I. Khan et al., 2019; L. Liu, Mo, Wei, and Raftery, 2012; Nikolaidis, Kosmidis, Sougioultzis, Kabasakalis, and Mougios, 2018; Thompson and Rechnitz, 1974) The results demonstrated that the Cu(II)-ImaSMe/Au sensor exhibited excellent selectivity for creatinine, with no significant alteration (<5%) in the current response at the peak potential in the presence of the aforementioned interferences, as shown in Figure 4.20b.

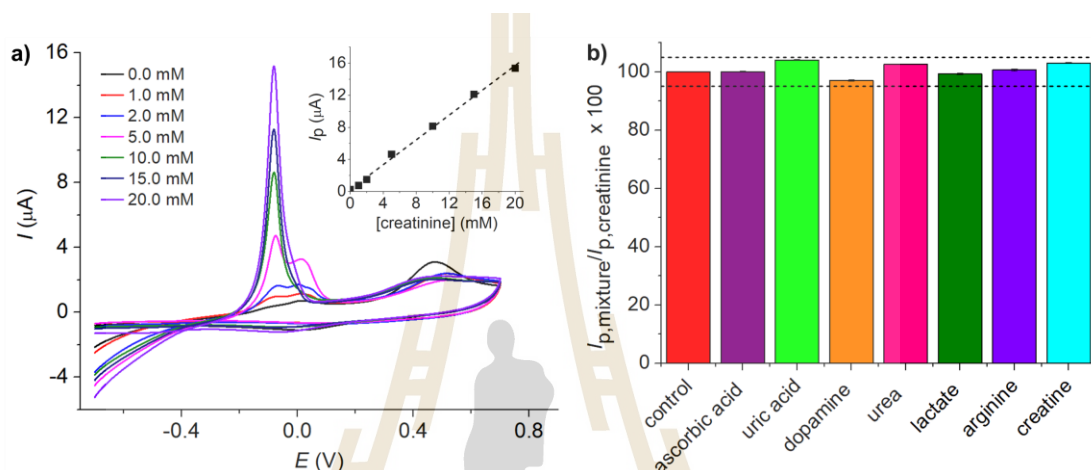


**Figure 4.20** a) CV of various creatinine concentrations containing 0.10 M KCl at Cu(II)-ImaSMe/Au electrode at a scan rate of  $50 \text{ mV s}^{-1}$ . Inlay: Plot of peak currents ( $I_p$ ) vs. creatinine concentrations. b) Peak currents of creatinine at Cu(II)-ImaSMe/Au electrode in the presence and absence of interfering species.

The performance of the developed sensor is compared with that of other existing non-enzymatic electrochemical sensors for creatinine detection, as illustrated in Table 4.3. Key parameters, including sensitivity, linear range, and limit of detection, are analyzed to highlight the advantages of the developed sensor.

**Table 4.3** Comparison of electrochemical sensors for creatinine detection.

Electrode	Method	Linear range (mM)	Limit of detection ( $\mu\text{M}$ )	Ref.
Cu/GC	CV	0–10	35	(Ngamchuea, Wannapaiboon, Nongkhunsan, Hirunsit, and Fongkaew, 2022)
Cu/GC	DPV	0.083–20.0	25	(Jankhunthod, Kaewket, Termsombut, Khamdang, and Ngamchuea, 2023b)

**Table 4.3** Comparison of electrochemical sensors for creatinine detection (Continued).

Electrode	Method	Linear range (mM)	Limit of detection ( $\mu$ M)	Ref.
CuO@MIP/CPE	AMP	0.0005–0.200	0.083	(Nontawong et al., 2019)
Fe <sup>3+</sup> /CB NPs/SPCE	DPV	0.10–6.50	43	(Fava et al., 2020)
MIP/Ni@PANI NPs/MGCE	DPV	0.000004–0.0008	0.2	(Rao et al., 2017)
PAA gel-Cu(II)/Cu <sub>2</sub> O NPs/SPCE	DPV	0.20–100	6.5	(Kalasin, Sangnuang, Khownarumit, Tang, and Surareungchai, 2020)
Pectin-MWCNT/CPE	DPV	0.000016–0.0033	0.6241	(Yazhini, Suja, Bagyalaksmi, and Pavalamalar, 2018)
Pt macrodisc	CV	1.00–10.00	100	(Kaewket and Ngamchuea, 2023)
Pt-MEA	LSV	0.00–5.00	59	(Kaewket and Ngamchuea, 2023)
Cu(II)-ImaSMe/Au	CV	0.14–20.0	40	This work

AMP: amperometry, CB: carbon black, CPE: a carbon-paste electrode, CV: cyclic voltammetry, DPV: differential pulse voltammetry, GC: glassy carbon electrode, ImaSMe: (*E*)-N-((1H-imidazol-4-yl)methylene)-4-(methylthio)aniline, LSV: linear sweep voltammetry, MGCE: modified glassy carbon electrode, MEA: microelectrode arrays, MIP: molecularly-imprinted polymer, NPs: nanoparticles, PAA: polyacrylic acid, PANI: polyaniline, MWCNT: multiwall carbon nanotube, SPCE: screen printed carbon electrode

#### 4.2.3.5 Application to synthetic urine samples

The developed method was applied to the detection of creatinine in synthetic urine, which was prepared in accordance with the protocol outlined by Jiang et al. (Jiang et al., 2016). The synthetic urine composition consisted of 170.0 mM urea, 1.1 mM sodium L-lactate, 2.0 mM citric acid, 25.0 mM, sodium bicarbonate, 90.0 mM sodium chloride, 2.0 mM magnesium sulfate, 10.0 mM sodium sulfate, 7.0 mM sodium phosphate monobasic, 7.0 mM sodium phosphate dibasic, and 25.0 mM

ammonium chloride. Additionally, the synthetic urine sample was supplemented with 20.0 mM creatinine and 0.10 M KCl. To evaluate the sensor's efficacy in real sample analysis, a standard recovery assay was conducted to quantitatively determine the creatinine content in synthetic urine. The recovery rate of creatinine was determined to be  $98.46 \pm 6.56\%$ .

#### 4.2.3.6 Application to real urine samples

The validation of the Cu(II)-ImaSMe/Au sensor was conducted using a urine sample obtained from a cohort of three healthy individuals. subsequently analyzed through voltammetric analyses at the Cu(II)-ImaSMe/Au using a scan rate of  $50 \text{ mV s}^{-1}$ , result as table 4.4. The standard addition method was employed to determine the concentration of creatinine in the spiked sample. The creatinine levels detected using the developed sensor were compared to those obtained via the VITROS CREA assay, performed on an automated analyzer (Vitros® 5600, Ortho-Clinical Diagnostics, USA) in accordance with the standard protocol for creatinine analysis. (Block, Cotten, Franke, and Mbughuni, 2022; De Silva, Halstead, Côté, Sabr, von Dadelszen, and Magee, 2013; Olayinka, Garnett, Burnett, and Devaraj, 2023) In this method, the urine sample is applied to a multilayered slide, where creatinine undergoes hydrolysis to form creatine. The creatine is subsequently converted into sarcosine and urea. Sarcosine is then oxidized, resulting in the formation of formaldehyde, hydrogen peroxide, and glycine. A peroxidase-catalyzed reaction follows, producing a colored compound whose intensity is measured at 670 nm at two specific time points. (Block, Cotten, Franke, and Mbughuni, 2022; De Silva, Halstead, Côté, Sabr, von Dadelszen, and Magee, 2013; Olayinka, Garnett, Burnett, and Devaraj, 2023)

**Table 4.4** Comparison of the Cu(II)-ImaSMe/Au sensor and Jaffe method for creatinine measurement in urine samples.

Sample	Creatinine concentration (mM)		% Recovery *	%RSD **
	Jaffe method	Cu(II)-ImaSMe/Au sensor		
1	1.48	1.44	97.3	1.59
2	2.04	2.05	100.5	6.25
3	2.67	2.60	97.4	7.31

\* % Recovery = (our sensor value / Jaffe Method value) x100%

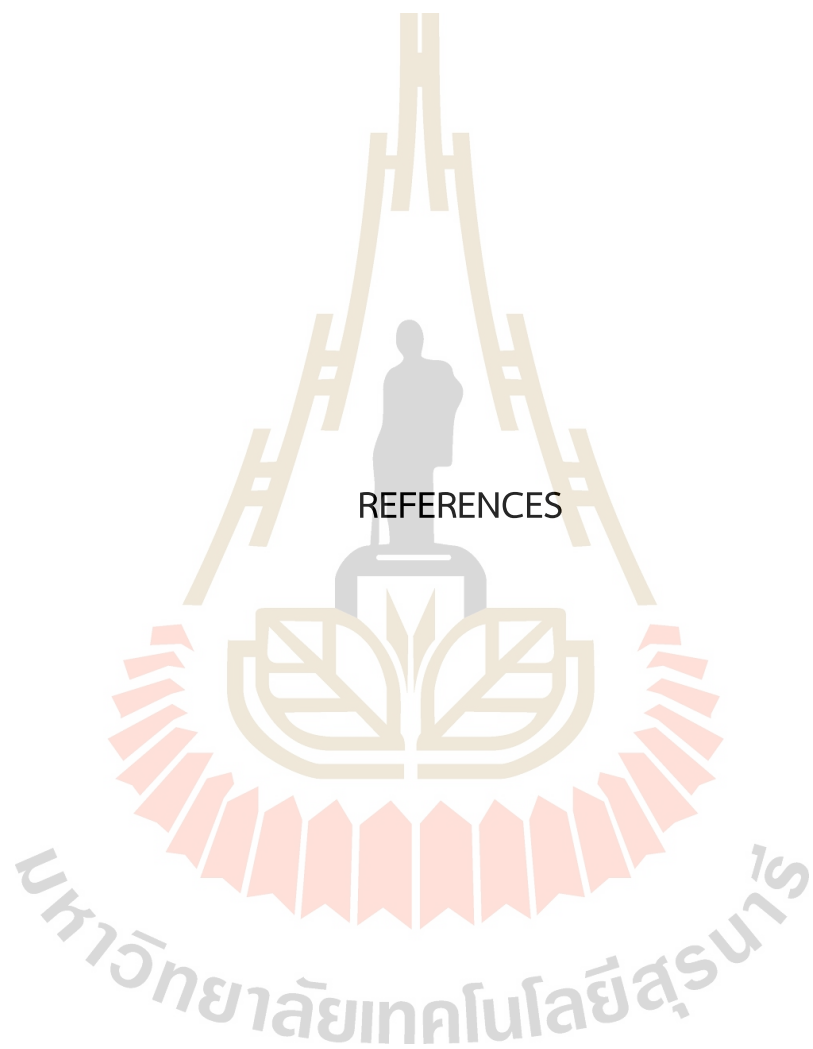
\*\* %RSD of the Cu(II)-ImaSMe/Au sensor

## CHAPTER V

### CONCLUSION

This work provides insights into two significant advancements in electrochemical sensing: the oxidation mechanism of guanosine and the development of a Cu(II)-ImaSMe complex for creatinine detection. The oxidation of guanosine was systematically studied using DFT calculations and cyclic voltammetry on stationary and rotating electrodes at both macro- and microscales. The results revealed a multi-step process, starting with an electrochemically irreversible  $1\text{H}^+ 1\text{e}^-$  reaction, followed by hydrolysis, electron transfer, and the formation of 8-hydroxyguanosine and a radical species. This radical readily dimerizes into an electrochemically inert product that deposits on the electrode surface. These findings contribute to a deeper understanding of guanosine oxidation, paving the way for advancements in guanosine analysis and its applications in biological and biomedical contexts.

Simultaneously, a novel Cu(II)-ImaSMe complex was synthesized and thoroughly characterized, revealing a well-defined crystalline structure, uniform particle distribution, and functional groups essential for its electrochemical behavior. This complex was successfully modified on a gold macroelectrode for the sensitive and selective detection of creatinine, even in the presence of interferences. The sensor demonstrated excellent performance in urine sample analysis, offering a rapid and straightforward approach for clinical diagnostics, particularly in kidney function monitoring. Together, these studies highlight critical innovations in electrochemical sensing, providing robust platforms for biomedical and clinical applications.



## REFERENCES

- Abellán-Llobregat, A., González-Gaitán, C., Vidal, L., Canals, A., and Morallon, E. (2018). Portable Electrochemical Sensor Based on 4-Aminobenzoic Acid-Functionalized Herringbone Carbon Nanotubes for the Determination of Ascorbic Acid and Uric Acid in Human Fluids. *Biosensors and Bioelectronics*, *109*, 123-131.
- Abellán-Llobregat, A., Vidal, L., Rodríguez-Amaro, R., Berenguer-Murcia, Á., Canals, A., and Morallón, E. (2017). Au-Iridium Microelectrodes Modified with Au-Doped Graphene Oxide for the Simultaneous Determination of Uric Acid and Ascorbic Acid in Urine Samples. *Electrochimica acta*, *227*, 275-284.
- Addison, A. W., Rao, T. N., Reedijk, J., van Rijn, J., and Verschoor, G. C. (1984). Synthesis, Structure, and Spectroscopic Properties of Copper (II) Compounds Containing Nitrogen-Sulphur Donor Ligands; the Crystal and Molecular Structure of Aqua [1, 7-Bis (N-Methylbenzimidazol-2'-yl)-2, 6-Dithiaheptane] Copper (II) Perchlorate. *Journal of the Chemical Society, Dalton Transactions*(7), 1349-1356.
- Ahlrichs, R., Bär, M., Häser, M., Horn, H. W., and Kölmel, C. M. (1989). Electronic Structure Calculations on Workstation Computers: The Program System Turbomole. *Chemical Physics Letters*, *162*, 165-169.
- Andreev, E., Koopman, M., and Arisz, L. (1999). A Rise in Plasma Creatinine That Is Not a Sign of Renal Failure: Which Drugs Can Be Responsible? *Journal of internal medicine*, *246*(3), 247-252.
- Babamiri, B., Salimi, A., Hallaj, R., and Hasanzadeh, M. (2018). Nickel Nanoclusters as a Novel Emitter for Molecularly Imprinted Electrochemiluminescence Based Sensor toward Nanomolar Detection of Creatinine. *Biosensors and Bioelectronics*, *107*, 272-279.
- Bandopadhyay, N., Paramanik, K., Mudi, P. K., Sarkar, G., Kotakonda, M., Shit, M., Biswas, B., and Das, H. S. (2022). A Thiomethyl-Substituted Imidazolyl Imine Functionalized Copper (II) Complex: Synthesis, Structural Characterization, Phenoxazinone Synthase Mimics and Biological Activities. *Polyhedron*, *218*, 115783.
- Baran, E. J. (2005). Structural Data and Vibrational Spectra of the Copper (II) Complex of L-Selenomethionine. *Zeitschrift für Naturforschung B*, *60*(6), 663-666.

- Batchelor-McAuley, C., and Compton, R. G. (2012). Voltammetry of Multi-Electron Electrode Processes of Organic Species. *Journal of Electroanalytical Chemistry*, 669, 73-81.
- Bauer, C., Melamed, M. L., and Hostetter, T. H. (2008). Staging of Chronic Kidney Disease: Time for a Course Correction. *Journal of the American Society of Nephrology*, 19(5), 844-846.
- Block, D. R., Cotten, S. W., Franke, D., and Mbughuni, M. M. (2022). Comparison of Five Common Analyzers in the Measurement of Chemistry Analytes in an Authentic Cohort of Body Fluid Specimens. *American Journal of Clinical Pathology*, 158(1), 47-61.
- Bolin, C., and Cardozo-Pelaez, F. (2007). Assessing Biomarkers of Oxidative Stress: Analysis of Guanosine and Oxidized Guanosine Nucleotide Triphosphates by High Performance Liquid Chromatography with Electrochemical Detection. *Journal of Chromatography B*, 856(1-2), 121-130.
- Chang, C.-N., Cheng, H.-B., and Chao, A. C. (2004). Applying the Nernst Equation to Simulate Redox Potential Variations for Biological Nitrification and Denitrification Processes. *Environmental science & technology*, 38(6), 1807-1812.
- Chen, D., Gan, C., Fan, X., Zhang, L., Li, W., Zhu, M., and Quan, X. (2019). Improving the Dynamic Mechanical Properties of Xnbr Using IIs/Kh550-Functionalized Multilayer Graphene. *Materials*, 12(17), 2800.
- Chen, X.-C., Tao, T., Wang, Y.-G., Peng, Y.-X., Huang, W., and Qian, H.-F. (2012). Azo-Hydrazone Tautomerism Observed from Uv-Vis Spectra by Ph Control and Metal-Ion Complexation for Two Heterocyclic Disperse Yellow Dyes. *Dalton Transactions*, 41(36), 11107-11115.
- Chhillar, M., Kukkar, D., Deep, A., Yadav, A. K., and Kim, K.-H. (2023). Zn<sup>2+</sup>/Gnps Nanocomposite for Highly Selective Colorimetric Detection of Creatinine in Urine Samples of Ckd Patients. *Inorganic Chemistry Communications*, 158, 111618.
- Chiorcea-Paquim, A.-M., and Oliveira-Brett, A. M. (2021). Nanostructured Material-Based Electrochemical Sensing of Oxidative DNA Damage Biomarkers 8-Oxoguanine and 8-Oxodeoxyguanosine: A Comprehensive Review. *Microchimica Acta*, 188, 1-13.
- Choi, K. C., Lee, J., Kim, S. W., Kim, N. H., Moon, K. H., Park, K. K., Bom, H. S., and Kang, Y. J. (1993). Cimetidine Improves the Accuracy of Creatinine Clearance as an Indicator for Glomerular Filtration Rate. *The Korean Journal of Internal Medicine*, 8(1), 28.

- Cooke, M. S., Evans, M. D., Dizdaroglu, M., and Lunec, J. (2003). Oxidative DNA Damage: Mechanisms, Mutation, and Disease. *The FASEB Journal*, 17(10), 1195-1214.
- Corder, C. J., Rathi, B. M., Sharif, S., and Leslie, S. W. (2018). 24-Hour Urine Collection. Core Laboratory at Abbott. (2018). Alinity c Creatinine (Enzymatic) Reagent Kit.
- Cui, X., Guo, W., Zhou, M., Yang, Y., Li, Y., Xiao, P., Zhang, Y., and Zhang, X. (2015). Promoting Effect of Co in Ni M Co N (M+ N= 4) Bimetallic Electrocatalysts for Methanol Oxidation Reaction. *ACS applied materials & interfaces*, 7(1), 493-503.
- Cywinski, P. J., Moro, A. J., Ritschel, T., Hildebrandt, N., and Löhmannsröben, H.-G. (2011). Sensitive and Selective Fluorescence Detection of Guanosine Nucleotides by Nanoparticles Conjugated with a Naphthyridine Receptor. *Analytical and Bioanalytical Chemistry*, 399, 1215-1222.
- Dalirirad, S., and Steckl, A. J. (2020). Lateral Flow Assay Using Aptamer-Based Sensing for on-Site Detection of Dopamine in Urine. *Analytical biochemistry*, 596, 113637.
- Dasgupta, P., Kumar, V., Krishnaswamy, P. R., and Bhat, N. (2020). Serum Creatinine Electrochemical Biosensor on Printed Electrodes Using Monoenzymatic Pathway to 1-Methylhydantoin Detection. *ACS omega*, 5(35), 22459-22464.
- Dash, A. K., and Sawhney, A. (2002). A Simple Lc Method with Uv Detection for the Analysis of Creatine and Creatinine and Its Application to Several Creatine Formulations. *Journal of Pharmaceutical and Biomedical Analysis*, 29(5), 939-945.
- de-los-Santos-Álvarez, N., de-los-Santos-Alvarez, P., Lobo-Castañón, M. J., López, R., Miranda-Ordieres, A. J., and Tuñón-Blanco, P. (2007). Electrochemical Oxidation of Guanosine and Adenosine: Two Convergent Pathways. *Electrochemistry communications*, 9(8), 1862-1866.
- De Silva, D. A., Halstead, A. C., Côté, A.-M., Sabr, Y., von Dadelszen, P., and Magee, L. A. (2013). Random Urine Albumin: Creatinine Ratio in High-Risk Pregnancy—Is It Clinically Useful? *Pregnancy Hypertension: An International Journal of Women's Cardiovascular Health*, 3(2), 112-114.
- Delanaye, P., Cavalier, E., and Pottel, H. (2017). Serum Creatinine: Not So Simple! *Nephron*, 136(4), 302-308.
- DeVananD, V., and Chithrapavai, S. (2013). Correlation of 2 Hours and 24 Hours Creatinine Clearance in Renal Donors after Unilateral Nephrectomy. *Journal of clinical and diagnostic research: JCDR*, 7(10), 2119.

- Dickinson, E. J., Limon-Petersen, J. G., Rees, N. V., and Compton, R. G. (2009). How Much Supporting Electrolyte Is Required to Make a Cyclic Voltammetry Experiment Quantitatively “Diffusional”? A Theoretical and Experimental Investigation. *The Journal of Physical Chemistry C*, 113(25), 11157-11171.
- Ebere, E. C., and Ngozi, V. E. (2019). Microplastics, an Emerging Concern: A Review of Analytical Techniques for Detecting and Quantifying Microplastics. *Analytical methods in environmental chemistry journal*, 2(2), 13-30.
- Faramarzi, B., Moggio, M., Diano, N., Portaccio, M., and Lepore, M. (2023). A Brief Review of Ft-Ir Spectroscopy Studies of Sphingolipids in Human Cells. *Biophysica*, 3(1), 158-180.
- Fava, E. L., do Prado, T. M., Garcia-Filho, A., Silva, T. A., Cincotto, F. H., de Moraes, F. C., Faria, R. C., and Fatibello-Filho, O. (2020). Non-Enzymatic Electrochemical Determination of Creatinine Using a Novel Screen-Printed Microcell. *Talanta*, 207, 120277.
- Festa, R. A., and Thiele, D. J. (2011). Copper: An Essential Metal in Biology. *Current Biology*, 21(21), R877-R883.
- Gao, H., Duan, Y., Xi, M., and Sun, W. (2011). Voltammetric Detection of Guanosine and Adenosine Using a Carbon Paste Electrode Modified with 1-Ethyl-3-Methylimidazolium Ethylsulfate. *Microchimica Acta*, 172, 57-64.
- Gao, X., Gui, R., Guo, H., Wang, Z., and Liu, Q. (2019). Creatinine-Induced Specific Signal Responses and Enzymeless Ratiometric Electrochemical Detection Based on Copper Nanoparticles Electrodeposited on Reduced Graphene Oxide-Based Hybrids. *Sensors and Actuators B: Chemical*, 285, 201-208.
- Gaur, A., Shrivastava, B., and Joshi, S. (2009). *Copper K-Edge Xanes of Cu (I) and Cu (II) Oxide Mixtures*. Paper presented at the Journal of Physics: Conference Series.
- Ge, M., Li, X., Zhang, M., and Liu, Z. (2022). Enhanced Photocatalytic Degradation Performance of Antibiotics Using Magadiite-Supported Carbon Nitride under Visible Light Irradiation. *Journal of Inorganic and Organometallic Polymers and Materials*, 1-9.
- Giuliani, P., Romano, S., Ballerini, P., Ciccarelli, R., Petragani, N., Cicchitti, S., Zuccarini, M., Jiang, S., Rathbone, M., and Caciagli, F. (2012). Protective Activity of Guanosine in an in Vitro Model of Parkinson's Disease. *Panminerva medica*, 54(1 Suppl 4), 43-51.
- Gonzalez-Gallardo, C. L., Arjona, N., Álvarez-Contreras, L., and Guerra-Balcázar, M. (2022). Electrochemical Creatinine Detection for Advanced Point-of-Care Sensing Devices: A Review. *RSC Advances*, 12(47), 30785-30802.

- González-Fernández, E., de-los-Santos-Álvarez, N., Lobo-Castañón, M. J., Miranda-Ordieres, A. J., and Tuñón-Blanco, P. (2008). Electrochemical Oxidation of Guanosine and Xanthosine at Physiological Ph: Further Evidences of a Convergent Mechanism for the Oxidation of Purine Nucleosides. *Electroanalysis: An International Journal Devoted to Fundamental and Practical Aspects of Electroanalysis*, 20(8), 833-839.
- Goyal, R., and Dryhurst, G. (1982). Redox Chemistry of Guanine and 8-Oxyguanine and a Comparison of the Peroxidase-Catalyzed and Electrochemical Oxidation of 8-Oxyguanine. *Journal of electroanalytical chemistry and interfacial electrochemistry*, 135(1), 75-91.
- Goyal, R. N., Gupta, V. K., Oyama, M., and Bachheti, N. (2007). Voltammetric Determination of Adenosine and Guanosine Using Fullerene-C60-Modified Glassy Carbon Electrode. *Talanta*, 71(3), 1110-1117.
- Goyal, R. N., Jain, N., and Garg, D. K. (1997). Electrochemical and Enzymic Oxidation of Guanosine and 8-Hydroxyguanosine and the Effects of Oxidation Products in Mice. *Bioelectrochemistry and bioenergetics*, 43(1), 105-114.
- Goyal, R. N., Oyama, M., and Tyagi, A. (2007). Simultaneous Determination of Guanosine and Guanosine-5'-Triphosphate in Biological Sample Using Gold Nanoparticles Modified Indium Tin Oxide Electrode. *Analytica chimica acta*, 581(1), 32-36.
- Goyal, R. N., Puri, B. K., and Jain, N. (2001). Electrochemical Oxidation of Guanosine-5'-Monophosphate at the Pyrolytic Graphite Electrode. *Journal of the Chemical Society, Perkin Transactions 2*(5), 832-837.
- Grossi, M., and Riccò, B. (2017). Electrical Impedance Spectroscopy (Eis) for Biological Analysis and Food Characterization: A Review. *Journal of sensors and sensor systems*, 6(2), 303-325.
- Gupta, A., and Lutsenko, S. (2009). Human Copper Transporters: Mechanism, Role in Human Diseases and Therapeutic Potential. *Future medicinal chemistry*, 1(6), 1125-1142.
- Hanif, S., John, P., Gao, W., Saqib, M., Qi, L., and Xu, G. (2016). Chemiluminescence of Creatinine/H<sub>2</sub>O<sub>2</sub>/Co<sup>2+</sup> and Its Application for Selective Creatinine Detection. *Biosensors and Bioelectronics*, 75, 347-351.
- Hathaway, B., and Billing, D. (1970). The Electronic Properties and Stereochemistry of Mono-Nuclear Complexes of the Copper (II) Ion. *Coordination Chemistry Reviews*, 5(2), 143-207.

- Ház, A., Jablonský, M., Orságová, A., and Šurina, I. (2013). *Determination of Temperature Regions in Thermal Degradation of Lignin*. Paper presented at the Proceedings of the 4 th International Conference on Renewable Energy Sources, Tatranské Matliare, Slovakia.
- Hernández, J. G., Aguilar, C. A. H., Narayanan, J., Flores, E. D. T., Thangarasu, P., Ramírez, A. H., Shanmugam, K., and Martinez, M. M. L. (2024). Effect of Metal Ions in the Electron-Transfer Mechanism on the Photovoltaic Performance of Salphen-Based Dssc: Experimental and Theoretical Studies. *Materials Advances*, 5(8), 3257-3280.
- Hertwig, R. H., and Koch, W. (1997). On the Parameterization of the Local Correlation Functional. What Is Becke-3-Lyp? *Chemical Physics Letters*, 268(5), 345-35
- Hesse, A., Classen, A., Knoll, M., Timmermann, F., and Vahlensieck, W. (1986). Dependence of Urine Composition on the Age and Sex of Healthy Subjects. *Clinica chimica acta*, 160(2), 79-86.
- Hewavitharana, A., and Bruce, H. (2003). Simultaneous Determination of Creatinine and Pseudouridine Concentrations in Bovine Plasma by Reversed-Phase Liquid Chromatography with Photodiode Array Detection. *Journal of Chromatography B*, 784(2), 275-281.
- Hsu, C.-C., Wang, H., Hsu, Y.-H., Chuang, S.-Y., Huang, Y.-W., Chang, Y.-K., Liu, J.-S., Hsiung, C. A., and Tsai, H.-J. (2015). Use of Nonsteroidal Anti-Inflammatory Drugs and Risk of Chronic Kidney Disease in Subjects with Hypertension: Nationwide Longitudinal Cohort Study. *Hypertension*, 66(3), 524-533.
- Huang, Y.-J., Wang, H. P., and Lee, J.-F. (2003). Catalytic Reduction of No on Copper/Mcm-41 Studied by in Situ Exafs and Xanes. *Chemosphere*, 50(8), 1035-1041.
- Inkson, B. J. (2016). Scanning Electron Microscopy (Sem) and Transmission Electron Microscopy (Tem) for Materials Characterization. In *Materials Characterization Using Nondestructive Evaluation (Nde) Methods* (pp. 17-43): Elsevier.
- Jakob, G., Mair, J., Vorderwinkler, K.-P., Judmaier, G., König, P., Zwierzina, H., Pichler, M., and Puschendorf, B. (1994). Clinical Significance of Urinary Cyclic Guanosine Monophosphate in Diagnosis of Heart Failure. *Clinical chemistry*, 40(1), 96-100.
- Jankhunthod, S., Kaewket, K., Termsombut, P., Khamdang, C., and Ngamchuea, K. (2023a). Electrodeposited Copper Nanoparticles for Creatinine Detection Via the in Situ Formation of Copper-Creatinine Complexes. *Analytical and Bioanalytical Chemistry*, 415(16), 3231-3242.

- Jankhunthod, S., Kaewket, K., Termsombut, P., Khamdang, C., and Ngamchuea, K. (2023b). Electrodeposited Copper Nanoparticles for Creatinine Detection Via the in Situ Formation of Copper-Creatinine Complexes. *Analytical and Bioanalytical Chemistry*, 1-12.
- Jayabharathi, J., Sundharesan, M., Prabhakaran, A., and Karunakaran, C. (2015). Understanding the Binding Interaction of Imidazole with ZnO Nanomaterials and Clusters. *RSC Advances*, 5(13), 9518-9531.
- Jen, J.-F., Hsiao, S.-L., and Liu, K.-H. (2002). Simultaneous Determination of Uric Acid and Creatinine in Urine by an Eco-Friendly Solvent-Free High Performance Liquid Chromatographic Method. *Talanta*, 58(4), 711-717.
- Jiang, G., Wang, J., Yang, Y., Zhang, G., Liu, Y., Lin, H., Zhang, G., Li, Y., and Fan, X. (2016). Fluorescent Turn-on Sensing of Bacterial Lipopolysaccharide in Artificial Urine Sample with Sensitivity Down to Nanomolar by Tetraphenylethylene Based Aggregation Induced Emission Molecule. *Biosensors and Bioelectronics*, 85, 62-67.
- Kaewket, K., and Ngamchuea, K. (2023). Electrochemical Detection of Creatinine: Exploiting Copper (II) Complexes at Pt Microelectrode Arrays. *RSC Advances*, 13(47), 33210-33220.
- Kai, M., Ohkura, Y., Yonekura, S., and Iwasaki, M. (1988). Selective Determination of Guanine and Its Nucleosides and Nucleotides by Reaction with Phenylglyoxal as a Fluorogenic Reagent. *Analytica chimica acta*, 207, 243-249.
- Kalasin, S., Sangnuang, P., Khownarumit, P., Tang, I. M., and Surareungchai, W. (2020). Evidence of Cu (I) Coupling with Creatinine Using Cuprous Nanoparticles Encapsulated with Polyacrylic Acid Gel-Cu (II) in Facilitating the Determination of Advanced Kidney Dysfunctions. *ACS Biomaterials Science & Engineering*, 6(2), 1247-1258.
- Kashani, K., Rosner, M. H., and Ostermann, M. (2020). Creatinine: From Physiology to Clinical Application. *European journal of internal medicine*, 72, 9-14.
- Kastrup, J., Petersen, P., Bartram, R., and Hansen, J. (1985). The Effect of Trimethoprim on Serum Creatinine. *British journal of urology*, 57(3), 265-268.
- Khan, A., Fayyaz, O., Shakoor, R., and Mansoor, B. (2022). Recent Trends in Applications of X-Ray Photoelectron Spectroscopy (Xps) Technique in Coatings for Corrosion Protection. *Recent Developments in Analytical Techniques for Corrosion Research*, 167-186.

- Khan, M. I., Zhang, Q., Wang, Y., Saud, S., Liu, W., Liu, S., Kong, H., Wang, C., Uzzaman, A., and Xiao, H. (2019). Portable Electrophoresis Titration Chip Model for Sensing of Uric Acid in Urine and Blood by Moving Reaction Boundary. *Sensors and Actuators B: Chemical*, 286, 9-15.
- Klamt, A., and Schüürmann, G. (1993). Cosmo: A New Approach to Dielectric Screening in Solvents with Explicit Expressions for the Screening Energy and Its Gradient. *Journal of the Chemical Society, Perkin Transactions 2*(5), 799-805.
- Kohn, W., and Sham, L. J. (1965). Self-Consistent Equations Including Exchange and Correlation Effects. *Physical Review*, 140(4A), A1133-A1138.
- Kossmann, S., and Neese, F. (2009). Comparison of Two Efficient Approximate Hartee-Fock Approaches. *Chemical Physics Letters*, 481(4-6), 240-243.
- Krstulovic, A. M., Brown, P. R., and Rosie, D. M. (1977). Identification of Nucleosides and Bases in Serum and Plasma Samples by Reverse-Phase High Performance Liquid Chromatography. *Analytical Chemistry*, 49(14), 2237-2241.
- Kumar, D. R., Manoj, D., and Santhanalakshmi, J. (2013). Optimization of Site Specific Adsorption of Oleylamine Capped CuO Nanoparticles on Mwcnts for Electrochemical Determination of Guanosine. *Sensors and Actuators B: Chemical*, 188, 603-612.
- Kumar, R. R., Shaikh, M. O., and Chuang, C.-H. (2021). A Review of Recent Advances in Non-Enzymatic Electrochemical Creatinine Biosensing. *Analytica chimica acta*, 1183, 338748.
- Kumar, V., Hebbar, S., Kalam, R., Panwar, S., Prasad, S., Srikanta, S., Krishnaswamy, P., and Bhat, N. (2017). Creatinine-Iron Complex and Its Use in Electrochemical Measurement of Urine Creatinine. *IEEE Sensors Journal*, 18(2), 830-836.
- Kushwaha, K. S., Anand, A., Dey, B., Ahmad, M. W., Syed, A., AL-Shwaiman, H. A., Subramaniam, M., and Choudhury, A. (2024). Novel Electrochemical Sensing Platform Based on Zinc Metal Organic Frameworks/Carbon Nanofiber Nanocomposite for Detection of Creatinine in Human Urine. *Journal of Electroanalytical Chemistry*, 971, 118574.
- Kvasnicová, V. r., Samcová, E., Jursová, A., and Jelínek, I. (2003). Determination of 8-Hydroxy-2'-Deoxyguanosine in Untreated Urine by Capillary Electrophoresis with Uv Detection. *Journal of Chromatography A*, 985(1-2), 513-517.
- Lanznaster, D., Dal-Cim, T., Piermartiri, T. C., and Tasca, C. I. (2016). Guanosine: A Neuromodulator with Therapeutic Potential in Brain Disorders. *Aging and disease*, 7(5), 657.

- Li, J.-X., Wang, J.-L., Chai, T.-Q., and Yang, F.-Q. (2023). One-Pot Synthesized Copper-Imidazole-2-Carboxaldehyde Complex Material with Oxidase-Like Activity for the Colorimetric Detection of Glutathione and Ascorbic Acid. *Heliyon*, 9(11).
- Lin, Y.-H., Wang, S.-H., Wu, M.-H., Pan, T.-M., Lai, C.-S., Luo, J.-D., and Chiou, C.-C. (2013). Integrating Solid-State Sensor and Microfluidic Devices for Glucose, Urea and Creatinine Detection Based on Enzyme-Carrying Alginate Microbeads. *Biosensors and Bioelectronics*, 43, 328-335.
- Liu, J., Jiang, X., Zhang, R., Zhang, Y., Wu, L., Lu, W., Li, J., Li, Y., and Zhang, H. (2019). Mxene-Enabled Electrochemical Microfluidic Biosensor: Applications toward Multicomponent Continuous Monitoring in Whole Blood. *Advanced Functional Materials*, 29(6), 1807326.
- Liu, L., Mo, H., Wei, S., and Raftery, D. (2012). Quantitative Analysis of Urea in Human Urine and Serum by  $^1\text{H}$  Nuclear Magnetic Resonance. *Analyst*, 137(3), 595-600.
- Luo, J., Tong, H., Mo, S., Zhou, F., Zuo, S., Yin, C., Xu, J., and Li, X. (2023). Integrated Exploration of Experimentation and Molecular Simulation in Ester-Containing Polyimide Dielectrics. *RSC Advances*, 13(2), 963-972.
- Magar, H. S., Hassan, R. Y., and Mulchandani, A. (2021). Electrochemical Impedance Spectroscopy (Eis): Principles, Construction, and Biosensing Applications. *Sensors*, 21(19), 6578.
- Meera, R., Neena, P., Pradeep, A., Nair, B. G., Vasu, S. P., and Babu, T. S. (2024). Non-Enzymatic Electrochemical Detection of Urine Creatinine Using Cobalt-Gold Bimetallic Nanoparticles. *Journal of The Electrochemical Society*, 171(6), 067504.
- Mei, S., Xu, G., Xing, J., and WU, C. (2001). Method for the Analysis of 8-Hydroxy-2'-Deoxyguanosine in Urine by Gas Chromatography. *Analytical sciences*, 17(6), 779-781.
- Moon, J. S., Lee, J. E., and Yoon, J. S. (2013). Variation in Serum Creatinine Level Is Correlated to Risk of Type 2 Diabetes. *Endocrinology and Metabolism*, 28(3), 207.
- Moreira Da Silva, C., Vallet, M., Semion, C., Blin, T., Saint-Martin, R., Leroy, J., Dragoe, D., Brisset, F., Gillet, C., and Guillot, R. (2023). A Simple and Efficient Process for the Synthesis of 2d Carbon Nitrides and Related Materials. *Scientific reports*, 13(1), 15423.

- Nazeeruddin, M. K., Zakeeruddin, S., and Kalyanasundaram, K. (1993). Enhanced Intensities of the Ligand-to-Metal Charge-Transfer Transitions in Ruthenium (Iii) and Osmium (Iii) Complexes of Substituted Bipyridines. *The Journal of Physical Chemistry*, 97(38), 9607-9612.
- Ngamchuea, K., Batchelor-McAuley, C., and Compton, R. G. (2018). Anodic Stripping Voltammetry of Silver in the Absence of Electrolytes: Theory and Experiment. *Journal of Electroanalytical Chemistry*, 830, 122-130.
- Ngamchuea, K., Tharat, B., Hirunsit, P., and Suthirakun, S. (2020). Electrochemical Oxidation of Resorcinol: Mechanistic Insights from Experimental and Computational Studies. *RSC advances*, 10(47), 28454-28463.
- Ngamchuea, K., Wannapaiboon, S., Nongkhunsan, P., Hirunsit, P., and Fongkaew, I. (2022). Structural and Electrochemical Analysis of Copper-Creatinine Complexes: Application in Creatinine Detection. *Journal of The Electrochemical Society*, 169(2), 020567.
- Nikolaidis, S., Kosmidis, I., Sougioultzis, M., Kabasakalis, A., and Mougios, V. (2018). Diurnal Variation and Reliability of the Urine Lactate Concentration after Maximal Exercise. *Chronobiology International*, 35(1), 24-34.
- Nontawong, N., Amatongchai, M., Thimoonnee, S., Laosing, S., Jarujamrus, P., Karuwan, C., and Chairam, S. (2019). Novel Amperometric Flow-Injection Analysis of Creatinine Using a Molecularly-Imprinted Polymer Coated Copper Oxide Nanoparticle-Modified Carbon-Paste-Electrode. *Journal of Pharmaceutical and Biomedical Analysis*, 175, 112770.
- Olayinka, L., Garnett, E., Burnett, B., and Devaraj, S. (2023). Comparison of Random Urine Protein/Creatinine Ratio with 24-Hour Urine Protein in Suspected Pre-Eclampsia. *Practical Laboratory Medicine*, 36, e00316.
- Oliveira-Brett, A. M., Silva, L. A. d., and Brett, C. M. (2002). Adsorption of Guanine, Guanosine, and Adenine at Electrodes Studied by Differential Pulse Voltammetry and Electrochemical Impedance. *Langmuir*, 18(6), 2326-2330.
- Opravil, M., Keusch, G., and Lüthy, R. (1993). Pyrimethamine Inhibits Renal Secretion of Creatinine. *Antimicrobial agents and chemotherapy*, 37(5), 1056-1060.
- Persson, F., and Rossing, P. (2018). Diagnosis of Diabetic Kidney Disease: State of the Art and Future Perspective. *Kidney international supplements*, 8(1), 2-7.

- Pesch, B., Lotz, A., Koch, H. M., Marczynski, B., Casjens, S., Käfferlein, H. U., Welge, P., Lehnert, M., Heinze, E., and Van Gelder, R. (2015). Oxidatively Damaged Guanosine in White Blood Cells and in Urine of Welders: Associations with Exposure to Welding Fumes and Body Iron Stores. *Archives of toxicology*, *89*(8), 1257-1269.
- Piéroni, L., Delanaye, P., Boutten, A., Bargnoux, A.-S., Rozet, E., Delatour, V., Carlier, M.-C., Hanser, A.-M., Cavalier, E., and Froissart, M. (2011). A Multicentric Evaluation of Idms-Traceable Creatinine Enzymatic Assays. *Clinica chimica acta*, *412*(23-24), 2070-2075.
- Pilger, A., Ivancsits, S., Germadnik, D., and Rüdiger, H. (2002). Urinary Excretion of 8-Hydroxy-2'-Deoxyguanosine Measured by High-Performance Liquid Chromatography with Electrochemical Detection. *Journal of Chromatography B*, *778*(1-2), 393-401.
- Pinitsoontorn, S., Prasoetsopha, N., Srepusharawoot, P., Bootchanont, A., Kidkhunthod, P., Kamwanna, T., Amornkitbamrung, V., Kurosaki, K., and Yamanaka, S. (2014). Local Structure Determination of Substitutional Elements in  $\text{Ca}_3\text{Co}_4\text{-Xm}_x\text{O}_9$  (M= Fe, Cr, Ga) Using X-Ray Absorption Spectroscopy. *physica status solidi (a)*, *211*(8), 1732-1739.
- Pizzino, G., Irrera, N., Cucinotta, M., Pallio, G., Mannino, F., Arcoraci, V., Squadrito, F., Altavilla, D., and Bitto, A. (2017). Oxidative Stress: Harms and Benefits for Human Health. *Oxidative medicine and cellular longevity*, *2017*(1), 8416763.
- Pottel, H., Vrydags, N., Mahieu, B., Vandewynckele, E., Croes, K., and Martens, F. (2008). Establishing Age/Sex Related Serum Creatinine Reference Intervals from Hospital Laboratory Data Based on Different Statistical Methods. *Clinica chimica acta*, *396*(1-2), 49-55.
- Price, C. P., Newall, R. G., and Boyd, J. C. (2005). Use of Protein: Creatinine Ratio Measurements on Random Urine Samples for Prediction of Significant Proteinuria: A Systematic Review. *Clinical chemistry*, *51*(9), 1577-1586.
- Pundir, C., Kumar, P., and Jaiwal, R. (2019). Biosensing Methods for Determination of Creatinine: A Review. *Biosensors and Bioelectronics*, *126*, 707-724.
- Rakesh Kumar, R., Shaikh, M. O., Kumar, A., Liu, C.-H., and Chuang, C.-H. (2023). Zwitterion-Functionalized Cuprous Oxide Nanoparticles for Highly Specific and Enzymeless Electrochemical Creatinine Biosensing in Human Serum. *ACS Applied Nano Materials*, *6*(3), 2083-2094.

- Rao, H., Lu, Z., Ge, H., Liu, X., Chen, B., Zou, P., Wang, X., He, H., Zeng, X., and Wang, Y. (2017). Electrochemical Creatinine Sensor Based on a Glassy Carbon Electrode Modified with a Molecularly Imprinted Polymer and a Ni@ Polyaniline Nanocomposite. *Microchimica Acta*, *184*, 261-269.
- Raveendran, J., Resmi, P., Ramachandran, T., Nair, B. G., and Babu, T. S. (2017). Fabrication of a Disposable Non-Enzymatic Electrochemical Creatinine Sensor. *Sensors and Actuators B: Chemical*, *243*, 589-595.
- Ravel, B., and Newville, M. (2005). Athena, Artemis, Hephaestus: Data Analysis for X-Ray Absorption Spectroscopy Using Ifeffit. *Journal of synchrotron radiation*, *12*(4), 537-541.
- Salim, S. (2017). Oxidative Stress and the Central Nervous System. *Journal of Pharmacology and Experimental Therapeutics*, *360*(1), 201-205.
- Sarioğulları, H., Şenocak, A., Basova, T., Demirbaş, E., and Durmuş, M. (2019). Effect of Different Swcnt-Bodipy Hybrid Materials for Selective and Sensitive Electrochemical Detection of Guanine and Adenine. *Journal of Electroanalytical Chemistry*, *840*, 10-20.
- Scholz, R., Palatzky, P., and Matysik, F.-M. (2014). Simulation of Oxidative Stress of Guanosine and 8-Oxo-7, 8-Dihydroguanosine by Electrochemically Assisted Injection–Capillary Electrophoresis–Mass Spectrometry. *Analytical and Bioanalytical Chemistry*, *406*, 687-694.
- Segawa, M., Nomura, Y., and Nishiyama, N. (2003). Autosomal Dominant Guanosine Triphosphate Cyclohydrolase I Deficiency (Segawa Disease). *Annals of Neurology: Official Journal of the American Neurological Association and the Child Neurology Society*, *54*(S6), S32-S45.
- Selden, C. R., Schilling, K., Godfrey, L., and Yee, N. (2024). Metal-Binding Amino Acid Ligands Commonly Found in Metalloproteins Differentially Fractionate Copper Isotopes. *Scientific reports*, *14*(1), 1902.
- Şenocak, A., Korkmaz, E., Khataee, A., and Demirbas, E. (2022). A Facile and Synergetic Strategy for Electrochemical Sensing of Rutin Antioxidant by Ce–Cr Doped Magnetite@ Rgo. *Materials Chemistry and Physics*, *275*, 125298.
- Şenocak, A., Sanko, V., Tümay, S. O., Orooji, Y., Demirbas, E., Yoon, Y., and Khataee, A. (2022). Ultrasensitive Electrochemical Sensor for Detection of Rutin Antioxidant by Layered Ti<sub>3</sub>Al<sub>0.5</sub>Cu<sub>0.5</sub>C<sub>2</sub> Max Phase. *Food and Chemical Toxicology*, *164*, 113016.

- Şenocak, A., Tümay, S. O., Ömeroğlu, İ., and Şanko, V. (2022). Crosslinker Polycarbazole Supported Magnetite Mof@ Cnt Hybrid Material for Synergetic and Selective Voltammetric Determination of Adenine and Guanine. *Journal of Electroanalytical Chemistry*, 905, 115963.
- Shafiee, A., Salleh, M. M., and Yahaya, M. (2011). Determination of Homo and Lumo of [6, 6]-Phenyl C61-Butyric Acid 3-Ethylthiophene Ester and Poly (3-Octyl-Thiophene-2, 5-Diyl) through Voltametry Characterization. *Sains Malaysiana*, 40(2), 173-176.
- Shi, H., Ma, Y., and Ma, Y. (1995). A Simple and Fast Method to Determine and Quantify Urinary Creatinine. *Analytica chimica acta*, 312(1), 79-83.
- Spierto, F., Hannon, W., Gunter, E., and Smith, S. (1997). Stability of Urine Creatinine. *Clinica chimica acta*, 264(2), 227-232.
- Sriramprabha, R., Sekar, M., Revathi, R., Viswanathan, C., and Wilson, J. (2020). Fe<sub>2</sub>O<sub>3</sub>/Polyaniline Supramolecular Nanocomposite: A Receptor Free Sensor Platform for the Quantitative Determination of Serum Creatinine. *Analytica chimica acta*, 1137, 103-114.
- Sun, S.-W., Liu, H.-L., Zhou, Y., Wang, F.-B., and Xia, X.-H. (2017). Copper–Nitrogen-Doped Graphene Hybrid as an Electrochemical Sensing Platform for Distinguishing DNA Bases. *Analytical Chemistry*, 89(20), 10858-10865.
- Sun, W., Duan, Y., Li, Y., Gao, H., and Jiao, K. (2009). Electrochemical Behaviors of Guanosine on Carbon Ionic Liquid Electrode and Its Determination. *Talanta*, 78(3), 695-699.
- Sun, W., Li, Y., Duan, Y., and Jiao, K. (2009). Direct Electrochemistry of Guanosine on Multi-Walled Carbon Nanotubes Modified Carbon Ionic Liquid Electrode. *Electrochimica acta*, 54(16), 4105-4110.
- Sun, W., Wang, X., Sun, X., Deng, Y., Liu, J., Lei, B., and Sun, Z. (2013). Simultaneous Electrochemical Determination of Guanosine and Adenosine with Graphene–ZrO<sub>2</sub> Nanocomposite Modified Carbon Ionic Liquid Electrode. *Biosensors and Bioelectronics*, 44, 146-151.
- Tajkhorshid, E., and Suhai, S. (1999). Dielectric Effects Due to the Environment on the Structure and Proton Affinity of Retinal Schiff Base Models. *Chemical Physics Letters*, 299(5), 457-464.
- Tang, W., Zhang, M., Li, W., and Zeng, X. (2014). An Electrochemical Sensor Based on Polyaniline for Monitoring Hydroquinone and Its Damage on DNA. *Talanta*, 127, 262-268.

- Thompson, H., and Rechnitz, G. (1974). Ion Electrode Based Enzymic Analysis of Creatinine. *Analytical Chemistry*, 46(2), 246-249.
- Toh, H. S., Batchelor-McAuley, C., Tschulik, K., Uhlemann, M., Crossley, A., and Compton, R. G. (2013). The Anodic Stripping Voltammetry of Nanoparticles: Electrochemical Evidence for the Surface Agglomeration of Silver Nanoparticles. *Nanoscale*, 5(11), 4884-4893.
- Tümay, S. O., Sanko, V., Şenocak, A., Orooji, Y., Demirbas, E., Yoon, Y., and Khataee, A. (2023). Direct and Selective Determination of P-Coumaric Acid in Food Samples Via Layered Nb<sub>4</sub>alc<sub>3</sub>-Max Phase. *Food chemistry*, 403, 134130.
- Uauy, R., Olivares, M., and Gonzalez, M. (1998). Essentiality of Copper in Humans. *The American journal of clinical nutrition*, 67(5), 952S-959S.
- Uemura, O., Honda, M., Matsuyama, T., Ishikura, K., Hataya, H., Yata, N., Nagai, T., Ikezumi, Y., Fujita, N., and Ito, S. (2011). Age, Gender, and Body Length Effects on Reference Serum Creatinine Levels Determined by an Enzymatic Method in Japanese Children: A Multicenter Study. *Clinical and experimental nephrology*, 15, 694-699.
- Ugarte, A., Gil-Bea, F., García-Barroso, C., Cedazo-Minguez, Á., Ramírez, M. J., Franco, R., García-Osta, A., Oyarzabal, J., and Cuadrado-Tejedor, M. (2015). Decreased Levels of Guanosine 3', 5'-Monophosphate (C Gmp) in Cerebrospinal Fluid (Csf) Are Associated with Cognitive Decline and Amyloid Pathology in a Lzheimer's Disease. *Neuropathology and applied neurobiology*, 41(4), 471-482.
- Varodi, C., Pogăcean, F., Ciorită, A., Pană, O., Leoştean, C., Cozar, B., Radu, T., Coroş, M., Ştefan-van Staden, R. I., and Pruneanu, S.-M. (2021). Nitrogen and Sulfur Co-Doped Graphene as Efficient Electrode Material for L-Cysteine Detection. *Chemosensors*, 9(6), 146.
- Voityuk, A. A., and Vyboishchikov, S. F. (2019). A Simple Cosmo-Based Method for Calculation of Hydration Energies of Neutral Molecules. *Physical Chemistry Chemical Physics*, 21(34), 18706-18713.
- Wallace, G. (1985). Dissolved Oxygen: The Electroanalytical Chemists Dilemma. *TrAC Trends in Analytical Chemistry*, 4(6), 145-148.
- Wang, L., Wang, J., and Zhou, F. (2004). Direct Electrochemistry of Catalase at a Gold Electrode Modified with Single-Wall Carbon Nanotubes. *Electroanalysis: An International Journal Devoted to Fundamental and Practical Aspects of Electroanalysis*, 16(8), 627-632.

- Wang, Y., Chen, J., Wu, Y., Chen, Y., Pan, J., Lei, J., Chen, Y., Sun, L., Feng, S., and Chen, R. (2012). *Surface-Enhanced Raman Spectroscopy of Creatinine in Silver Colloid*. Paper presented at the Tenth International Conference on Photonics and Imaging in Biology and Medicine (PIBM 2011).
- Ward Jones, S. E., Campbell, F. W., Baron, R., Xiao, L., and Compton, R. G. (2008). Particle Size and Surface Coverage Effects in the Stripping Voltammetry of Silver Nanoparticles: Theory and Experiment. *The Journal of Physical Chemistry C*, 112(46), 17820-17827.
- Wei, F., Cheng, S., Korin, Y., Reed, E. F., Gjertson, D., Ho, C.-m., Gritsch, H. A., and Veale, J. (2012). Serum Creatinine Detection by a Conducting-Polymer-Based Electrochemical Sensor to Identify Allograft Dysfunction. *Analytical Chemistry*, 84(18), 7933-7937.
- Weigend, F., and Ahlrichs, R. (2005). Balanced Basis Sets of Split Valence, Triple Zeta Valence and Quadruple Zeta Valence Quality for H to Rn: Design and Assessment of Accuracy. *Physical Chemistry Chemical Physics*, 7(18), 3297-3305.
- Wen, T., Zhu, W., Xue, C., Wu, J., Han, Q., Wang, X., Zhou, X., and Jiang, H. (2014). Novel Electrochemical Sensing Platform Based on Magnetic Field-Induced Self-Assembly of Fe<sub>3</sub>O<sub>4</sub>@ Polyaniline Nanoparticles for Clinical Detection of Creatinine. *Biosensors and Bioelectronics*, 56, 180-185.
- Yazhini, K., Suja, S., Bagyalakshmi, J., and Pavalamalar, S. (2018). Non-Enzymatic Sensing of Kidney Dysfunction Biomarker Using Pectin-Mwcnt Nanocomposite. *Applied Surface Science*, 449, 736-744.
- Yin, H., Zhou, Y., Ma, Q., Ai, S., Chen, Q., and Zhu, L. (2010). Electrocatalytic Oxidation Behavior of Guanosine at Graphene, Chitosan and Fe<sub>3</sub>O<sub>4</sub> Nanoparticles Modified Glassy Carbon Electrode and Its Determination. *Talanta*, 82(4), 1193-1199.
- Yokoyama, Y., Tsuji, S., and Sato, H. (2005). Simultaneous Determination of Creatinine, Creatine, and Uv-Absorbing Amino Acids Using Dual-Mode Gradient Low-Capacity Cation-Exchange Chromatography. *Journal of Chromatography A*, 1085(1), 110-116.
- Zhao, C., Wang, B., Zhong, S., Akhtaruzzaman, M., Liang, W., and Chen, H. (2023). Ndt Studies of Nanoscale Polymeric Coatings. In *Polymer-Based Nanoscale Materials for Surface Coatings* (pp. 235-257): Elsevier.

- Zhu, D., Chu, M., Xin, J., Wang, X., O'Halloran, K. P., Ma, H., Pang, H., Tan, L., and Yang, G. (2021). Hierarchical and Hollow Boron/Nitrogen Co-Doped Yolk-Shell Mesoporous Carbon Nanospheres Attached to Reduced Graphene Oxide with High Sensing Performance for the Simultaneous Detection of Xanthine and Guanosine. *Sensors and Actuators B: Chemical*, 343, 130068.
- Zhu, D., Zhen, Q., Xin, J., Ma, H., Pang, H., Tan, L., and Wang, X. (2021). In Situ Hierarchical Encapsulation of Bimetallic Selenides into Honeycomb-Like Nitrogen Doped Porous Carbon Nanosheets for Highly Sensitive and Selective Guanosine Detection. *Journal of Colloid and Interface Science*, 598, 181-192.
- Zimmermann, P., Peredkov, S., Abdala, P. M., DeBeer, S., Tromp, M., Müller, C., and van Bokhoven, J. A. (2020). Modern X-Ray Spectroscopy: Xas and Xes in the Laboratory. *Coordination Chemistry Reviews*, 423, 213466.



## CURRICULUM VITAE

**Name:** Jinnapat Wijitsak  
**Contact Address:** 126 Village No.6 Phathairin Sub-district,  
Lamplaimat District, Buriram, 31130  
**Email:** jinnapat1512@gmail.com  
**Date of Birth:** 15<sup>th</sup> December 2000

### Education

2019 – 2023 B.Sc. (Chemistry) (GPAX 3.51, 1<sup>st</sup> class honor), *Suranaree University of Technology*  
2016 – 2019 High School Diploma (GPAX 3.96), *Lamplaimat School*

### Scholarships

2023 – present Suranaree University Scholarships, *Suranaree University of Technology*

### Publications

Electrochemical oxidation of guanosine: Mechanistic insights and direct detection in weakly supported media. **J. Wijitsak**, B. Tharat, S. Suthirakul, K. Ngamchuea, *Journal of Electroanalytical Chemistry*, 950, (2023), 117878.

Catalysis of oxygen reduction reaction by iron porphyrin and its sensing application. T. Rattanaumpa, P. Panbo, S. Suthirakun, K. Kaewket, **J. Wijitsak**, P. Pinyou, K. Ngamchuea, *Journal of Electroanalytical Chemistry*, 973, (2024), 118647.

Machine learning-guided cobalt@copper dual-metal electrochemical sensor for urinary creatinine detection. K. Kaewket, T. Outrequin, S. Deepaisarn, **J. Wijitsak**, P. Sunon, K. Ngamchuea, *ACS sensors*, 2025. 10(5): p. 3471-3483.

Elucidating Redox-Active Molecular Architectures: Copper(II) Methylthio-Imidazole Schiff Base Complex for Small-Molecule Recognition. **J. Wijitsak**, T. Boonprab, P. Harding,<sup>1</sup> D. J. Harding, Jack K. Clegg, K. Kaewket, C. Jakkrawhad, S. Nijpanich, S. Wannapaiboon, W. Kaewraung, S. Suthirakun, K. Ngamchuea, *manuscript submitted*.